

INFORMATION TO USERS

This manuscript has been reproduced from the microfilm master. UMI films the text directly from the original or copy submitted. Thus, some thesis and dissertation copies are in typewriter face, while others may be from any type of computer printer.

The quality of this reproduction is dependent upon the quality of the copy submitted. Broken or indistinct print, colored or poor quality illustrations and photographs, print bleedthrough, substandard margins, and improper alignment can adversely affect reproduction.

In the unlikely event that the author did not send UMI a complete manuscript and there are missing pages, these will be noted. Also, if unauthorized copyright material had to be removed, a note will indicate the deletion.

Oversize materials (e.g., maps, drawings, charts) are reproduced by sectioning the original, beginning at the upper left-hand corner and continuing from left to right in equal sections with small overlaps.

Photographs included in the original manuscript have been reproduced xerographically in this copy. Higher quality 6" x 9" black and white photographic prints are available for any photographs or illustrations appearing in this copy for an additional charge. Contact UMI directly to order.

**ProQuest Information and Learning
300 North Zeeb Road, Ann Arbor, MI 48106-1346 USA
800-521-0600**

UMI[®]

University of Alberta

Low Frequency Macroinstabilities in a Stirred Tank.

by

Vesselina Tzvetanova Roussinova ©

**A thesis submitted to the Faculty of Graduate Studies and Research in partial fulfillment
of requirements of the degree of Master of Science**

in

Chemical Engineering

Department of Chemical and Material Engineering

Edmonton, Alberta

Fall 2001



**National Library
of Canada**

**Acquisitions and
Bibliographic Services**

**395 Wellington Street
Ottawa ON K1A 0N4
Canada**

**Bibliothèque nationale
du Canada**

**Acquisitions et
services bibliographiques**

**395, rue Wellington
Ottawa ON K1A 0N4
Canada**

Your file Votre référence

Our file Notre référence

The author has granted a non-exclusive licence allowing the National Library of Canada to reproduce, loan, distribute or sell copies of this thesis in microform, paper or electronic formats.

The author retains ownership of the copyright in this thesis. Neither the thesis nor substantial extracts from it may be printed or otherwise reproduced without the author's permission.

L'auteur a accordé une licence non exclusive permettant à la Bibliothèque nationale du Canada de reproduire, prêter, distribuer ou vendre des copies de cette thèse sous la forme de microfiche/film, de reproduction sur papier ou sur format électronique.

L'auteur conserve la propriété du droit d'auteur qui protège cette thèse. Ni la thèse ni des extraits substantiels de celle-ci ne doivent être imprimés ou autrement reproduits sans son autorisation.

0-612-69813-0

Canada

University of Alberta

Library Release Form

Name of Author: Vesselina Tzvetanova Roussinova


Title of Thesis: Low Frequency Macroinstabilities in a Stirred Tank

Degree: Master of Science

Year this Degree Granted: 2001

Permission is hereby granted to the University of Alberta Library to reproduce single copies of this thesis and to lend or sell such copies for private, scholarly or scientific research purposes only.

The author reserves all other publication and other rights in association with the copyright in the thesis, and except as herein before provided, neither the thesis nor any substantial portion thereof may be printed or otherwise reproduced in any material form whatever without the author's prior written permission.



Vesselina Tzvetanova Roussinova

Michener Park 519C

Edmonton, AB

T6H4M5

Date: 28/Sept/2001

University of Alberta

Faculty of Graduate Studies and Research

The undersigned certify that they have read, and recommend to the Faculty of Graduate Studies and Research for acceptance, a thesis entitled ***Low Frequency Macroinstabilities in a Stirred tank*** submitted by ***Vesselina Tzvetanova Roussinova*** in partial fulfillment of the requirements for the degree of Master of Science in Chemical Engineering.


Dr. S.M. Kresta (Supervisor)


Dr. Peter Minev


Dr. Kumar Nandakumar

Date: Sept 25, 2001

Abstract

In this thesis, the macroinstabilities (MI) produced by three axial impellers; the 45 degree pitched blade turbine (PBT), the Lightnin fluidfoil (A310) and the Chemineer high efficiency HE3, are studied. These phenomena are observed as an unsteady, low-period variation of the velocity as measured with Laser Doppler Velocimetry (LDV). The process of particle arrival is random and therefore the time between measured samples is non-uniform. This precludes the use of standard spectral estimators. The frequencies from unequally spaced data must be calculated by using the Lomb algorithm.

For the 45° PBT with impeller diameter $D=T/2$ at an off-bottom clearance ratio $C/D=0.50$ the frequency of the macroinstability scales linearly with the rotational speed, remaining constant at $f_{MI}/N=0.186$. The A310 and HE3 impeller showed no coherent frequency in any of the geometries examined. Key measurements were repeated in a large-scale tank of diameter $T=1.22\text{m}$ (4.0ft) with the same result. LES simulations revealed exactly the same frequency as the experiments and provide a closer examination of the mechanism which drives the macroinstability.

Acknowledgements

Many people have contributed their ideas, support and time to help make this research possible. First, I would like to thank my supervisor Dr. Suzanne Kresta for her encouragement and support. Without her guidance and constructive criticism this work could not be as complete as it is now.

I also wish to thank Dr. Ron Weetman, Gary Houdenious, Craig Bahr and all people from Lightnin who helped me during my six weeks stay in Rochester, USA. I have enjoyed the time spent in Lightnin.

This study was possible, thanks to the financial assistance from Lightnin, DOW Chemical, FLUENT and National Sciences and Engineering Research Council (NSERC).

Table of Contents

Chapter 1: Introduction	1
1.1 Macroinstabilities in the stirred tank-current state of knowledge	2
1.2 Frequency analysis of unevenly spaced data	7
1.2.1 Fast Fourier transform (FFT)	8
1.2.2 Autocorrelation methods	9
1.2.3 Wavelet analysis	11
1.2.4 Lomb periodogram	16
1.3 Conclusions	20
1.4 Nomenclature	22
1.5 References	25
1.6 Appendix	32
Chapter 2: Experiments and Results	37
2.1 LDV apparatus	40
2.1.1 Small scale experiments	41
2.1.2 Large scale experiments	43
2.2 Mixing tank geometries and fluids	44
2.2.1 Mixing tanks	44
2.2.2 Impellers and fluids	45
2.2.3 Flow visualization	47
2.3 Experimental errors	48
2.3.1 Viscosity measurement	48
2.3.2 LDV measurements	49
2.4 Results	52
2.4.1 HE3 and A310	53
2.4.2 PBT	54
2.5 Conclusions	56
2.6 Nomenclature	58
2.7 References	59
Chapter 3: Large eddy simulation	82
3.1 Introduction	83
3.2 The choice of turbulent model	88
3.2.1 Two equation k- ϵ model	88
3.2.2 Large eddy simulations approach	93
3.3 Simulation conditions	96
3.3.1 Differences between the structured and the unstructured grid	96
3.3.2 Numerical procedure	97
3.4 Results	99

3.4.1 Mean flow	99
3.4.2 Frequency analysis	102
3.4.3 Transient flow field of the 45° PBT	103
3.5 Conclusions	104
3.6 Nomenclature	105
3.7 References	107
3.8 Appendix	133

Table of Tables

Table 2-1. Parameters of the two LDV systems used in this work.	61
Table 2-2. Dimensions of the PBT impellers used at the small and large-scale experiments.	61
Table 2-3. Experimental configurations studied.	62
Table 2-4. Range of viscosities covered by the experiments.	62
Table 2-5. Summary of the radial and vertical positions of measurements for both small and large scale tanks.	63
Table 3-1. Parameters of the LES wall jet profiles	109
Table 3-2. Time periods showing how long the jets sits either impinging on the bottom or the wall of the tank. The average period of flapping coincides with the f_{MI} obtained from FFT.	110

Table of Figures

Figure 1-1. Geometry of stirred tank as defined for this work.	27
Figure 1-2. Comparison between the mean and instantaneous velocity fields for the 45° PBT. Data from Bakker and Fasano (1995).	28
Figure 1-3. BPF and macroinstabilities (MI) evident in the impeller stream (45° PBT, C/D=0.5 and D=T/2, fluid water, Re=48,000).	29
Figure 1-4. Decay of the BPF in the upper part of the tank: only the macroinstabilities and the turbulence persist (45° PBT, C/D=0.5 and D=T/2, fluid water, Re=48,000).	29
Figure 1-5. A test signal (a) and its continuous wavelet transform using the Morlet wavelet (b). The periodic oscillations are represented by vertical dark and white stripes. The cones are also visible at the location of signal singularities.	30
Figure 1-6. A sample LDV signal (a) and its continuous wavelet transform using the Morlet wavelet (b). We visualize the absolute values of the wavelet coefficients vs. the number of examined data points. N_{MI} represents the periodicity due to MI, and N_{BP} represents the periodicity due to blade passages.	31
Figure 2-1. Schematics of the a) forward scattering LDV system and b) backscattering LDV system.	64
Figure 2-2. Signal components of Doppler burst showing: a) Total signal b) High-pass filtering the modulated light intensity results in an oscillating signal. The frequency corresponds to the velocity of the tracer particles. c) Real sequence of Doppler bursts with some noise. Data are taken from Dantec Dynamics.	65
Figure 2-3. Examples of the frequency spectra obtained from a) LDV signal processor by van Maanen, 1999 and b) constant temperature anemometry (CTA) technique by Wernerson, 1997.	65

- Figure 2-4.** The mean and the RMS axial velocity profiles across the lower edge of the 45° PBT for two different shift frequencies: 40MHz and 1 MHz. The effect of the number of samples is also shown. 66
- Figure 2-5.** Natural frequency of the impeller-shaft system a) 45° PBT ($D=T/2$, $C/D=0.50$). Natural frequency of 3.775Hz. b) A310 $D=0.36T$ natural frequency of 4.425Hz. 67
- Figure 2-6.** Impellers used in this work: 45° PBT impellers, $D=T/2$, small and large scale, fluidfoil A310 (by Lightnin) and high efficiency impeller by Chemineer (HE3- axial flow). 68
- Figure 2-7.** Top view of the regions of vortex disintegration on the free surface of the mixing tank (after Fort and Bruha, 1993). 69
- Figure 2-8.** Schematic of the small-scale mixing tank showing the LDV measurement grid. 69
- Figure 2-9.** Variation of viscosity for different water solutions of TEG (wt%). Dotted symbols represent the actual measurements while the solid line is their best fit. 70
- Figure 2-10.** Dependence of viscosity on temperature for TEG–water mixtures (large scale experiments). 70
- Figure 2-11.** Specific gravities of triethylene glycol aqueous solutions at various concentrations. Data are taken from Shell Chemical –online library. 71
- Figure 2-12.** Viscosities of triethylene glycol aqueous solutions. Data are taken from Shell Chemical –online library. 72
- Figure 2-13.** Frequency spectrum for the axial velocity at $2r/D=1.05$ showing the presence of the BPF and MI. 73

- Figure 2-14.** Frequency spectrum for the axial velocity at $2r/D=1.35$ showing the presence only of the MI. Note that the $f_{MI}=0.92\text{Hz}$, (45° PBT, $C/D=0.5$ and $D=T/2$, fluid bayol, $Re=24,000$). 73
- Figure 2-15.** Distribution of MI frequency for *HE3* with constant impeller diameter, $D=T/3$ and various C/D ratios: a) $C/D=0.40$, b) $C/D=0.80$ and c) $C/D=1.0$ 74
- Figure 2-16.** Distribution of MI frequency for *A310* with constant impeller diameter, $D=0.58T$ and various C/D ratios: a) $C/D=0.33$, b) $C/D=0.50$ and c) $C/D=0.67$. 75
- Figure 2-17.** Distribution of MI frequency for the large-scale *A310* ($D=0.35T$, $C/D=1.0$) at $Re=5.65 \times 10^4$. No coherent frequency was detected. 76
- Figure 2-18.** Distribution of MI frequency for 45° PBT with constant impeller diameter, $D=T/2$ and various C/D ratios: a) $C/D=0.33$, b) $C/D=0.50$ and c) $C/D=0.67$, $Re=48,000$. 77
- Figure 2-19.** Distribution of MI frequency for large-scale 45° PBT with constant impeller diameter, $D=T/2$ and various C/D ratios: a) $C/D=0.33$, b) $C/D=0.50$ and c) $C/D=0.67$. The Reynolds number was greater than 20,000 for all runs. 78
- Figure 2-20.** Combined results showing the scaling of the dimensionless frequency for the resonant geometry (45° PBT, $D=T/2$, $C/D=0.50$) small and large scale experiments. 79
- Figure 2-21.** Zones of the large-scale tank showing the spatial position where the coherent frequency is found at three different axial locations a) $z/T=0.60$, b) $z/T=0.70$ and c) $z/T=0.90$. Configuration 45° PBT $D=T/2$, $C/D=0.50$, $Re=20,000$. 80
- Figure 2-22.** Distribution of MI frequency for 45° PBT with constant impeller diameter, $D=T/3$ and $C/D=0.50$ at various Reynolds numbers: a) $Re=18,000$, b) $Re=20,000$ and c) $Re=25,000$. 81

- Figure 3-1.** Schematic of the idealized turbulent spectrum. The inertial subrange is characterized by a $-5/3$ slope. 111
- Figure 3-2.** Separation of the computational domain with a sliding mesh interface. The sliding surface was chosen to lie midway between the baffles and the tip of the impeller blades: a) top view and b) side view. LES was used to examine both planes 1 and 2. 112
- Figure 3-3.** Two-dimensional sliding mesh interface (Mathur, 1994) 112
- Figure 3-4.** Radial profile of the axial velocity in the impeller discharge stream for the resonant geometry (45° PBT, $D=T/2$, $C/D=0.50$). Comparison with the experimental data from Kresta and Wood (1993b) taken 2mm below the impeller blade. Effect of hub size is also shown. 113
- Figure 3-5.** Schematic of the 3-D wall jet radial profiles at different axial locations in a stirred tank (Bhattacharya and Kresta, 2001). 114
- Figure 3-6.** Similarity profiles (experimental data by Bittorf, 2000) fitted with the similarity solution for the 3-D wall jet (Equation 3.27). 115
- Figure 3-7.** Similarity profiles from LES simulation of the resonant geometry (45° PBT, $D=T/2$, $C/D=0.50$). 115
- Figure 3-8.** Regular oscillations in axial velocity due to macroinstabilities: a) LES time series and b) LDV experimental time series. Note that the turbulence is filtered out of the LES time series. Data are taken at $2r/D=1.58$ and $z/T=0.50$. 116
- Figure 3-9.** LES frequency distribution histogram with maximum at dimensionless frequency $f_{MI}/N=0.186$. 117
- Figure 3-10.** Graph showing the scaling of LES f_{MI}/N with impeller Reynolds number. 117

Figure 3-11a. Instantaneous velocity field (r-z plane) produced by 45° PBT after 18.00s.	118
Figure 3-11b. Instantaneous velocity field (r-z plane) produced by 45° PBT after 18.75s.	119
Figure 3-11c. Instantaneous velocity field (r-z plane) produced by 45° PBT after 19.50s.	120
Figure 3-11d. Instantaneous velocity field (r-z plane) produced by 45° PBT after 20.25s.	121
Figure 3-11e. Instantaneous velocity field (r-z plane) produced by 45° PBT after 21.00s.	122
Figure 3-11f. Instantaneous velocity field (r-z plane) produced by 45° PBT after 21.75s.	123
Figure 3-11g. Instantaneous velocity field (r-z plane) produced by 45° PBT after 22.50s.	124
Figure 3-12. Schematic of the four jet interaction below the impeller and close to the tank bottom: a) Side view and b) Top view.	125
Figure 3-13a. Instantaneous velocity field (r- θ plane) produced by 45° PBT after 18.00s.	126
Figure 3-13b. Instantaneous velocity field (r- θ plane) produced by 45° PBT after 18.75s.	127
Figure 3-13c. Instantaneous velocity field (r- θ plane) produced by 45° PBT after 19.50s.	128

Figure 3-13d. Instantaneous velocity field (r- θ plane) produced by 45° PBT after 20.25s. 129

Figure 3-13e. Instantaneous velocity field (r- θ plane) produced by 45° PBT after 21.00s. 130

Figure 3-13f. Instantaneous velocity field (r- θ plane) produced by 45° PBT after 21.75s. 131

Figure 3-13g. Instantaneous velocity field (r- θ plane) produced by 45° PBT after 22.50s. 132

Chapter 1: Introduction

Recognizable structures or events in turbulent flow occur randomly in time and space and have a certain randomness in appearance and orientation. Detection of such events is subject to uncertainty, and the recognition criteria and experimental methods play a critical role in the measurement result. It is important to be able to define what one wants to look for and to use detection methods that are somewhat immune to the randomness in time and location of events. One classical way of characterizing the existing structures in a turbulent flow is to extract information about the frequency spectrum from velocity time series measurements using the fast Fourier transform (FFT). The FFT analysis however is possible only if the velocity data are evenly sampled. The main data analysis problem in this work is extraction of unbiased information for the frequency content from unevenly sampled Laser Doppler Velocimetry (LDV) data.

1.1 Macroinstabilities in a stirred tank-current state of knowledge

The stirred tank defined for this work is shown in Figure 1-1. The main geometric variables are: the tank diameter T , the impeller diameter D , the off-bottom clearance C and the liquid level H . There are four baffles of width $W=T/10$ which are equally spaced around the tank wall at a 90° spacing. In the center of the vessel an impeller is mounted on the shaft and the impeller diameter, D , is usually defined as a fraction of the tank diameter. Overall fluid circulation in the stirred tank depends mainly on the type of impeller. In the case of an axial impeller the flow is directed towards the bottom of the tank. On the bottom the fluid diverges, changing its direction, and then travels upward along the vessel wall. At the top of the tank the fluid is directed radially inward and then redirected down to the impeller closing the circulation loop. In Figure 1-2a the axial circulation pattern for a 45° PBT, as represented by the mean velocity vectors, is plotted. The picture shows a case where two circulation loops exist.

Numerous publications document that the flow field produced by axial impellers is not truly steady but is rather a subject to a large-scale, low-frequency (macro) instability. In Figures 1-2a and b the mean velocity field is compared with the instantaneous velocity field. These vector fields were acquired with the LDV and DPIV techniques and were

first presented by Bakker and Fasano (1995). The mean velocity field is symmetrical with respect to the impeller shaft. At any instant the (instantaneous) velocity flow field in stirred tanks contains a whole spectrum of frequencies due to unstable formations such as eddies and vortices. Close to the impeller blades, there are trailing vortices with dimensions of the order of $D/10$. The macroinstabilities can be visualized as large scale eddies with the dimensions of the order of the tank diameter, T . The macroinstabilities are superimposed on the turbulent random fluctuations with a time scale which is very long compared to the characteristics blade passage frequency (BPF). In what follows, we briefly review the experimental observations published on this phenomenon.

Winardi et al. (1988) were among the first to report that the instantaneous flow field for a paddle impeller (four bladed 90° paddle impeller, $T=0.40\text{m}$, $D=0.16\text{m}$, $C=0.20\text{m}$) is different from the mean velocity field as measured using LDV. Quite different flow patterns and various combinations of patterns appear over time. Flow visualization experiments revealed that the instantaneous flow pattern is asymmetric with respect to the impeller shaft. Three circulation patterns were identified which changed randomly over time. Their lifetime could range from half a second to several minutes.

Kresta and Wood (1993a, 1993b) observed variations in the bulk circulation pattern when they analyzed the flow field of a 45° PBT impeller ($T=0.152\text{m}$, $D=T/2$ and $T/3$, $C/D=0.50$) using flow visualization, LDV, and spectral analysis. A later paper by Chapple and Kresta (1994) considers the influence of geometric parameters such as off bottom clearance, impeller diameter and number of baffles on flow stability for two axial impellers: the Lightnin fluidfoil A310 impeller and the pitched blade turbine (PBT). The authors found that the stability of the flow is different for different geometries but they did not find any geometry with a repeatable coherent pattern. The geometric variables which were most significant for flow stability depended on the type of impeller.

Bruha et al. (1993) investigated 3, 4, and 6 bladed, 45° axial impellers. They studied the effect of impeller rotational speed and the different geometries in which macroinstabilities occur. Their investigations covered two impeller diameters ($D=T/3$ and $T/4$), and three different off-bottom clearances ($T=0.3\text{m}$, $C/T=0.33$, 0.4 and 0.5). They observed a vortex which appears as welling up of the fluid surface close to the baffle,

again on a much longer time and length scale than that of the turbulent eddies. To capture the shape and dimensions of the large vortex they used a video camera. A round probe above the fluid surface was used to measure the frequency of the "surface swelling". They concluded that this frequency is linearly dependent on the impeller rotational speed. The effect of geometry was not systematically examined, although several variations were studied. More recent work from this group (Bruha et al. 1994, 1995, and 1996) uses flow visualization and a special mechanical device called a 'tornadometer'. The tornadometer is placed below the surface in the vicinity of the impeller. The target is deflected whenever macro-instabilities are strong enough to change the direction of the mean flow. The authors were able to confirm their earlier report that the frequency of the macro-instabilities is linearly related to the impeller rotational speed. They also observed that the low frequency macro-instabilities are accompanied by changes in the angle of the impeller discharge flow and the appearance of an unstable secondary circulation loop. This is in agreement with Kresta and Wood (1993a). Bruha et al., (1996) hypothesize that the macroinstability arises from a transition of the flow field from single to double loop circulation. While single loop circulation can be very stable, double loop circulation is inherently unstable due to the weak converging radial flow at the bottom of the tank. The strength of the converging radial flow will be at a maximum when the impeller discharge stream hits the tank wall exactly at the bottom corner of the tank. This condition coincides with the resonant geometry examined in this work.

Montes et al. (1997) used LDV measurements; flow visualization, spectral analysis, and wavelet transforms to analyze flow macroinstabilities in a stirred tank equipped with a six bladed 45° PBT impeller ($T=0.30\text{m}$, $D=T/3$, $C/T=0.35$, four baffles). They suggest that the occurrence of macroinstabilities is accompanied by the presence of a large vortex in the upper part of the vessel, and that it is linearly coupled with the frequency of the impeller revolution. The RMS velocity vs. Reynolds number plot shows a sudden rise in fluctuating intensity at a Reynolds number around 600. They concluded that this change corresponds to the first appearance of the macroinstability. For $Re>600$, the frequency spectrum shows a distinct peak of low frequency oscillations. This shows that both the transitional and fully turbulent flow regimes are subject to this type of instability.

Myers et al. (1997) used digital particle image velocimetry (DPIV) to characterize macroinstabilities in the flow field driven by a four bladed 45° PBT ($T=0.145$ m, $D=0.35T$, $C=0.33T$ and $0.46T$). They analyzed spatially averaged vorticity from DPIV velocity time series covering 40 to 300 impeller revolutions. The authors found that the trailing vortices due to the blade passages did not influence the asymmetries present in the flow. The trailing vortices are restricted to the impeller region: away from the impeller the flow is dominated by the macroinstability.

Hasal, et al. (2000) implemented a new type of analysis to extract the macroinstabilities. They treated the flow field in a mixing vessel as a pseudo-stationary low-dimensional dynamical system. Analysis of the LDV velocity time series was done using proper orthogonal decomposition (POD). The chaotic attractors of the macroinstability were reconstructed using the method of delays. This method was successfully applied at both low and moderate Reynolds numbers. The authors calculated the correlation dimension and the largest Lyapunov exponent λ_{\max} , but they showed that the macroinstabilities have no coherent frequency for the geometry investigated (a six bladed 45° PBT impeller, $T=0.30$ m, $D=T/3$, $C=0.35T$, four baffles) in zones close to the vessel wall, or at high Reynolds numbers.

Industrial scale mixing tanks are significantly larger than the small (laboratory) scales used in all of the aforementioned experiments. The present state of knowledge of scale-up effects on time varying flow in stirred tanks is very limited. This topic was explored by Tatterson and Brodkey (1980) who reported “a number of specific observations” for both bench and industrial scale PBT’s. They studied the flow produced by a six bladed PBT at bench scale and flow produced by a four blade PBT at the large industrial scale at Reynolds numbers beyond the limit of fully turbulent flow. Their case was complicated by the fact that geometric similarity was not maintained- the impeller was changed from a six-blade arrangement at bench scale to a more open four-blade arrangement at the large scale. A special stereoscopic visualization technique was undertaken, making it possible to record a three dimensional picture of the large vortices in a mixing tank. The authors identified two flow structures: high-speed jets driven by the impeller blades and strong trailing vortices. At the bench scale the high-speed jets

drive the flow and contain a large portion of the input energy, creating chaotic and irregular turbulence. The flow patterns at the industrial scale were less chaotic and more coherent. In this case, the predominant flow structure was the strong trailing vortex system formed at the tip of the impeller blades. Even though this study was devoted to investigating the scaling of the trailing vortex system, not the unsteady macroinstabilities, it provides useful information for the velocity field in both large and small-scale tanks and part of it will be used for qualitative validation of the velocity field obtained from large eddy simulations (LES) in Chapter 3.

From this review the macroinstability phenomenon can be summarized as follows:

1. Macroinstabilities are large-scale periodic fluctuations with a period much longer than the blade passages. In order to quantify the frequency of the macroinstabilities, many low-period oscillations need to be acquired.
2. The macroinstability persists in both transitional and fully turbulent flow regimes and scales linearly with the rotational speed of the impeller, N .
3. None of the mixing tank geometries discussed thus far showed a single, coherent frequency observed at more than one location in the tank.

The objectives of this work are:

- 1) to select experimental and numerical tools which will allow successful detection and identification of macroinstabilities.
- 2) to apply this tool for different tank scales, impeller geometries and Reynolds numbers, searching for conditions at which the macroinstabilities become coherent (resonant), meaning that they have single frequency.
- 3) to validate the large eddy simulation approach and use it to probe the macroinstability in more detail at the resonant geometry using computational fluid dynamics (CFD).

The LDV velocity time series used for frequency analysis in this work are Poisson distributed in time and a proper signal analysis technique must be applied. The popular Fast Fourier Transformation (FFT) is not suitable for such unevenly spaced data.

1.2 Frequency analysis of unevenly spaced data

Wide ranges of time and length scales are the defining characteristic of turbulence. The turbulence frequency spectrum is one of the sources from which it is possible to gain some understanding of the turbulent energy distribution, and of the various length scales present in the flow. In addition the turbulence spectrum can reveal any dominant frequencies in the flow field, information which is not available from mean and RMS velocity measurements. This information is vitally important for understanding the dynamics of transport phenomena, reaction rates, and mixing times.

Typical time series of the axial velocity measured in the impeller stream and in the bulk of the tank for the 45° PBT are shown in Figures 1-3 and 1-4. The velocity record shows the turbulent fluctuations, the fluctuations due to the individual blade passages of the impeller, and the fluctuations due to macroinstabilities. In this time series, the high intensity turbulent fluctuations tend to obscure the longer time scale fluctuations. At the other extreme, the mean velocity absorbs in a single value the contribution from the whole frequency spectrum and does not provide any information about the different length scales present in the flow. One way of distinguishing the macroinstabilities is to transform the velocity signal into the frequency domain where dominant periodic or quasi-periodic motions appear as peaks in the frequency spectrum. The transformation from the time domain to the frequency domain can be done easily using the standard fast Fourier transform (FFT) if the input signal is equally sampled. This is not the case for the velocity signals measured with LDV. In the burst detection LDV mode, velocity measurements are taken as particles cross the measuring volume, meaning that the time between the samples follows a Poisson distribution. The random effects of sampling schemes introduce more variability in the calculated frequency spectrum, compared to periodic sampling, but there is another interesting effect. Some random sampling schemes are shown to be alias-free (Shapiro and Silverman, 1960) and Poisson sampling is one of these. In theory there is no upper limit on the frequency range available from an unevenly sampled power spectrum. This is contrast to periodic sampling schemes where

the highest frequency which can be calculated, the Nyquist frequency, is exactly half the sampling frequency:

$$f_c = \frac{1}{2\Delta} \quad (1.1)$$

where Δ is the sampling interval in seconds.

Numerous techniques for recovering the frequency content from LDV data have been proposed in the literature and a short summary of these follows. All methods depend on the characteristics of the signal that is measured and on the signal processing method which is used.

1.2.1 Fast Fourier transform (FFT)

Approximation of unevenly spaced LDV data as evenly spaced combined with direct application of the Fourier transform results in smeared-out and inaccurate frequency spectra and this method is mentioned here only by way of introduction to more appropriate methods.

Every continuous signal can be approximated as a discrete set of equally sampled points with a sampling interval, Δ . The discrete signal can be Fourier transformed by means of

$$H(f_n) = \int_{-\infty}^{+\infty} h(t)e^{2\pi f_n t} dt \approx \sum_{k=0}^{N-1} h_k e^{2\pi f_n t_k} \Delta = \Delta \sum_{k=0}^{N-1} h_k e^{2\pi k n / N} = \Delta H_n \quad (1.2)$$

where $h_k = h(t_k)$ is the discrete evenly sampled set at $t_k = k\Delta$, $k = 0, 1, 2, \dots, N-1$. The H_n is the discrete Fourier transform of the N points of h_k . Numerical implementation of Equation 1.2 involves N^2 complex multiplications. This number is reduced to $N \log_2 N$ operations with the fast Fourier transform (FFT). This algorithm reorders the input data by bit reversal, and applies the Danielson-Lanczos lemma (Press et al., 1989). This reduces significantly the computational time required for calculation of the frequency spectrum.

The FFT is able to calculate the frequency content correctly only if the input data are equally sampled and their total number is a power of two. Series lengths less than a power-of-two can be extended to the desired length by adding trailing zeros to the original data set. This manipulation does not bias the frequencies present in the spectrum. The frequency spectrum can be distorted, however, if one models the unevenly sampled data as an equally spaced sequence by means of any kind of interpolation. A review of various interpolation procedures applied to the LDV signal has been discussed by Antonia and Britz (1996). All interpolation techniques generate new artificial points, which can be modeled as a white noise added to the original signal. This addition low-pass filters the frequency spectrum and shifts the dominant peaks in the low frequency range. All interpolation procedures are computationally intensive and their implications are not clearly defined due to the nature of the turbulent signal.

1.2.2 Autocorrelation methods

A second way of extracting the overall signal characteristics from randomly sampled LDV data is to calculate the (auto)-power spectrum from the Fourier transform of the autocorrelation function. Gaster and Roberts (1975) provide a numerical procedure for these calculations. The randomly sampled lag times are discretized into bins. The mean autocorrelation function is then approximated by a Dirac comb. The values of the spikes of the Dirac comb are taken as being equal to the average value of the neighboring randomly spaced estimates. Then the correlation plane (lag times) is divided into a number of slots and cross product values are accumulated in various store locations appropriate to the lag times. The major advantage of this method is that now, because of the equally spaced bins, an FFT can be used to perform the transform from the autocorrelation to the frequency spectrum; aliasing however, is re-introduced.

A variation on the slotted autocorrelation technique was applied by Grgic (1998) and this technique was not able to accurately resolve the upper frequency part of the spectrum using the LDV time series. The “slotting” technique of Mayo et al. (1974) has been applied to perform reduction of random velocity data into an evenly spaced record. The raw data record was processed by moving a fixed time window through it. All data

points which fall into the window are averaged, and empty windows are filled by interpolation. The resulting data record was in effect sharply low-pass filtered at a Nyquist frequency corresponding to the window size. As a result the high frequency component of the resulting spectrum does not represent the true distribution.

Interpolating for missing data, on the other hand, can modify the true spectrum by increasing the low-frequency content of the signal. Many factors were examined as possible sources of errors such as velocity biasing, ambiguity noise and measurement noise. It was concluded that the combined analysis of the low and high frequency part of the turbulent spectrum requires different tools for analysis and the best approach is to separate this into two different tasks. In this study, we focus only on exact estimation of the dominant low frequencies present in the LDV signal due to macroinstabilities.

Very recently, another technique was proposed for analyzing noisy LDV signals taken at low data rates. This method uses a curve-fit to the autocorrelation function (van Maanen, 1999). The method is called parametric because it is based on prior knowledge of turbulence and it imposes a spectral shape independent of the data. First an analytical expression for the turbulence power spectrum and the autocorrelation function (ACF) are derived. The ACF is fully determined by six parameters. The parameters are optimized to fit the ACF to data obtained from experiments. Additional adjustable parameters are necessary if periodic (or quasi-periodic) components are present in the signal. To avoid the need for this, van Maanen filtered out any low frequency periodic components present in the signal. The technique was tested using LDV and hot-wire anemometry data and the method extended the high frequency part of the power spectrum up to twice the data rate, or more than four decades beyond the noise floor. In the inertial and dissipation ranges, the slope of the power spectrum obtained by the algorithm was accurate. This method is somewhat empirical, because it requires a priori knowledge of turbulence. It may be suitable for the isotropic fully developed turbulent flow conditions but it is not suitable for calculation of unsteady flow, where the quasi-periodic part (such as macroinstabilities) of the spectrum is the primary focus.

Since in this study we want to examine macroinstabilities, which exhibit anisotropic effects and are more closely related to the mean flow than to the purely random turbulence (Roussinova and Kresta, 2000), a technique which is robust and can calculate

only the low frequency content of the spectrum exactly is needed. A numerical method which can operate directly on randomly sampled data is required.

1.2.3 Wavelet analysis

The wavelet transform is a mathematical technique based on group theory and square integrable representation which is capable of providing simultaneously both a wavenumber and a physical space analysis. It uses analyzing functions called wavelets which are localized in space. The scale decomposition is obtained by dilating or contracting the chosen analyzing wavelet before convoluting it with the signal. The limited spatial extent of wavelets is important because the behavior of the signal at infinity does not play any local role. Wavelet analysis can be performed locally on the signal, as opposed to the Fourier transform, which is inherently non-local due to the space-filling nature of the trigonometric functions. In this section we show an example of how the wavelet transform may be used to analyze turbulent time series.

The main problem in applying wavelet analysis to turbulence research is that we have not yet identified the typical “objects” that compose a turbulent field. For instance the Fourier transform would be the appropriate tool if and only if a turbulent flow field was a superposition of harmonic waves; only in this case are wavenumbers well defined and the Fourier energy spectrum meaningful. The cascade models (Kraichnan, 1974) assume that wavenumber octaves (small eddies) are the elementary objects needed to describe homogeneous turbulence and that their interactions consist of exchanging energy with the neighboring octaves. If this theory is true and the turbulent field is a superposition of harmonic waves then the energy density calculated from the wavelet transform should be distributed in phase space among the distinct horizontal bands, each band corresponding to an excited wave number (Farge, 1992). If the turbulent field is a set of localized structures-called coherent structures-the energy density should be distributed among the cone-like patterns, each cone pointed to an excited structure. The hypothesis that turbulence consists mainly of random fluctuations would produce an energy density randomly distributed in both space and scale without presenting any characteristic pattern in phase space. Most probably the turbulent field is a combination

of different phase-space structures which can be separated into different characteristic classes for different types of flows.

Grossman and Morlet introduced equations for the wavelet transform in 1984. In the wavelet transform a signal is broken down into a family of localized wavelets which are obtained by translating and dilating a mother wavelet $\psi(x)$ in such a way that the wavelets remain self-similar. The parameters of the wavelet transform are a location x_0 for translation and a scale s for dilation. The wavelet is defined by

$$\Psi(x, x_0, s) = \frac{1}{\sqrt{s}} \psi\left(\frac{x - x_0}{s}\right) \quad (1.3)$$

where the factor $\frac{1}{\sqrt{s}}$ ensures that the wavelet energy $\frac{1}{s} \int \Psi(x, x_0, s) dx_0$ is conserved at each scale. A function $\psi(x)$ can be a mother wavelet if it is well localized in both physical and wavenumber space and it is admissible. The first requirement means that the wavelet's spread in x-space is given by finite constant $\Delta x = \sigma$, and its spread in k-space is given by $\Delta k = 1/\sigma$ (from uncertainty principle $\Delta x \Delta k \geq 1$). Because of its self-similarity, the wavelet's spread in physical space is σs ; its spread in a wavenumber space is $1/(\sigma s)$; and its norm scales with s^{-1} . Thus, the wavelet transform resolves the small scales finely and the larger scales more coarsely.

The admissibility requirement means that the wavelet must satisfy

$$C_\psi = 2\pi \int_{-\infty}^{\infty} |\hat{\psi}(k)|^2 \frac{dk}{k} < \infty \quad (1.4)$$

where $\hat{\psi}(k)$ is the Fourier transform of $\psi(x)$. This requirement means that the wavelet must have zero mean and ensures that a reconstruction formula exists for the wavelet transform. Practically, these two conditions mean that one chooses a mother wavelet which is an oscillating function (wavenumber space localization) about zero with a rapidly decaying envelope (physical space localization).

The one-dimensional continuous wavelet transformation whose redundancy allows an unfolding of the flow information on the complete scale-space grid is preferred for

turbulence analysis. The continuous wavelet transform of a function or a distribution $u(x)$ is defined as the inner product between $u(x)$ and the wavelet ψ , which gives the wavelet coefficients:

$$CWT = \tilde{u}(x_0, s) = \frac{1}{\sqrt{s}} \int_{-\infty}^{+\infty} u(x) \psi^* \left(\frac{x - x_0}{s} \right) dx \quad (1.5)$$

where ψ^* is the complex conjugate of ψ .

As seen in the above equation, the wavelet transform allows one to investigate the structure of the signal in both physical and wavenumber space. The wavelet transform acts like a mathematical microscope in which the optical characteristics are determined by ψ , and s^{-1} is the magnification at the focal point x_0 .

The wavelet transform is ideally suited to the investigation of coherent structures in turbulence because it allows the definition of the local energy spectrum.

$$W(x_0, s) = |\tilde{u}(x_0, s)|^2 \quad (1.6)$$

By integrating the local energy spectrum $W(x_0, s)$ over a coherent structure it is possible to find the energy spectrum associated with a particular structure. The energy spectrum of the coherent structure then may be compared with the wavelet energy integrated over the whole flow $E_w(s)$

$$E_w(s) = \frac{1}{L} \int_0^L |\tilde{u}(x_0, s)|^2 dx_0 \quad (1.7)$$

(analogous to the Fourier energy spectrum) to determine how that structure contributes to the energy spectrum of the flow as a whole.

The wavelet transform can also be used to detect coherent structures in turbulent flow. Approximate singularities in the flow (such as produced by spiral vortices) appear in the (x_0, s) plane of the wavelet transform as long cones pointing towards the location x_0 of the structure. Strong isolated cones in the wavelet transform are signature of eddies or other approximately singular structures in the flow. By examining the rate of decay of the wavelet transform with s , it is also possible to determine the order of the structure's

singularity (Bacry et al, 1990). Apparent structures in a turbulent flow can thus be both detected (by looking for cones) and characterized (by finding the order of singularity and local energy spectrum) using the wavelet transform.

Usually the wavelets must be complex-valued, because the quadrature between the real and imaginary parts makes it possible to eliminate spurious oscillations of the wavelet coefficients by visualization of their modulus instead of their real part. One of the most commonly used complex valued wavelets is the Morlet wavelet defined as:

$$\psi(x) = \exp(ik_0x) \exp\left(-\frac{1}{2}|x|^2\right) \quad (1.8)$$

(where $k_0=6$ to make the wavelet admissible). This is a plane wave which is modulated by a Gaussian envelop of unit width. The Morlet wavelet is selected because the resulting averaged wavelet energy spectrum is very close to the Fourier energy spectrum making comparison with traditional methods possible (Bonnet et al, 1998).

The continuous wavelet transform was applied to the LDV signal measured just below the impeller tip. To remove the effect of random sampling, the time series was first resampled with a “sample and hold” interpolation technique at a sampling frequency equal to the average sampling frequency. The continuous wavelet transform was performed using the Morlet wavelet (Equation 1.8). It is possible to compute the wavelet transform in the physical domain using Equation 1.5 directly: however, it is much simpler to use the fact that the wavelet transform is the convolution between two functions $u(x)$ and ψ , and to carry out the wavelet transform in Fourier space using the FFT algorithm. The first step of this algorithm computes separately the Fourier transform of the time series and the Fourier transform of the Morlet wavelet that is known analytically as

$$\hat{\psi}(k) = \sqrt{\pi} \exp(-(k - k_0)^2 / 4) \quad (1.9)$$

The ‘hat’ indicates a Fourier transformed quantity. The wavelet coefficients in the Fourier space are then computed using the relation

$$\hat{u}(k, s) = s^{-1/2} s \hat{\psi}(sk) \hat{u}(k) \quad (1.10)$$

From the Fourier space, the wavelet transform at each scale is transformed back to the physical space using the inverse FFT algorithm. This method of computing the wavelet transform brings out the role of the wavelet as a sort of Fourier-space filter and is much more efficient than carrying out the convolution in physical space. This method is ideal for a structural analysis since an arbitrary number and distribution of scales can be chosen.

Two examples of a continuous wavelet transform applied to the test signal and the LDV signal measured just below the impeller tip are shown in Figures 1-5 and 1-6. The absolute values of the wavelet coefficients, $\tilde{u}(x_0, s)$ at all scales are colored in shades of gray. The horizontal axis is the translation axis (location in the time series) and the vertical axis is the scale or dilatation axis (analogous to the wavenumber or period) on a logarithmic scale. The plots are constructed as follows: at every time, the absolute value of the wavelet coefficient, for a fixed scale a , is calculated. Because the scales are varied continuously a set of the wavelet coefficients are obtained at each instance. In order to represent that on a 2-D plot the amplitudes of the wavelet coefficients are depicted as a color map.

For comparison, both the test signal (Figure 1-5a) and the velocity signal (Figure 1-6a) are also given in the time domain. The LDV signal has 3000 points which are rearranged at a sampling interval of $\Delta=0.015$ s. The continuous wavelet transform reveals the presence of a large number of scales as should be expected from a signal taken close to the impeller blade. The signal exhibits some apparent “scale” pattern, which has fractal structure. The light stripes are an indication of the presence of a strong oscillating component in the signal. The number of stripes at different scales can be related either to the blade passages, N_{BP} at the small scale around 140, or low frequency macroinstabilities, N_{MI} at the large scale of 225. Signal recognition criteria for wavelet analysis are not well established and further research is needed.

Wavelet filtering was also used to calculate the power of the signal at every scale band. The filtering was performed using Daubechies wavelets with four coefficients (Press et al, 1989). After applying the wavelet filtering, the signal was decomposed into 7 levels each containing a different frequency band. Next the decomposed parts of the

signal at every level were transformed back in to the time domain with an inverse wavelet transform. Finally the standard FFT algorithm was applied to each of them and the power content was calculated. Close to the impeller blade the FFT transform shows that 80% of the signal power is concentrated in the blade passages rather than in the low frequency macroinstabilities. The strength of the blade passage frequency decays rapidly and in the bulk of the tank and in the baffle region, the maximum signal power is concentrated in the low frequency macroinstability.

The wavelet transform can be considered as a complementary tool to FFT for analysis of turbulent signals. It can provide information about the scales (structures) present in the signal at each instant in time. However, the method in its present form suffers from the same disadvantage as the Fourier transforms: the time series of interest have to be equally spaced.

1.2.4 Lomb periodogram

The Lomb spectral method was originally developed by Lomb (1976) for astronomic time series analysis. In astronomical data, the most important objective is generally to detect periodicity in the data and the signal is composed of sharp peaks and white background noise. Like the binned autocorrelation method (Gaster and Roberts, 1977) the Lomb periodogram uses exact time information; however, this method was developed specifically for the detection of narrow peaks corresponding to periodic components in the signal.

Spectral analysis of a set of unevenly spaced data is far more complex than spectral analysis of a uniform set of data mostly because there is no frequency range in which a period is unambiguously defined. Each true peak in the spectrum gives rise to a number of other peaks (aliases) of various heights, distributed through the spectrum. As a consequence no more than one period can be determined for any one calculation of the spectrum because of possible confusion with the alias structure of the major peak. Subsequent periods have to be found by successively subtracting the previous

periodicities from the data. Periodogram analysis is the most suitable technique for calculating the frequency spectrum from an unequally spaced set of data.

The Lomb method is based on general transformation theory (Oppenheim and Willsky, 1983), which shows that the projection of the signal $x(t)$ onto the element of an orthonormal basis $b_i(t)$ is the value, c that minimizes the mean square error energy E . E is the integral of the squared differences between $x(t)$ and $c \cdot b_i(t)$ over the definition interval. The Lomb method implements this minimization procedure over the unevenly distributed sampled values of $x(t)$ using a Fourier kernel $b_i(t) = \exp(j2\pi f_i t)$ basis function.

Suppose that x_n is a discrete signal, where $x_n = x(t_n)$, $n = 1..N$, and $b_i(t)$ is an orthogonal basis set which defines the transform by

$$x_n = \sum_i c_i b_i(t_n) \quad (1.11)$$

Multiplying both sides of Equation 1.11 by $b_k(t_n)$ and summing over n gives

$$\sum_n x_n b_k(t_n) = \sum_i \sum_n c_i b_i(t_n) b_k(t_n) \quad (1.12)$$

For the right side of Equation 1.12, applying the orthogonality condition given as

$\sum_n b_i(t_n) b_k(t_n) = \delta_{ik}$ we obtain that

$$\text{RHS} = \sum_i c_i \sum_n b_i(t_n) b_k(t_n) = \sum_i c_i \delta_{ik} = c_k \quad (1.13)$$

The coefficients c_k that represent the x_n in the transformation domain are thus given as

$$c_k = \sum_n x_n b_k(t_n) \quad (1.14)$$

Thus, the squared difference error, E , can be defined as the difference between the true signal x_n and its transformed value:

$$E = \sum_n \varepsilon_n^2 = \sum_n \left(x_n - \sum_i c_i b_i(t_n) \right)^2 \quad (1.15)$$

The constant coefficients c_i are those which minimize the squared error Equation 1.15. In the case of evenly sampled data in the Fourier domain Equation 1.15 is known as the discrete time Fourier transform (DTFT), its discretely evaluated version (DFT) and the associated fast algorithm used to compute it as (FFT). When the signal is available only at unevenly spaced time instants Lomb proposed to estimate the Fourier spectra by adjusting the model given as

$$x(t_n) + \varepsilon_n = a \cos 2\pi f_i(t_n - \tau) + b \sin 2\pi f_i(t_n - \tau) \quad (1.16)$$

in such a way that the error E is minimized with the proper a and b parameters. In the original work, Lomb introduces a delay, τ at the basis, which becomes a more efficient estimation algorithm. The mean square error or functional $E(a, b)$ that has to be minimized is defined as

$$E(a, b) = \sum_n [x_n - a \cos 2\pi f_i(t_n - \tau) - b \sin 2\pi f_i(t_n - \tau)]^2 \quad (1.17)$$

where x_n is a signal with zero mean. The $E(a, b)$ will be minimum if both derivative

$\frac{\partial E(a, b)}{\partial a}$ and $\frac{\partial E(a, b)}{\partial b}$ are equal to zero. Adopting the notation

$$\begin{aligned} CC &= \sum_n \cos^2 2\pi f_i t_n, \quad SS = \sum_n \sin^2 2\pi f_i t_n, \\ CS &= \sum_n \cos 2\pi f_i t_n \sin 2\pi f_i t_n \\ XC &= \sum_n x_n \cos 2\pi f_i t_n, \quad XS = \sum_n x_n \sin 2\pi f_i t_n \end{aligned} \quad (1.18)$$

we are led to solve the normal equations

$$\begin{bmatrix} CC & CS \\ CS & SS \end{bmatrix} \begin{bmatrix} a \\ b \end{bmatrix} = \begin{bmatrix} XC \\ XS \end{bmatrix} \quad (1.19)$$

After solving the Equation 1.19 we obtain the following expressions for parameters a and b

$$a = \frac{XC SS - XS CS}{SS CC - CS^2}, \quad b = \frac{XS CC - CS XC}{SS CC - CS^2} \quad (1.20)$$

to minimize E .

By definition the signal power is $P = \sum_n x_n x_n^*$ where x_n^* is a complex conjugate. In the case of real signal the power simply becomes

$$P = \sum_n x_n^2 \quad (1.21)$$

First, we want to calculate the power of the signal using the model expression given in Equation 1.16. Second we want to compare this value with the power calculated from the real signal. The expected ratio between these two values has to lie in the range 0 to 1. By substituting Equation 1.16 into Equation 1.21 we obtain the expression for P_{model} :

$$P_{model} = a^2 CC + b^2 SS + 2abCS = a(aCC + bCS) + b(bSS + aCS) \quad (1.22)$$

Substituting the solutions for parameters a and b (Equation 1.20) into the brackets of Equation 1.22 we derive the theoretical power of the signal based on the model proposed by Lomb:

$$P_{model} = aXC + bXS \quad (1.23)$$

In matrix notation

$$P_{model} = \begin{pmatrix} XC & XS \end{pmatrix} \begin{bmatrix} SS/D & -CS/D \\ -CS/D & CC/D \end{bmatrix} \begin{pmatrix} XC \\ XS \end{pmatrix} \text{ where } D = CC SS - CS^2$$

By choosing the delay τ , as

$$\tan(2\omega\tau) = \frac{\sum_{n=1}^N \sin 2\omega t_n}{\sum_{n=1}^N \cos 2\omega t_n} \quad (1.24)$$

the CS becomes 0 for all values of τ and then the theoretical power of the signal is

$$P_{model} = \begin{pmatrix} XC & XS \end{pmatrix} \begin{bmatrix} 1/CC & 0 \\ 0 & 1/SS \end{bmatrix} \begin{pmatrix} XC \\ XS \end{pmatrix}. \text{ Hence} \quad (1.25)$$

$$P_{model} = \left(\frac{XC^2}{CC} + \frac{XS^2}{SS} \right)$$

The power calculated from the model is then normalized by the actual power, P_{real} given with Equation 1.21. Finally, the Lomb normalized periodogram (spectral power as a function of angular frequency $\omega = 2\pi f > 0$) is defined by

$$P_N(\omega) \equiv \frac{1}{P_{real}} \left\{ \frac{\left[\sum_{n=1}^N x(t_n) \cos(\omega(t_n - \tau)) \right]^2}{\sum_{n=1}^N \cos^2 \omega(t_n - \tau)} + \frac{\left[\sum_{n=1}^N x(t_n) \sin(\omega(t_n - \tau)) \right]^2}{\sum_{n=1}^N \sin^2 \omega(t_n - \tau)} \right\} \quad (1.26)$$

The delay τ is a kind of offset that makes $P_N(\omega)$ completely independent of shifting all the t_i 's by any constant. It makes Equation 1.26 identical to the equation obtained if one estimated the harmonic content of a data set, at given frequency ω , by linear least squares fitting.

The Lomb method is absolutely free from aliasing and it can find spectral peaks at frequencies that are as much as fifty times higher than Nyquist frequency. The integral of the estimated spectrum depends strongly on the highest frequency for which the estimate is calculated. That maximum frequency is not necessarily limited to some given value, so the Lomb spectrum defined by Equation 1.26 has no direct interpretation as a distribution of power over the frequencies. The Lomb algorithm is a slow algorithm which requires $N_\omega N$ operations in order to calculate N_ω frequencies from N data points. The C++ code implementing the Lomb method, including also the routine **PERIOD** (Press et al, 1989), is given in Appendix.

1.3 Conclusions

In this section a review of different techniques for signal analysis of the burst detected LDV time series is presented. The signal analysis task is not trivial because the velocity measurements are unequally sampled and therefore the standard methods of analysis based on the Fourier transform are unsuitable. This creates a numerical problem when one wants to extract unbiased information for the frequencies present in such signals. Selection of an appropriate method, one which can analyze the velocity data for unknown periodicities, underlies a systematic methodology for further detection and analysis of the large-scale macroinstabilities present in the flow.

It was shown that the random sampling could be overcome using the Lomb periodogram algorithm. The Lomb algorithm approximates the data with a least-square minimization procedure which evaluates frequencies at the times that are actually measured. The algorithm statistically verifies the significance of every frequency peak and so it is able to resolve very narrow frequency oscillations. This method is excellent for accurate reconstruction of the low frequency content from the unequally spaced LDV signals. The mathematical estimate for the Lomb power spectrum, given by Equation 1.26, cannot be related directly to the power calculated with the standard FFT. An alternative method to assess the relative power contribution in different frequency bands applies a wavelet filtering procedure to the interpolated LDV signal and then calculates the power content of the filtered signal using the FFT algorithm. For signals measured in the vicinity of the impeller blades, the maximum power is concentrated in the blade passage frequency. Close to the tank wall and at the baffle region, the maximum power is concentrated into the low frequency component due to the macroinstabilities. A further continuous wavelet transform was applied to the same signal and it revealed a fractal structure (see Figure 1-6) due to the presence of the large number of scales.

1.4 Nomenclature

$a=$	parameter
$b=$	parameter
$b_i(t)=$	orthonormal basis function, Fourier kernel, $\exp(j 2 \pi f_i t)$
$C=$	impeller off bottom clearance (m)
$CC=$	Lomb notation, $\sum_n \cos^2 2\pi f_i t_n$
$CS=$	Lomb notation, $\sum_n \cos 2\pi f_i t_n \sin 2\pi f_i t_n$
$C_\psi=$	wavelet admissibility constant, $2\pi \int_{-\infty}^{\infty} \hat{\psi}(k) ^2 \frac{dk}{k} < \infty$
$c=$	constant
$D=$	impeller diameter (m)
$E=$	mean square energy
$E_w(s)=$	wavelet energy integrated over the whole flow, $\frac{1}{L} \int_0^L \tilde{u}(x_0, s) ^2 dx_0$
$f=$	frequency, Hz
$f_{MI}=$	frequency of macroinstabilities, Hz
$f_c=$	Nyquist frequency, (Hz), $f_c = \frac{1}{2\Delta}$
$j=$	square root of -1
$H=$	continuous Fourier transform,
$H_n=$	discrete Fourier transform
$h_k=$	discrete equally sampled signal, $h(t_k)$
$i=$	index of summation
$k=$	index of summation
$\Delta k=$	wavelet's spread in k-space
$N=$	impeller rotational speed (rpm or s^{-1})
$N_w=$	number of frequencies
$N_w N=$	number of numeric calculations
$P=$	general definition of a signal power, $\sum_n x_n x_n^*$
$P_{model}=$	theoretical Lomb power, $aXC + bXS$

P_N	Lomb normalized periodogram
r	radial position (m)
Re	impeller Reynolds number, $\frac{ND^2}{\nu}$
SS	Lomb notation, $\sum_n \sin^2 2\pi f_n t_n$
s	wavenumber or scale
T	tank diameter, (m)
t	time, s
XC	Lomb notation, $\sum_n x_n \cos 2\pi f_n t_n$
XS	Lomb notation, $\sum_n x_n \sin 2\pi f_n t_n$
x_0	parameter of the wavelet transform
x_n	signal or time series with zero mean, $x(t_n)$
x_n^*	complex conjugate of x_n
Δx	wavelet's spread in x-space
$u(x)$	function or distribution
$\hat{u}(k)$	function in the Fourier space
$\tilde{u}(x_0, s)$	wavelet coefficients, $\frac{1}{\sqrt{s}} \int_{-\infty}^{+\infty} u(x) \psi^* \left(\frac{x-x_0}{s} \right) dx$
$\hat{\tilde{u}}(k, s)$	wavlet coefficients in the Fourier space, $s^{-1/2} s \hat{\psi}(sk) \hat{u}(k)$
$W(x_0, s)$	wavelet local energy spectrum, $ \tilde{u}(x_0, s) ^2$

Greek

Δ	sampling interval, (s)
δ_{ik}	Dirak delta function
π	Pi constant
ν	fluid viscosity
ρ	fluid density
ω	angular velocity,
τ	time delay, $\tan(2\omega\tau) = \frac{\sum_{n=1}^N \sin 2\omega t_n}{\sum_{n=1}^N \cos 2\omega t_n}$

ϵ_n	=	error
λ_{\max}	=	Lyapunov exponent
$\psi(x)$	=	mother wavelet
$\hat{\psi}(k)$	=	Fourier transform of the wavelet
$\psi^*(x)$	=	complex conjugate
$\Psi(x, x_0, s)$	=	wavelet, $\frac{1}{\sqrt{s}} \psi\left(\frac{x - x_0}{s}\right)$
σ	=	constant

Abbreviations

ACF	=	autocorrelation function
A310	=	three bladed aerofoil impeller by Lightnin'
BPF	=	blade passage frequency
CWT	=	continuous wavelet transform
DFT	=	discrete Fourier transform
DTFT	=	discrete time Fourier transform
DPIV	=	digital particle image velocimetry.
FFT	=	fast Fourier transform
HE3	=	three bladed high efficiency turbine by Chemineer
MI	=	macroinstability
LDV	=	laser Doppler velocimeter
PBT	=	four bladed, 45° pitched blade turbine
POD	=	proper orthogonal decomposition
RMS	=	root mean square

1.5 References

1. Antonia R. A. and D. Britz 1996, *A comparison of methods of computing power spectra from LDV signals*, Meas. Sci. Technol., **7** 1024-1053.
2. Bacry E., Arneodo A., Frisch U., Gagne Y., Hopfinger E., 1990, *Wavelet analysis of fully developed turbulence data and measurement of scaling exponents*. In: *Turbulence and coherent structures*, Dordrecht, Kluwer, 203-215.
3. Bakker A and Fasano J. B., 1995, *Stirred tank flow pattern study using digital particle image velocimetry*. Presented at the 1995 Annual meeting, November 1995, Miami Beach Session 123, paper 123c.
4. Bittorf, K., 2000, *The application of wall jets in stirred tanks with solids distribution*, PhD thesis (University of Alberta, Canada).
5. Bonnet J. P, Delville J, Glauser M.N, Antonia R. A, 1998, *Collaborative testing of eddy structure identification methods in free turbulent shear flow*, Exp. in Fluids, **25**, 197-225.
6. Bruha, O., I. Fort, and P. Smolka, 1993, *Large scale unsteady phenomenon in a mixing vessel*, Acta Polytechnica, Czech Tech. Univ. Prague, **27** 33.
7. Bruha O., I. Fort, and P. Smolka, 1994, *Flow transition phenomena in an axially agitated system*. Proceedings of the VIII European Conference on Mixing (IChEME Symposium series **136**), 121-128, Cambridge UK.
8. Bruha O., I. Fort, and P. Smolka, 1995, *Phenomenon of the turbulent macro instabilities in agitated systems*, Collect. Czech.Chem Commun, **60**, 85-94.
9. Bruha, O., I. Fort, P. Smolka, and M. Jahoda, 1996, *Experimental study of turbulent macroinstabilities in an agitated system with axial high-speed impeller and with radial baffles*, Coll. Czech. Chem. Comm., **61**, 856-867.
10. Farge M, 1992, *Wavelet transforms and their applications to turbulence*, Annu. Rev. Fluid Mech, **24**, 395-457
11. Gaster M. and J. B. Roberts, 1977, *The spectral analysis of randomly sampled records by direct transform*, Proc. R. Soc. London A, **354**, 27-58.
12. Gaster M. and J. B. Roberts, 1975, *Spectral analysis of randomly sampled signals*, Journal of the Institute of mathematics and its applications, **15**, 195-216.
13. Grgic B., 1998, *Influence of the impeller and tank geometry on low frequency phenomena and flow stability*, MSc thesis (University of Alberta, Canada).

14. Hans Rudi Eduard van Maanen, 1999, *Retrieval of turbulence and turbulence properties from randomly sampled Laser-Doppler anemometry data with noise*, PhD thesis, Amsterdam, The Netherlands
15. Hasal, P., J.-L. Montes, H.-C. Boisson and I. Fort, 2000, *Macro-instabilities of velocity field in stirred vessel: detection and analysis*, Chem. Eng. Sci, **55**, 391-401.
16. Kraichnan R.H, 1974, *On Kolmogorov's inertial range theories*, J. Fluid Mech. **62**, 305-30.
17. Kresta, S.M. and P.E. Wood, 1993a, *The flow field produced by a pitched blade turbine: Characterization of the turbulence and estimation of the dissipation rate*, Chem. Eng. Sci. **48**, 1761-1774.
18. Kresta, S.M. and P.E. Wood, 1993b, *The mean flow field produced by a 45° Pitched Blade Turbine: changes in the circulation pattern due to off-bottom clearance*, Can. J. Chem. Eng. **71**, 42-53.
19. Lomb N. R., 1976 *Least-squares frequency analysis of unequally spaced data*, Astrophysical J., **39**, 447-462
20. Mayo W.T, 1974, *A discussion of limitations and extensions of power spectrum estimation with burst counter LDV systems*, In proceedings of the second international workshop on Laser velocimetry, 90-104, Purdue University.
21. Montes, J.L., H.C. Boisson, I. Fort, and M. Jahoda, 1997, *Velocity field macro-instabilities in an axial agitated mixing vessel*, Chem. Eng. J, **67**, 139-145.
22. Myers, K.J., R.W. Ward, and A. Bakker, 1997, *A digital particle image velocimetry investigation of flow field instabilities of axial flow impellers*, J. Fluids Eng., **119**, 623-632.
23. Oppenheim, A.V. and A.S. Willsky, 1983, **Signal and systems**, Englewood Cliffs, NJ: Prentice-Hall
24. Press, W.H., B.P. Flannery, S.A. Teukolsky, and W.T. Vetterling, 1989, **Numerical recipes, The art of scientific computing**, Cambridge University Press, New York.
25. Roussinova V., B. Grgic, S. M. Kresta, 2000 *Study of macro-instabilities in stirred tanks using a velocity decomposition technique*, Trans IChemE, **78**, Part A, 1040-1052.
26. Shapiro and Silverman, 1960, *Alias free sampling of random noise*, J. SIAM, **21**, 714-719.
27. Tatterson and Brodkey, 1980, *Stereoscopic visualization of the flows for pitched blade turbines*. Chem. Eng. Sci. **35**, 1369-1375.
28. Winardi, S., S. Nakao, and Y. Nagase, 1988, *Pattern recognition in flow visualization around a paddle impeller*, J.Chem.Eng. Japan, **21**, 503-508.

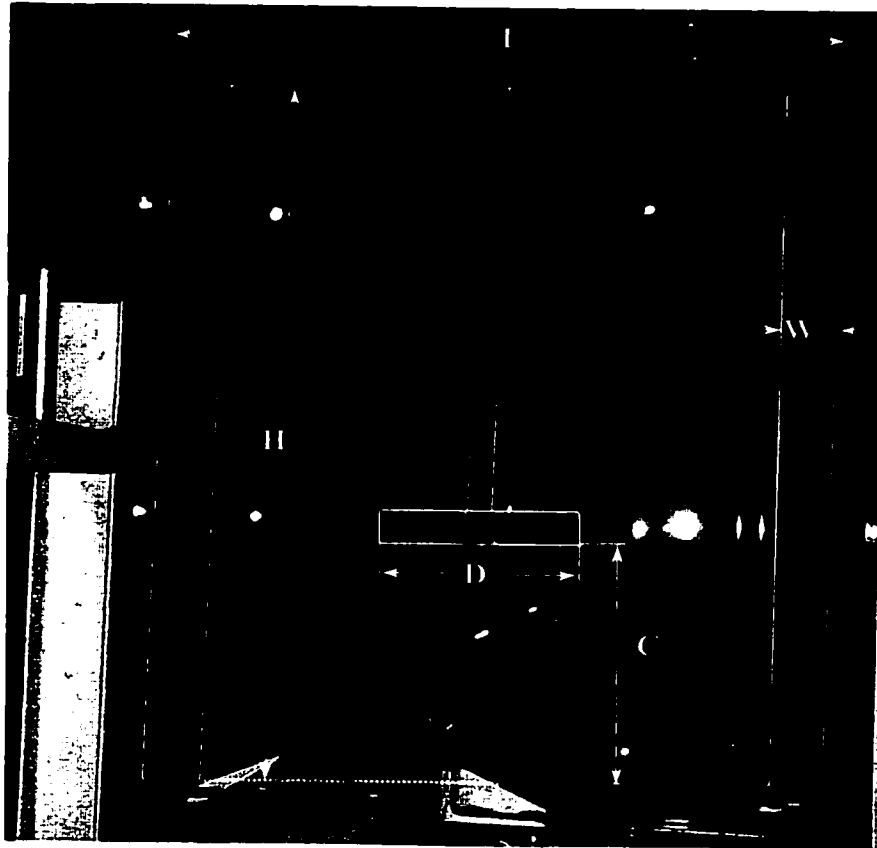


Figure 1-1. Geometry of stirred tank as defined for this work.

a) Mean velocity field

b) Instantaneous velocity field

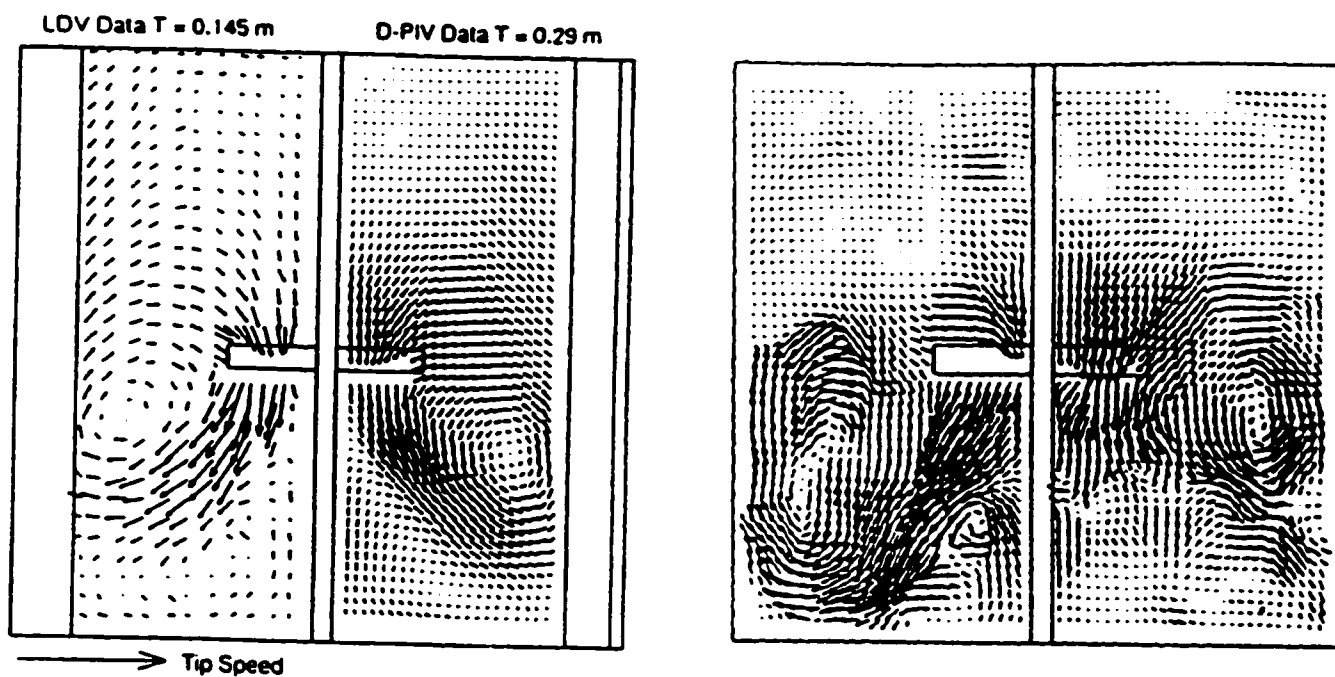


Figure 1-2. Comparison between the mean and instantaneous velocity fields for the 45° PBT. Data from Bakker and Fasano (1995).

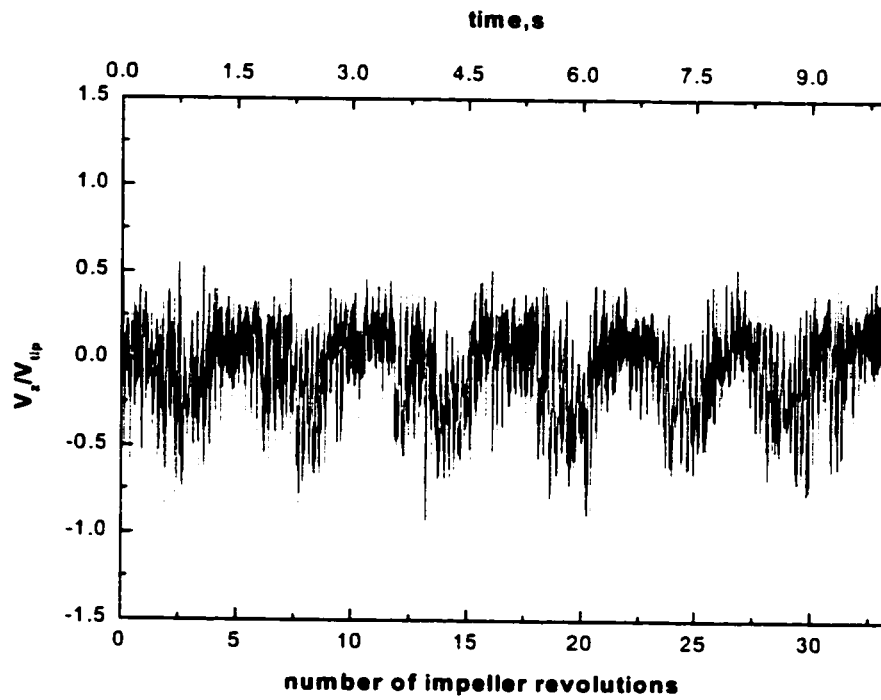


Figure 1-3. BPF and macroinstabilities (MI) evident in the impeller stream (45° PBT, $C/D=0.5$ and $D=T/2$, fluid water, $Re=48,000$).

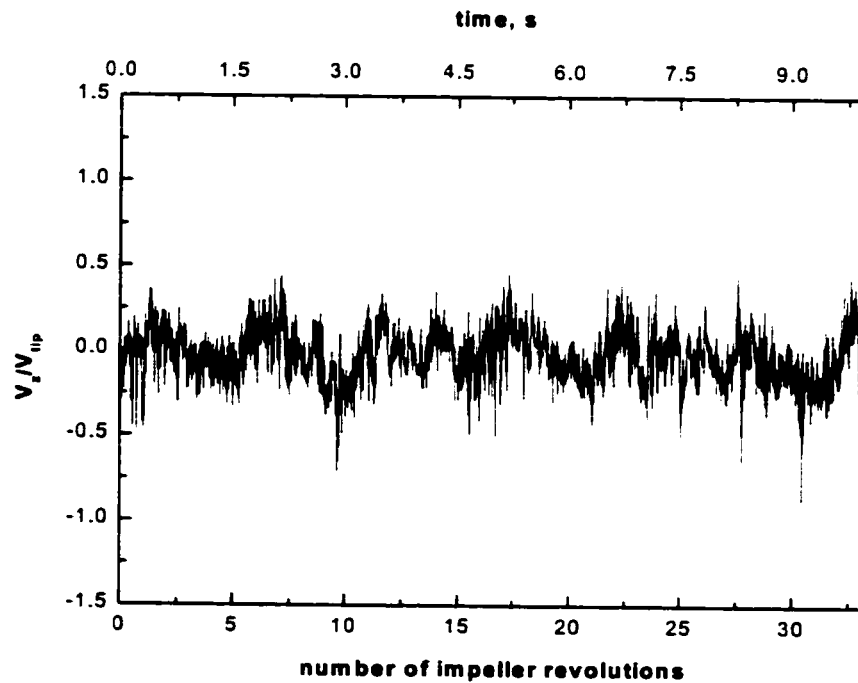
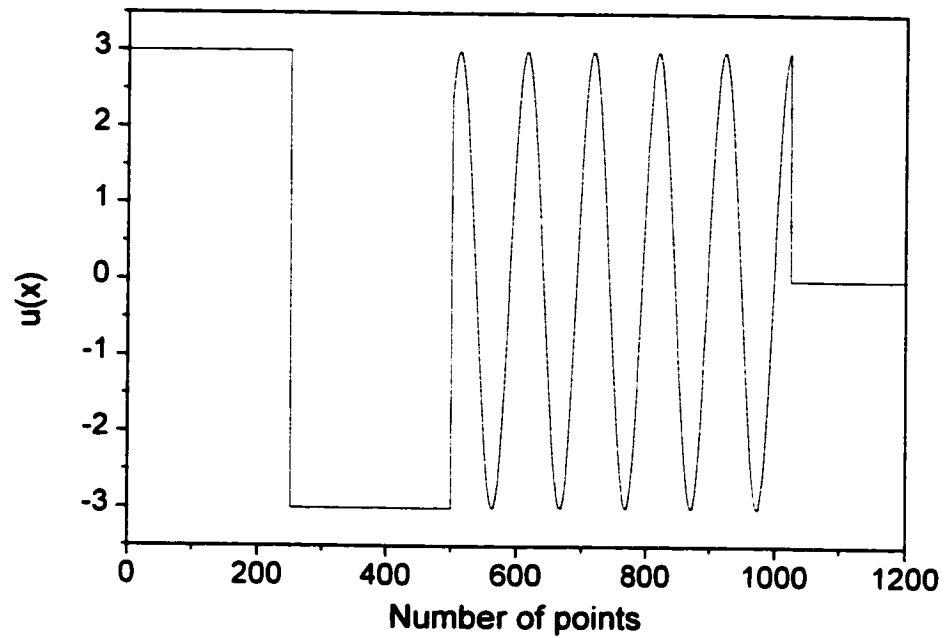


Figure 1-4. Decay of the BPF in the upper part of the tank: only the macroinstabilities and the turbulence persist (45° PBT, $C/D=0.5$ and $D=T/2$, fluid water, $Re=48,000$).

a)



b)

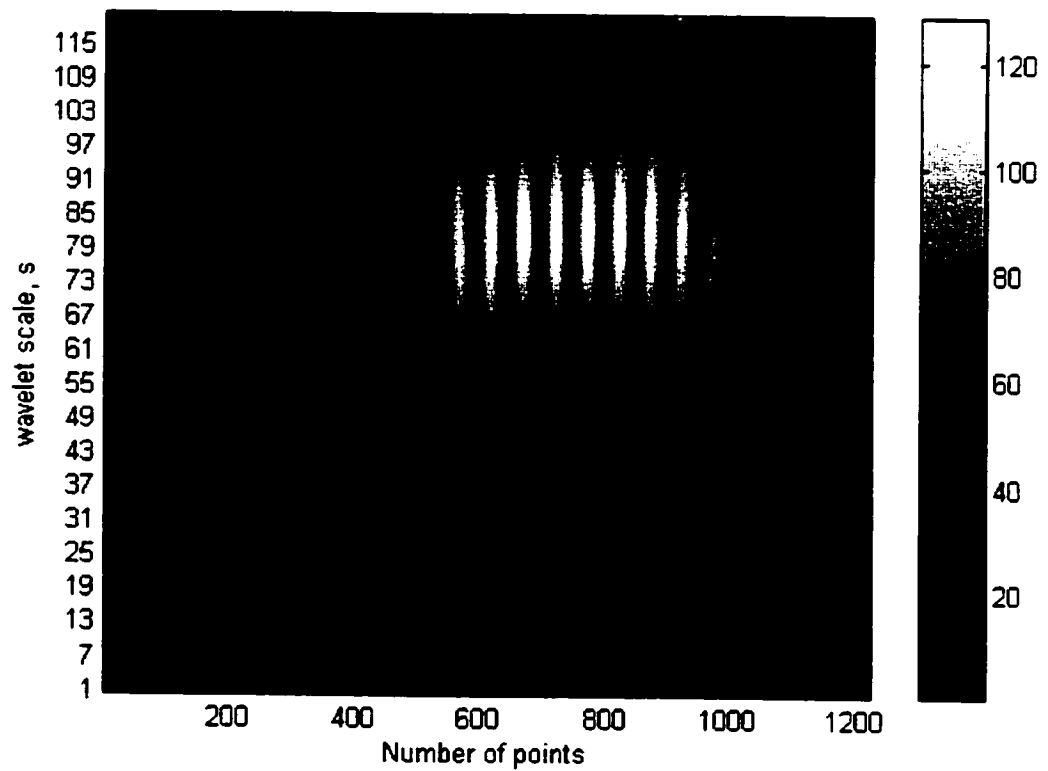


Figure 1-5. A test signal (a) and its continuous wavelet transform using the Morlet wavelet (b). The periodic oscillations are represented by vertical dark and white stripes. The cones are also visible at the location of signal singularities.

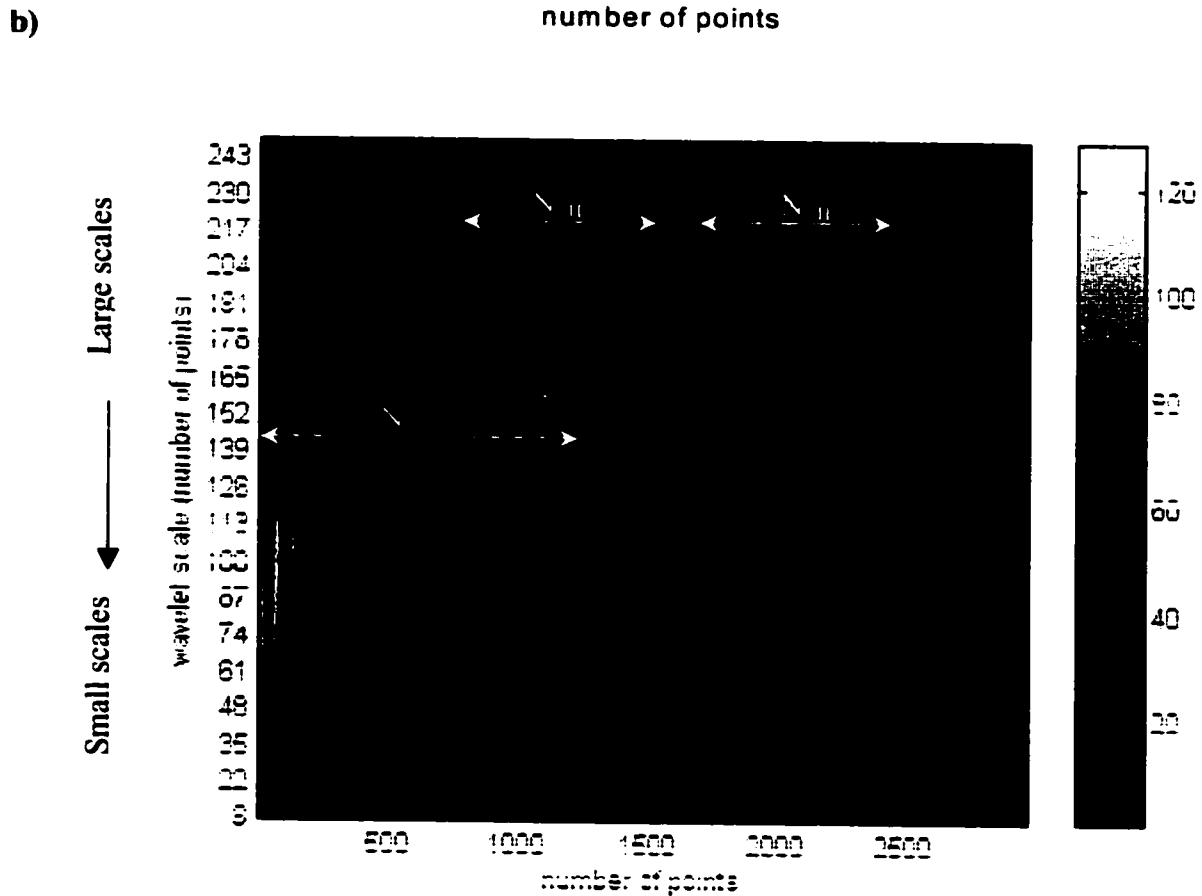
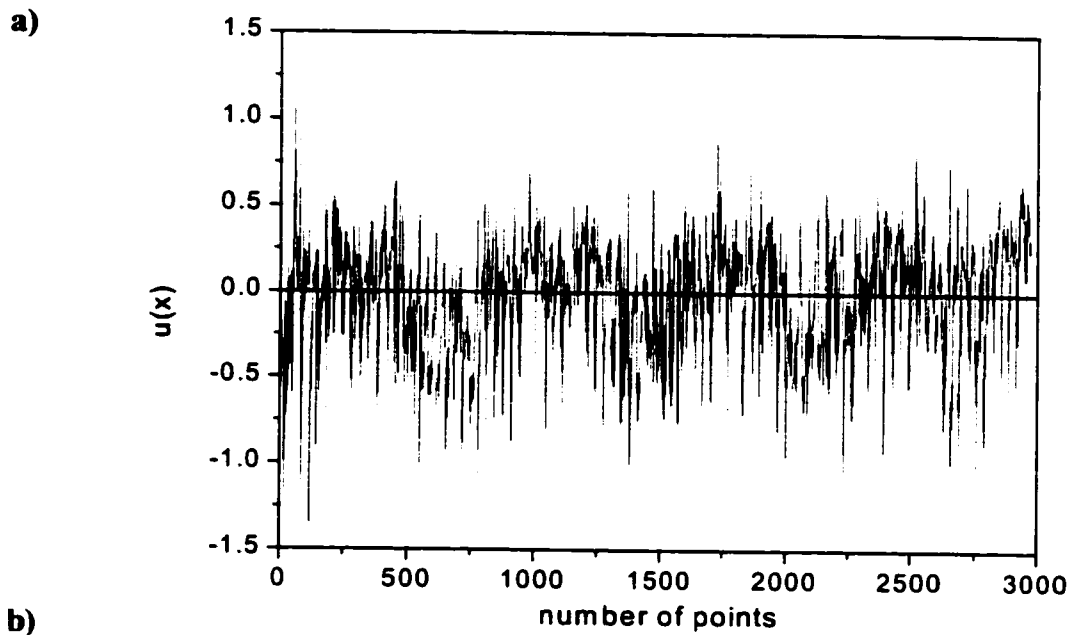


Figure 1-6. A sample LDV signal (a) and its continuous wavelet transform using the Morlet wavelet (b). We visualize the absolute values of the wavelet coefficients vs. the number of examined data points. N_{MI} represents the periodicity due to MI, and N_{BP} represents the periodicity due to blade passages.

1.6 Appendix

```

/*****
Lomb periodogram routine
This code has to be compiled and build as executable file.
*****/

//x[i]→input time
//y[i]→input velocity
//ASCII data file exported from the RSA.
//The program subtracts the mean from the velocity data.

#include <stdio.h>
#include <math.h>
#define NRANSI
#include <nr.h>
#include <nrutil.h>
#include <nrutil.c>
#include <period.c>
#include <avevar.c>

#define TWOPI 6.2831853

int main(int argc, char *argv[])
{

    int n,i;
    long int np,NPR,nout;
    long idum=(-4);
    int j,jmax;
    float prob,*px,*py,*x,*y;
    float pom1,pom2;

```

```

float ofac,hifac,fc,fhi,T;

FILE *infile,*outfile;
printf("Start: ");
printf(argv[1]);printf("\n");

    if ((infile = fopen(argv[1], "r")) == NULL)
        {
            fprintf(stderr, "Cannot open input file.\n");
            return 1;
        }
    if ((outfile = fopen(argv[2], "wt")) == NULL)
        {
            fprintf(stderr, "Cannot open output file.\n");
            return 1;
        }

i=0;
while (!feof(infile))
    {
        i++;
        fscanf(infile, "%f\t", &pom1); fscanf(infile, "%f\n", &pom2);
    }

close(infile);
if ((infile = fopen(argv[1], "r")) == NULL)
    {
        fprintf(stderr, "Cannot open input file.\n");
        return 1;
    }

n=i;

```

```

x=vector(1,n);
y=vector(1,n);
for (i=1;i<=n;i++)
    {
        fscanf(infile, "%f\t", &pom1); fscanf(infile, "%f\n", &pom2);
        x[i]=pom1;y[i]=pom2;
    }

close(infile);

T=x[n]-x[1];
// T→is the time period of the input data
ofac=4.0;
// ofac→oversampling parameter equal to 4.
fc=n/(2*T);
//fc→ is Nyquist frequency. defined as if the input data are equally spaced
hifac=1.0;
// hifac → ratio between the fhi/fc. In all calculations the hifac is equal to 1.0
fhi=fc*hifac;
np=(long int)(ofac*hifac*n/2.0);
// np → This is the number of different frequencies returned by the program.

px=lvector(1,np);
py=lvector(1,np);
period(x,y,n,ofac,hifac,px,py,np,&nout,&jmax,&prob);
printf("nout,jmax,prob=%d %d %12.6g\n",nout,jmax,prob);
NPR=np;
for (j=LMAX(1,jmax-NPR/2);j<=LMIN(nout,jmax+NPR/2);j++)
    fprintf(outfile,"%d %12.6f %12.6f\n",j,px[j],py[j]);

/*for(i=1;i<=n;i++)
    {
        fprintf(outfile,"%12.6f %12.6f\n",x[i],y[i]);
    }

```

```
        }  
    /*      close(outfile);  
    printf("End: ");  
    printf(argv[2]);printf("\n");  
    free_lvector(py,1,np);  
    free_lvector(px,1,np);  
    free_vector(y,1,n);  
    free_vector(x,1,n);  
    return 0;  
    }  
#undef NRANSI
```

Chapter 2: Experiments and Results

Organized (coherent) flow structures superimposed on the turbulent flow are found in many shear flows of practical importance such as mixing layers (Roshko, 1976), jets and wakes (Grant, 1958). “*Coherent structures*” form part of the considerable organized structure present in the flow, and maintain their structure for some time. Under turbulent flow conditions, it is usually the large energy-containing scales that exhibit the most evident structure. In any given situation one may expect to find organized structures; the relative strength of the coherent structures is a function of the inflow conditions, of the type of flow, and of the spatial location of interest (distance downstream). These structures may be remnants of instabilities in the laminar flow, or they may have developed from instabilities of the turbulent flow itself.

In a mixing tank such visible flow structures are called macroinstabilities. The macroinstabilities exhibit very low period velocity fluctuations and they are characterized by a time scale much longer than the impeller blade passages. The macroinstabilities can affect not only the mechanical integrity of the mixing vessel but also the processes undertaken in mixing tanks. Basic blending operations such as dissolving solids, chemical reactions, flocculation, and precipitation can be very sensitive to the local conditions of turbulence in the vessel. Large-eddies can cause a significant heterogeneity of the turbulence level, especially in the bulk of the vessel. For continuous operations care should be taken when two streams of reactants have to be brought in contact. The presence of large-scale macroinstabilities can cause an intermittency of the feed stream jet which may strongly influence the kinetics of fast reactions. Therefore care should be taken when selecting the feed location, taking into account the presence of large-scale macroinstabilities, as discussed by Houcine et al. (1999).

The latter brings us to the main objectives with which the macroinstability analysis was undertaken. First the resonant geometries at which the macroinstabilities have a coherent (single) frequency are to be identified. For this reason the velocity time series from three different axial impellers; 45° pitched blade turbine (45° PBT), Lightnin fluidfoil A310 and Chemineer HE3 were examined. Because the inflow conditions for a fixed vessel size are set by the impeller diameter, D , and the off-bottom clearance, C , by changing both parameters we were able to find a favorable geometrical configuration at

which the macroinstabilities are coherent. In a plant situation, it has long been hypothesized that the mechanical impact of macroinstabilities on the tank internals, impeller shaft and impeller itself may cause significant damage. In the present study, this situation is confirmed in the case of a full-scale vessel, where failure of the bolts coupling the shaft with the motor was observed.

The spread of turbulence in a shear flow can be related to the phenomena of entrainment, that is the incorporation of irrotational fluid into the turbulent region. Translated into mixing, the turbulence generated by the impeller spreads throughout the tank and this mechanism is mostly due to the propagation of a whole range of eddies. By analogy with the fully developed turbulence in a pipe, in a mixing vessel the viscous forces and the large eddies are generated mostly in the proximity of the solid boundaries; close to the impeller blades or baffles. In order to investigate the response of macroinstabilities to changes in the Reynolds number (or changes in the ratio between viscous and inertial forces) the fluid viscosity was varied.

The extreme difficulty of detecting the macroinstabilities arises from the fact that with the LDV probe we cannot measure the velocities at two different spatial locations simultaneously. To eliminate this disadvantage a number of points (spatially located down stream of the path of the macroinstabilities) were measured with LDV. The spatial placement of the measurement grid coincides with the region (upstream of the baffle and close to the tank wall) where the 3-D wall jet was found (Bittorf and Kresta, 2001).

The combination of Lomb periodogram analysis (Chapter 1) with a supplementary statistical treatment was applied to all experimental data. The results for A310 and HE3 impellers were combined since no coherent frequency was found for either impeller. In the case of the 45° PBT ($D=T/2$ and $C/D=0.50$) a single coherent frequency (f_{MI}/N) was identified at both vessel scales, which also stayed constant when the Reynolds number was varied. These results will be extended in Chapter 3, where large eddy simulations (LES) are used to probe large-scale macroinstabilities in the resonant geometry.

2.1 LDV apparatus

In this study two different LDV systems were used to probe the frequency of the macroinstabilities. Both instruments detect the velocity of the seeding (fluid) particle traversing the measuring volume. The main components of a standard LDV system are laser, Bragg cell, transmitting optics, photodetector, signal processor and traverse mechanism. While both instruments are made up of similar components, significant differences in configuration warrant discussion. To place this discussion in context, the principle of LDV measurements is summarized below.

In laser Doppler velocimetry two beams of linearly polarized laser light are crossed to form a measuring volume. Because velocity is a vector quantity, it is necessary to measure not only its magnitude but also its direction. Hence, one beam is frequency shifted, creating a light-beating (moving) pattern of fringes in the measuring volume. The frequency of the scattered light will decrease if the particle is moving in the same direction as the moving fringes, and will increase if the particle is moving in the opposite direction. The frequency shift is done using the acoustic-optical modulator also known as a Bragg cell. If the frequency shift is chosen so that it exceeds the maximum expected velocity, then directional discrimination of all signals will be possible. In this study two different frequency shifts were used: 40MHz and 1 MHz.

The scattered light is collected in a photodetector where the modulated light intensity generates a frequency equal to the Doppler frequency caused by the velocity of the particle. Depending on the position of the photodetector there are two types of the LDV's; one operating in forward scatter mode and the other operating in backscatter mode. In this study small scale experiments were done with the Aerometrics forward scattering LDV system, while the large-scale experiments were done with a dual-color Dantec 55X LDV system, operating in backscatter mode. Schematics of these two arrangements are shown in Figures 2-1a and 2-1b.

The primary task of the signal processor is to extract the frequency information from the burst signal (Figure 2-2) generated by a particle passing through the measuring volume, and provide an analog or digital output proportional to the frequency of the signal. It should be noted that burst signals are usually noisy, may only have a few

cycles, have amplitudes varying within the burst, arrive at random times, have a peak amplitude which varies from one burst to the next, and can contain frequencies over 100 MHz. Numerous techniques have been used for processing the Doppler signal. For full descriptions of these the reader should consult the general references by Drain (1980) and by Durst et al. (1981).

2.1.1 Small scale experiments

The Aerometrics LDV is one-component system operating in forward scatter mode (Figure 2-1a). It uses a 300mW argon laser ($\lambda=514.5$ nm) with a beam separation of 0.0338m, and a focal length of 500mm, corresponding to a fringe spacing of $7.6\mu\text{m}$. Further details of the instrument configuration are given in Zhou and Kresta (1996). Details for optical parameters of the Aerometrics LDV system are given in Table 2-1. Two types of signal processors, a Doppler signal analyzer (DSA) and a real signal analyzer (RSA) were tested. Both of them operate in burst detection mode, and both were capable of accurately measuring velocity signals with a low signal to noise ratio (SNR). In the DSA every detected burst is “gated” meaning that the transit time is fixed. This incorporates some noise in the time record especially when both short bursts and long bursts are processed. This problem is compensated for in the RSA, which allows control of the number of samples per burst and centers the record time in the middle of the burst. A detailed discussion of the advantages and disadvantages of both signal processors can be found in Grgic (1998). Neither of these processors was able to recover the high frequency part of the turbulence spectrum. In Figures 2-3a and 2-3b, spectra obtained directly from a conventional LDV signal processor (van Maanen, 1999), and from constant temperature anemometry (CTA) (Wernerson, 1997) are compared. The slope of the LDV spectrum aliases up to 10^2 Hz, while the CTA spectrum extends with a clear $-5/3$ slope up to 10^3 Hz.

To reduce the noise contamination in the velocity signal, the shift frequency was reduced from the Aerometrics standard of 40MHz down to 1MHz. The change of the shift frequency neither improved the high frequency part of the spectrum nor affected the macroinstabilities and the statistics of the time series. Identical frequencies were

calculated from velocity time series measured at 1MHz and 40 MHz shift frequencies. The repeatability of the time series statistics (mean and RMS velocity) was verified at both frequency shifts. A traverse of the axial velocity for the 45° PBT ($D=T/2$, $C/D=0.5$) was measured 3mm below the impeller blade. In Figures 2-4a and 2-4b, mean and RMS velocities are compared with the previous LDV data by Zhou (1996). Despite the excellent agreement between the mean velocities some differences in RMS velocities are evident. This is mainly due to the increasing number of samples collected in the present experiments to 30,000 from the 10,000 used by Zhou.

For all experiments the analog signal was sampled at 2.5 MHz or 5 MHz. These frequencies were shown to be optimum by Grgic (1998) and to produce accurate results for the mean and RMS velocity profiles. The frequency of velocity measurements is also determined by the particle arrival rate, which varied from 1500Hz to 700Hz in this work. This variation reflects the distribution of the particles in the fluid, or the seeding density. In the impeller region, the data collection is faster than that in the top of the tank because the fluid velocity is higher and more fluid traverses the measuring volume per unit time. Although all velocity time series were taken over a fixed sampling time of 60s, the number of velocity determinations per scanned point varies substantially, from 60,000 to 100,000, due to the different particle arrival rate in different parts of the tank. The percent of measurements validated was always higher than 90%.

An automatic traverse mechanism was used to position the tank in two directions: x and y. Positioning of the z direction and off-bottom clearance adjustments for the impeller were done manually. The accuracy of the horizontal x and y-traverses was $\pm 0.5\text{mm}$ while the vertical traverses was positioning within $\pm 1.0\text{mm}$.

The zero position for the x, y traverses was determined by moving the traverses from the tip of the impeller blade ($D=T/2$) to the tank wall. The procedure is complete whenever the reading of the traverse is identical to the physical location of the traverse. The zero position of the vertical traverse was found knowing the off-bottom clearance of the impeller. The off-bottom clearance was set by moving the impeller shaft to the bottom of the tank and marking this position as zero.

2.1.2 Large scale experiments

The velocity time series was obtained at the Lightnin-Mixer facility using a two-color Dantec 55X LDV system. An Argon Ion laser (2W) was operated in back scatter mode (Figure 2-1b) and the signal was transmitted via fiber optics (Weetman, 1981). This eliminates the need to re-align the receiving optics at each scanned point but the signal strength is weaker than in the forward scatter arrangement. One of the beams is frequency shifted using a Bragg cell at 40MHz. More information on the measuring volume dimensions is given in Table 2-1.

Next the signal coming from the photomultiplier was converted to a series of Doppler frequencies from which the time series of the velocity can be determined. The signal processor is operated in the burst (random) detection mode that ensures the highest possible temporal resolution. The data rate was adjusted carefully by adding polystyrene seeding particles with diameter of $2\mu\text{m}$. They are neutrally buoyant and they have good light scattering properties. The data rate depends on the seeding, focusing and position of the measuring volume inside the tank. The validation rate varied substantially but was always greater than 70%. The burst quality was monitored during the measurements with the oscilloscope. It was observed that the bursts had good visibility and low noise contamination. The data collection was automated allowing computer-controlled operation. The total number of collected samples per scanned point varies from 15,000 to 20,000, giving time records from 2 to 10min in length.

The third important part of the LDV system is the traverse mechanism. The laser head is attached to a 3D traverse, which allows positioning of the measuring volume with error $\pm 0.01\text{in}$. The zero position of the coordinate system was chosen to be in the center of the tank (x and y position) and at the bottom of the tank (z position). Prior to starting experiments two other issues which affect the exact position of the probe volume inside of the tank must be addressed. When the laser beams travel through different solid material or fluids the position of the intersection of the beams is distorted due to the changes of refractive index. To address this problem code was developed based on vector algebra (see Kresta and Wood 1993b). The code corrects the position of the traverse in outer coordinates to obtain the desired interception position of the measuring

volume inside the cylindrical tank. The code implements the Newton-Raphston numerical routine which finds the roots of the system of two non-linear equations. The procedure is iterative and requires an initial guess. For more details the reader should see Numerical Recipes in C++(Press et al., 1994), and Kresta and Wood (1993b).

Once the refractive index correction was done the center of the tank was located using a spatial zeroing cone on the shaft. The procedure was completed when the measuring volumes of the blue (for measuring the radial velocity component) and green (for measuring the axial velocity component) beams were both visible on the cone of the shaft. The procedure was repeated twice to ensure exact zeroing of both the x and y-axes.

The mixing tank can be described as a mechanical system, including the tank, impeller, fluid, shaft, and motor. Every mechanical system can be characterized by a natural (critical) frequency, N_{CRIT} . Because the shaft is subject to fluid forces in a dynamic environment, for practice the situation of more concern is where the resultant force on the shaft occurs at its natural frequency. If the impeller is run at the natural frequency of the system (impeller-fluid-shaft) one could expect a large amplification of the fluid forces and even breakage of the shaft. To avoid this condition, the natural frequency of the system was measured monitoring the mechanical loads on the shaft. This was done using a strain gage mounted between the shaft and the drive unit. The strain gage measures the percent elongation of the shaft which is proportional to the stress on the material for elastic materials. N_{CRIT} is important parameter for the large-scale tanks but not so important for the small laboratory scale. Examples of two spectrograms for a 45° PBT ($D=T/2$) and A310 ($D=0.35T$) are shown in Figures 2-5a and 2-5b.

2.2 Mixing tank geometries and fluids

2.2.1 Mixing tanks

Two mixing tank models are used for this work to allow study of the scale up: one with tank diameter $T=0.240\text{m}$ and the other with diameter $T=1.22\text{m}$ (4.0ft). The small scale tank was built for the University of Alberta mixing laboratory while the large scale tank was provided by Lightnin-Mixers, Rochester USA. Both tanks are cylindrical and

are equipped with four vertical rectangular baffles of width, $W=T/10$. The baffles are equally spaced around the periphery of the tank at a small distance from the wall. The liquid level, H , in the tanks was kept equal to the tank diameter, $H=T$. Both cylindrical tanks were placed in square tanks filled with the same fluid to minimize optical distortion.

To prevent air entrainment and surface vortexing, a lid was placed on the top of the small-scale tank, which was covered with an additional 5 cm of fluid to seal the tank surface. The large-scale tank was not covered with a lid and therefore special attention was required to prevent air entrainment. Unavoidably, in some runs, there was a small number of gas bubbles in the upper part of the tank due to air entrainment. The lid is known to have no effect on mean velocity (Ljungqvist and Rasmuson, 1998).

2.2.2 Impellers and fluids

The study of macroinstabilities generated by three axial impellers was undertaken: a 45° pitched blade turbine, known as a 45° PBT, Lightnin fluidfoil impeller (A310) and high efficiency impeller provided by Chemineer (HE3) as shown in Figure 2-6. The detailed geometric specifications of the large and small scale 45° PBT are given in Table 2-2. The A310 and HE3 were as supplied by Lightnin and Chemineer respectively.

The experimental design covers variation of two important geometrical variables for the mixing tanks:

- i. impeller diameter- for the 45° PBT $D=T/2$ and $T/4$, for the HE3 $D=T/3$ and $T/4$, and for the A310 $D=0.58T$ and $0.35T$
- ii. off-bottom clearance ratio- $C/D=0.33, 0.50, 0.67, 1.00$.

General observations of the flow field in mixing tanks, discussed by Chapple and Kresta, (1994), show that the stability of the flow direction depends on a complex interaction between the impeller diameter and off-bottom clearance. A bigger impeller diameter is more likely to interact with surrounding baffles, generating a flow subject to some type of instability. Kresta (1991) observed that the characteristics of the 45° PBT flowfield depend strongly on the off-bottom clearance. Instead of a single circulation loop which

extends over the whole tank for all geometries, the primary circulation loop reached the bottom of the tank only for a $C=T/3$ clearance and was accompanied by a secondary circulation loop when the clearance was increased to $C=T/2$. This motivates us to examine two impeller diameters and to cover a range of off-bottom clearances. All small and large-scale geometries examined are summarized in Table 2-3.

Usually, the complex hydrodynamics of the mixing tank is characterized using a few dimensionless numbers. The impeller Reynolds number (Re) is one of the oldest and most commonly used among them. It gives the ratio between the inertial and viscous forces. For the mixing tanks the Reynolds number is defined as:

$$Re = \frac{ND^2}{\nu} = f(N, D, \nu) \quad (2.1)$$

N =rotational speed of the impeller (rps)

D =diameter of the impeller, (m)

ν =kinematic viscosity of the fluid (m^2/s)

The value of the impeller Reynolds number characterizes the flow regime in the mixing tank—turbulent, transitional or laminar. The impeller drives the flow and therefore the impeller diameter and the tip speed, V_{tip} are used as characteristic length and velocity scales. It is accepted that the limit of the fully turbulent regime for the mixing tank is at a Reynolds number equal to 20,000. Below $Re=20,000$ the flow is transitional.

According to Equation 2.1, there are two possible ways of changing the Reynolds number for a fixed impeller diameter, D , either by changing the rotational speed of the impeller N or by changing the viscosity of the fluid. Both approaches were explored in both small and large-scale experiments. This provides an opportunity to study how sensitive macroinstabilities are to changes in the ratio between viscous and inertial forces. This is very important for the flow in the bulk of the tank where the turbulence is suppressed and the macroinstability prevails. Three Newtonian fluids were tested: water, bayol and different water solutions of triethylene glycol (TEG). In Table 2-4 a summary of the fluid viscosities is given.

2.2.3 Flow visualization

Even though the flow visualization is quite an old technique it gives a representative picture of the flow field and it is extremely helpful when attacking a new problem. It is a non-intrusive method showing the flow field in a whole 2-D plane at one time and it is very easy and cheap to perform. For a better understanding of the complex hydrodynamics in the mixing tank this qualitative picture is very useful. Prior to starting the LDV experiments an extensive flow visualization study was performed. The flow patterns for three axial impellers were carefully examined in a small-scale tank ($T=0.240\text{m}$) using a filament light source to produce a sheet with thickness of 2-4mm. In order to track the flow field a small amount of $160\mu\text{m}$ polystyrene particles were added. They scatter the light while passing through the illuminated plane, so the observer can see their path (Kresta, 1991). The light sheet was oriented vertically. All impellers were set to rotate in the clockwise direction. Two different axial planes were watched for a long period of time-10 to 20 minutes. The first plane was located upstream of the baffle, where the three-dimensional wall jet is formed (Bittorf and Kresta, 2000). The second plane was chosen to lie in the mid-baffle plane.

The main characteristics of the flow produced by a 45° PBT ($D=T/2$) matched those described in the literature (Tatterson and Brodkey, 1980, Kresta and Wood, 1993b). The impeller discharge jets are formed and all four jets may interact with each other in a complex manner when impinging on the bottom of the tank. This creates a violent upward flow along the tank wall. It was observed that the jet in a single plane is flapping, changing its angle from 90° (impingement on the bottom) to almost 180° (impingement on the wall of the tank). Regularly, every four to five flaps, a large vortex is torn off the bottom, quickly escaping up, entraining the surrounding fluid and creating a fountain observed on the free surface of the large scale tank. The same phenomenon called "surface swelling", has been observed by Bruha and Fort, 1993 (Figure 2-7). They report that the regions on the free surface where the vortex disintegrates are always upstream of the baffles. These are the same four regions where the 3-D wall jets develop.

Based on the flow visualization analysis, the experimental grid was located in the region where the wall jet develops and the surface welling originates. The total number

of grid points scanned with LDV was 60 for the small-scale experiments and 150 for the large scale. The node distribution for the small-scale tank was 6 nodes in the radial direction (measured every 5mm from $y=80$ to $y=110$ mm) at 10 axial positions ($z/T=0.40, 0.50, 0.55, 0.60, 0.65, 0.70, 0.75, 0.80$ and 0.90) (see Figure 2-8) whereas for the large scale there are 30 nodes in the radial direction at 5 axial positions ($z/T=0.50, 0.60, 0.70, 0.75, 0.80$). Because of the large diameter, the distribution of the radial points at different heights was different. Table 2-5 summarizes all radial and vertical positions examined for both small and large scale tanks.

2.3 Experimental errors

An experimentally measured quantity usually deviates from its true value by an amount called the experimental, or measurement error. Because the true value is a quantity which is generally unknown the magnitude of the error can only be estimated. Here the importance of the different sources of uncertainty will be discussed for both measured quantities: fluid viscosity and velocity time series.

There are two types of errors: one that is always the same when the quantity is measured, known also as systematic error, and the other that is randomly distributed. While averaging the quantity over a number of measurements can minimize the random errors, the reduction of systematic errors can be done only by eliminating of the source of error.

2.3.1 Viscosity measurement

In this study, the Reynolds number is calculated according to Equation 2.1 and the error in it depends on the individual errors in D , N and ν . The principle of propagation of variances can be used to derive an expression for the variance of Reynolds number as a function of variances of these three variables:

$$\sigma_{Re}^2 = \left(\frac{\partial f}{\partial N} \right)^2 \sigma_N^2 + \left(\frac{\partial f}{\partial D} \right)^2 \sigma_D^2 + \left(\frac{\partial f}{\partial \nu} \right)^2 \sigma_\nu^2 \quad (2.2)$$

If it is assumed that the variables are symmetrically distributed random variables which are statistically independent, substituting the Equation 2.1 into Equation 2.2 gives:

$$\frac{\sigma_{Re}}{Re} = \sqrt{\frac{\sigma_N^2}{N^2} + \frac{2\sigma_D^2}{D^2} + \frac{\sigma_v^2}{v^2}} \quad (2.3)$$

σ_{Re}/Re is the relative error of Reynolds number. According to Equation 2.3 the Reynolds number estimation will be most sensitive to incorrect measurements of the swept impeller diameter. In our case the small impeller diameter is determined with an error of 0.1mm (or relative error of 0.08%) while the large-scale impeller diameter is determined with an error of 0.05in (0.21%). The relative error of the rotational speed N is specified by the manufacturer and it is less than 0.1%.

The viscosity was measured using capillary Cannon-Fenske viscometers at room temperature 22°C (average specific density equal to 1.00) for the small scale experiments. Resulting viscosities are given in Figure 2-9. For large-scale experiments the viscosity of the TEG fluid was monitored three times per day and the Reynolds number was calculated based on the average viscosity value during the day. The measured viscosity vs. temperature variations for two mixtures of TEG are given in Figure 2-10. The specific gravity and viscosity temperature dependencies for different solutions of TEG given by Shell are shown in Figures 2-11 and 2-12. The agreement with the data in Figure 2-10 is very good.

During the day, the kinematic viscosity changes by no more than 1cS due to an increase in the temperature; thus the relative error in viscosity for large-scale experiments does not exceed 10%. Combining all errors this results in a relative error of 10% for the experimentally determined Reynolds number.

2.3.2 LDV measurements

The measurement accuracy of the LDV depends on the signal quality or signal to noise ratio (SNR) of the signal burst. While the signal processor used to extract the frequency of the burst can have an influence, a higher SNR of the input signal invariably leads to more accurate flow information. According to Adrian and Early (1975), the SNR depends on many factors such as laser power, efficiency of the photodetector, optical

alignment and bandwidth of the Doppler signal. The proper choice of all these parameters will ensure higher SNR or good velocity measurements. The vendor predetermines some of these factors; however, the SNR can be improved if the following are done:

- i. the beams are properly collimated and parallel to the optical axes,
- ii. a particle size which follows the fluid is selected.
- iii. refraction due to passage of the beams through materials with different refraction indexes is minimized.

The concentration of the tracer particles is not only of importance for the noise level in the Doppler signal but also for the data-rate. It is important that one determine experimentally the optimum particle concentration by monitoring the data rate and the validation percentage. The later factors are general for all LDV systems and should be considered for velocity measurements at any types of flow.

The other source of uncertainty in the measurement of the Doppler frequency that can directly affect the estimated turbulent quantities (van Maanen, 1999) is arrival time estimation noise. Usually the arrival time of the Doppler signal is defined as the time at which the particle is in the center of the measurement volume. Or, to be more precise, when the distance that the particle has traveled through the measuring volume is equal to the distance it still has to travel through it. Noise is incorporated if the particle does not move through the exact center. This noise introduces an uncertainty in the record time. This error can be reduced either by using short transit times or by minimizing the measurement volume.

The random error associated with fluctuations in the measured Doppler burst and the systematic error introduced by the correlation of the sampling frequency with the velocity of the particle, known as velocity bias, is important for calculating the mean and RMS velocity and does not affect the frequency content of the signal. The velocity bias arises from the fact that the number of particles passing through the measuring volume per unit time is higher at high velocity than at low velocity. In effect there is a correlation between the nature of the flow (velocity) and the sampling process. Here we will

concentrate only on the factors which are important for obtaining a correct estimate of the low frequency part of the spectrum. They are:

- i. length of the velocity record which depends on the sampling size/time (or data rate)
- ii. accurate positioning of the measuring volume
- iii. random sampling times, as discussed in Chapter 1.

The macroinstabilities were characterized by determining the low frequency content of the measured velocity time series. Based on the observations of Bruha et al (1993), we expect that the frequencies due to macroinstabilities, will be typically in the range of 0.1-20 Hz for a small-scale tank and one order of magnitude lower, 0.01-5 Hz, for a large-scale tank. Due to the time series finite length, it is possible to calculate the lowest frequency that can be detected. This frequency will sustain only one period and it is proportional to the inverse of the total measuring time. For example, if the total time of the velocity time series is 60s, then the lowest frequency which can be detected is 1/60 or 0.0167Hz. It is clear that in the small-scale tank, a 60s time record will be more than enough to capture many low period velocity oscillations due to macroinstabilities. A long velocity record is essential in order to capture many macroinstability oscillations.

Experimental results show that both the sampling size and the sampling time are critical to velocity measurements. It was reported by Zhou (1996) that the sample time must be long enough to cover at least 80 passages of the impeller blade in order to get a stable mean velocity reading. Calculations showed that for a small-scale tank with an impeller with 4 blades rotating at 400 rpm, the sampling time should be no less than 3 seconds (i.e. $3 \times 4 \times 400 / 60 = 80$ blade passages). If the sampling time is too short, the reproducibility of the mean velocity measurement is poor even with a sample size larger than 10,000 data points.

For all small-scale experiments the sampling time was set equal to 60s, which means that the number of samples varies in different z/T planes from 60,000 to 100,000 data. In the large-scale experiments the number of samples was fixed from 15,000 to 20,000 due to the limitations of the computer software. The length of the velocity records varies

from 2-12min. For both experiments this corresponds to a sampling time much longer than 100 rotations of the impeller and allows the capture of many macroinstability cycles, which occur on the order of once every 5 rotations of the impeller.

Positioning errors due to incorrectly finding the zero position of the measuring volume and incorrect optical alignment can also contribute to the errors in velocity measurements. In the small-scale experiments the traverse in the z-direction is positioned manually and therefore the accuracy of the axial positioning was $\pm 1.0\text{mm}$, while in the x and y directions the accuracy was $\pm 0.5\text{mm}$. The positioning error of the traverse for the large-scale experiments was $\pm 0.1\text{in}$ in x, y and z directions.

2.4 Results

The frequency spectra of the axial velocity time series were evaluated using the Lomb algorithm (Chapter 1). The Lomb spectrum in Figure 2-13 shows the presence of both the BPF (Blade Passage Frequency) and the macroinstabilities, but such spectra are typical only for locations close to the impeller. There is a clear separation in scales between the BPF and the observed low frequency, therefore the macroinstabilities should be related more to the mean flow unsteady fluctuations instead of turbulence. The BPF almost disappears from the spectrum by a radial position of $2r/D=1.33$ as shown in Figure 2-14.

Because of the different spatial locations of the examined points, a statistical histogram approach was used in order to evaluate the presence of a coherent (single) frequency. For all grid points examined in this work the macroinstabilities are the dominant frequency. Once the individual frequency spectrum was calculated for all 60 locations in the small-scale experiments and 120 locations in the large-scale experiments (Figure 2-8), histograms with the distribution of these frequencies at the baffle were constructed. Only the frequencies containing power higher than 75% of the maximum peak in an individual spectrum were included in the histograms. The choice of the 75% threshold eliminates the presence of any spurious frequencies such as the BPF (which are 20 times higher than the low frequencies) and ensures that only the low-period events

will be included. Because all time series have finite length, the lowest possible frequency was calculated in such a way that the total time interval can sustain at least 5 periods. All calculated frequencies lower than this limit were discarded. The mean and the standard deviation of the selected frequencies were also calculated. Every bin size was optimized starting with the calculated standard deviation value as a first guess. The bin size was minimized in such a way to include enough counts for statistics and to have enough resolution. For better comparison of the results the bin size for all impellers was equal to 0.05 Hz.

2.4.1 HE3 and A310

The results for the small-scale Chemineer HE3 impeller with diameter of $D=T/3$ at three different C/D ratios are shown in Figure 2-15. The histograms show no dominant frequency; on the contrary a broad band of low frequencies are evident. This impeller creates a very weak and unstable flow field in the vicinity of the examined baffle-wall region (Jaworski et al, 1996).

In Figure 2-16 the frequency histograms for the small-scale A310 are shown. The impeller diameter in this case is $D=0.58T$. The Reynolds number is $Re=6.5 \times 10^4$, so the flow field is fully turbulent. The frequency of the macroinstabilities is unstable, with dimensionless frequency, f_M/N ranging from 0.09 to 0.132. A single dominant frequency could not be identified. The maximum variability of the frequencies is observed in the case $C/D=0.33$. The flow pattern in this configuration is influenced by the proximity of the tank bottom to the impeller. This gives rise to a wide distribution of frequencies, as there is a feed back from the impinging flow at the bottom of the tank to the impeller discharge. No coherent frequency was evident for either of these axial impellers on small scale.

At the large scale, the frequency distribution results for the A310 with impeller diameter of $D=0.35T$ and $C/D=1.0$ also showed no dominant or coherent frequency. A broad band of very low frequencies is evident, as shown in Figure 2-17. If any macroinstabilities are generated by this impeller they have a very long period, of the order of *few hundred* impeller rotations. The long period of A310 macroinstabilities and

their relatively small amplitude requires very long velocity time records. The records must be extended up to 20-40min on the large scale in order to get repeatable results.

2.4.2 PBT

In the case of a small scale PBT with $D=T/2$ and $Re=48000$, the distribution of frequencies (Figure 2-18) shows a distinctive peak at dimensionless frequency of $f_{MI}/N=0.186$. This frequency remains dominant when the C/D ratios are varied. For C/D ratios 0.33 and 0.67, the histograms show the presence of additional frequencies $f^*/N=0.078$ and $f^{**}/N=0.228$ and some scattered minor frequencies. The resonant geometry for the macroinstabilities is at $D=T/2$, $C/D=0.5$ as shown in Figure 2-18b. At this off bottom clearance, the dominant frequency is very coherent.

In Figure 2-19, the frequency histograms obtained from a large-scale experiments at the same off-bottom clearances $C/D=0.33$, 0.50 and 0.67, are shown. A single coherent low frequency of $f_{MI}=0.186$ Hz which scales with the rotational speed of impeller was again detected. The magnitude of the frequency is always 18.6% of the rotational speed for Reynolds numbers greater than 20,000. This agrees exactly with the results obtained in the small-scale tank. In contrast with the small-scale experiments the f_{MI} stays coherent not only for the C/D ratio of 0.50 but also for the higher C/D ratio. We hypothesize that the stabilization of the frequency may be due to the absence of the lid on the top of the large-scale tank. Ljungqvist and Rasmuson (1998) observed no difference in the mean velocities on removal of the lid.

Once the dominant macroinstability frequency and resonant geometry for both scales was determined, the experiments were extended by varying the fluid viscosity. All working fluids were Newtonian, with viscosities ν , ranging from 1×10^{-6} m²/s to 23×10^{-6} m²/s (see Table 2-4). The scaling of the dimensionless macroinstability frequency, f_{MI}/N , with Reynolds number is shown in Figure 2-20. For $Re > 2 \times 10^4$ the dimensionless frequency is constant at 0.186.

In Figure 2-21 the distribution of frequencies for the large-scale experiments in the resonant configuration ($D=T/2$, $C/D=0.50$) is shown at different axial heights in the tank

($z/T=0.60, 0.70$ and 0.90). At every grid node only the dominant (maximum) frequency is denoted. At the lower axial location (Figure 2-21c) f_{MI} is dominant at all measured points. At the higher axial locations $z/T=0.70$ and 0.90 zones of intermittency are formed. They are characterized by frequencies either higher or lower than f_{MI} . Spatially, those regions are formed close to the baffle and in the middle (central) part of the tank. This indicates the presence of a high degree of randomness due to a breakdown of the flow to small-size turbulent vortex motions. At the top of the tank ($z/T=0.90$) a second frequency is observed with a dimensionless magnitude of approximately 0.06 which is close to that measured by Bruha and Fort (1993) in their “surface swelling” experiments. At $z/T=0.90$ the f_{MI} is detected in a small radial region from $2r/D=1.2$ to 1.7 forming a small circle with diameter of $0.25T$. This coincides with the spot where the vortex disintegration on the top of the fluid surface takes place.

The placement of the macroinstability and intermittency zones is important if one wants to assess where in the reactor to put a feed stream in order to achieve a fast reaction. Certainly, if the feed pipe is placed at the top of the tank or in the baffle regions where the macroinstability are dominant the feed stream is more likely to oscillate, as has been reported by Houcine et al., (1999). Houcine et al., (1999) found three states of the feedstream which they characterized as no intermittency (the feed stream is always vertical), slight intermittency (chaotic movement of the feedstream jet) and effective intermittency with a period of 1-2s. They concluded that to avoid formation of unwanted byproducts, the feed stream has to be placed as close as possible to the impeller stream, where the flow is turbulent and the reactants will be in contact immediately. The local conditions of the flow field and more importantly the presence of macroinstability have to be considered to avoid irregularities in the concentration field.

Macroinstabilities were also recorded in a full-scale square tank with diameter $T=16.0\text{ft}$. In this plant scale, a repeated breaking of the bolts which couple the shaft to the gearbox was encountered. It was confirmed that the low frequency vibrations associated with the bolt and shaft failure were not related to mechanical issues in the motor or gearbox. In this tank (impeller diameter $D=T/2$, and $C/D=0.63$) the impeller rotational speed was 45rpm. The frequency of the recorded oscillations at the failure location was 5 to 6 oscillations per minute, corresponding to a dimensionless frequency

of $f^*/N=0.111$. This frequency is very close to the second peak in the histogram for a small-scale experiments in round tank with the same impeller diameter and off bottom clearance (Figure 2-18c).

Switching the impeller diameter to a small diameter ($D=T/3$ and $C/D=0.50$) essentially eliminates the dominant frequency as shown in Figure 2-22. The variability of the frequencies remains the same with increase of the Reynolds number. In this case the impeller discharge stream either impinges on the bottom of the tank or decays significantly before reaching the tank wall. The maximum frequencies are very low and not distinct as in the case of the large impeller diameter. These results show that coherent macroinstabilities are extremely sensitive to impeller diameter. Most probably the macroinstabilities become stabilized whenever the interaction between the impeller and the baffles is strong.

All results confirm that the macroinstabilities are an important characteristic of the unsteady flow field generated by a 45° PBT and should be taken into account. The same macroinstabilities persist in the flow not only in the small-scale tank but also in pilot scale vessels. In plant situations, the presence of macroinstability may result in amplified oscillations, which can cause a mechanical failure when applied to the shaft and impeller.

2.5 Conclusions

LDV time series of axial velocities upstream of the baffle were successfully analyzed using the Lomb algorithm, an alternative to the FFT for the case of unevenly sampled data. The Lomb algorithm was able to correctly capture the dominant frequency in the flow. The observed dominant frequency is 20 times lower than the blade passage frequency and it is associated with the presence of large macroinstabilities.

Statistical analysis of the frequencies at 60 small-scale and 150 large-scale grid positions gives quantitative information about the dominant frequencies of the macroinstability in the stirred tank. For the case of a small scale 45° PBT with diameter $D=T/2$ and four baffles a single coherent frequency of the macroinstability of $f_{MI}/N=0.186$ was observed. This frequency remains dominant when the off-bottom

clearance (C/D) is changed, but two additional frequencies appear ($f^*/N=0.078$ and $f^{**}/N=0.228$), and there is a distribution of minor frequencies around the dominant peaks. At the resonant geometry the frequency of the macroinstability scales linearly with the rotational speed of the impeller, N , for Reynolds numbers greater than 20,000. It has been shown that for the resonant geometry ($D=T/2$, $C/D=0.50$) the same f_{MI} exists in a large-scale tank with diameter 1.22m (4.0ft). The frequency recovered from the large scale LDV time series has a dimensionless magnitude of $f_{MI}/N=0.186$ which is exactly the same with those obtained from the small-scale. In contrast to the small-scale experiments this frequency remains coherent for C/D ratios of 0.50, 0.67 and 1.0. We hypothesize that the stabilization of the frequency may be influenced by the absence of the lid on the top of the large-scale tank. Finally full-scale data is provided for a large plant scale vessel, where a frequency matching that of the observed macroinstability resulted in repeated mechanical failures associated with the shaft coupling and the shaft itself.

The frequency analysis for the small-scale PBT (with small impeller diameter $D=T/3$), HE3, A310 and large scale A310 impeller did not show the presence of any coherent frequency. These impellers may produce a macroinstability with a very low frequency and more experimental efforts are necessary in order to properly detect this instability.

2.6 Nomenclature

C=	impeller off bottom clearance (m)
D=	impeller diameter (m)
f_{MI} =	frequency of macroinstabilities, Hz
f'	multiples of the macroinstability frequency, Hz
f''	triples of the macroinstability frequency, Hz
L=	blade length
N=	impeller rotational speed (rpm or s^{-1})
N_{CRIT}	critical impeller rotational speed (rpm or s^{-1})
Re=	impeller Reynolds number $\frac{ND^2}{\nu}$
T=	tank diameter, (m)
W=	baffle width, (m)

Greek

λ =	wave length , (nm)
μ =	absolute viscosity, (cP)
ν =	kinematic viscosity, (m^2/s , or cS)
ρ =	fluid density, (kg/m^3)
σ_{Re} =	variance of the Reynolds number
σ_{ν} =	variance of the viscosity
σ_N =	variance of the impeller rotational speed.

Abbreviations

A310=	three bladed aerofoil impeller by Lightning'
BPF=	blade passage frequency
DSA=	Doppler signal analyzer
HE3=	three bladed high efficiency turbine by Chemineer
LDV=	laser Doppler velocimeter
PBT=	four bladed, 45° pitched blade turbine
RSA=	real signal analyzer
SNR=	signal to noise ratio

2.7 References

1. Adrian R.J. and Early W.L., 1975, *Evaluation of laser Doppler velocimeter performance using Mie scattering theory*, Proceedings of the Minnesota Symposium on Laser Anemometry, University of Minnesota pp.429-454.
2. Bittorf K, and S.M. Kresta, 2001, *Three-dimensional wall jets: axial flow in a stirred tank*, AIChE Journal, **47** (6), 1277-1284.
3. Bittorf, K., 2000 *The application of wall jets in stirred tanks with solids distribution*, PhD thesis (University of Alberta, Canada).
4. Bruha, O., I. Fort, and P. Smolka, 1993, *Large scale unsteady phenomenon in a mixing vessel*, Acta Polytechnica, Czech Tech. Univ. Prague, **27** 33.
5. Chapple D. and S. M. Kresta, 1994, *The effect of geometry on the stability of flow patterns in stirred tanks*, Chem. Eng. Sci., **49**(21), 3651-3660.
6. Drain L. E., 1980, **The Laser Doppler technique**. John Wiley and Sons, Toronto.
7. Durst F., A. Melling and H. J. Whitelaw, 1981, **Principles and practice of laser Doppler anemometry**, second edition, academic Press Inc., New York.
8. Hans Rudi Eduard van Maanen, 1999, Retrieval of turbulence and turbulence properties from randomly sampled Laser-Doppler anemometry data with noise, PhD thesis. Amsterdam. The Netherlands
9. Houcine, I., E. Plasari, R. David and J. Villermaux, 1999, *Feedstream jet intermittency phenomena in continuous stirred tank reactor*, Chem. Eng. J., **72**, 19-30
10. Gaster M. and J. B. Roberts, 1977, *The spectral analysis of randomly sampled records by direct transform*, Proc. R. Soc. London A, **354**, 27-58.
11. Grant H.L., 1958, *The large eddies of turbulent motion*, JFM, **4**, 149-190.
12. Grgic B., 1998, *Influence of the impeller and tank geometry on low frequency phenomena and flow stability*, MSc thesis (University of Alberta, Canada).
13. Jaworski Z, A.W. Neinow and K.N. Dyster, 1996, *An LDA study of the flow field in a baffled vessel agitated by an axial down-pumping hydrofoil impeller*. Can. J. Chem. Eng. **74**, 3-15.
14. Kresta S.M., 1991, *Characterization and prediction of the turbulent flow in stirred tanks*, PhD thesis, MacMaster University, Hamilton, Canada.

15. Kresta, S.M. and P.E. Wood, 1993, *The Mean Flow Field Produced by a 45° Pitched Blade Turbine: Changes in the Circulation Pattern due to Off-bottom Clearance*, Can. J. Chem. Eng. **71**, 42-53.
16. Ljungqvist M, A. Rasmuson, 1998, *A comparison of the hydrodynamics of open and closed vessels*, Chem. Eng. Comm. **165**, 123-150.
17. Old Shell Chemical –online library
http://plaza.powersurfr.com/vesselin/vesselina_web/Vesselina_old.htm
18. Press, W.H., B.P. Flannery, S.A. Teukolsky, and W.T. Vetterling, 1989, **Numerical recipes, The art of scientific computing**, Cambridge University Press, New York.
19. Roshko A., 1976, *Structure of turbulent shear flows: A new look*, AIAA J., **14**, 1349-1357.
20. Tatterson and Brodkey, 1980, *Stereoscopic visualization of the flows for pitched blade turbines*, Chem. Eng. Sci. **35**, 1369-1375.
21. Weetman, R.J., and R.N. Salzman, 1981 *Impact of side flow on mixing impeller*, Chem Eng. Progress, June, 71-75.
22. Wernerson E. S., 1997, *Some fluid characteristics in the scale-up of Rushton turbine-agitated tanks*, PhD thesis, Lund University, Sweden.
23. Zhou, G. and S.M. Kresta, 1996, *Impact of the tank geometry on the maximum turbulence energy dissipation rate for impellers*, AIChE Journal **42**, 2476-2490.
24. Zhou, G., 1996, *Characteristics of turbulence energy dissipation and liquid-liquid dispersions in an agitated tanks*, Ph.D. thesis, University of Alberta, Edmonton, Alberta.

Table 2-1. Parameters of the two LDV systems used in this work.

	Dantec 55X LDV	Aerometrics LDV
Focal length, mm	600	500
Beam separation before expansion, mm	38	16.9
Beam waist before expansion, mm	2.20	-
Expansion factor E	1.98	2
Beam separation after expansion, ED mm	75.2	33.8
Beam waist after expansion, mm	4.36	0.140
Beam intersection angle, rad	0.125 or 7.1620°	0.067 or 3.87°
Diameter of focused laser beam, μm	88	1170
Measuring volume diameter, μm	88	1170
Measuring volume length, μm	1.40	82
Fringe separation, μm	4	7.6
Fringes, N	22	18

Table 2-2. Dimensions of the PBT impellers used in the small and large-scale experiments.

	Diameter, m	Blade width, W/D	Blade length, L/D	Hub diameter, d_h/D	Hub height, h/D
Small scale	0.120	0.20	0.44	0.13	0.11
Large scale	0.609	0.20	0.44	0.13	0.11

Table 2-3. Experimental configurations studied.

	Small scale experiments		Large scale experiments	
Impeller type	Impeller diameter, D	C/D ratio	Impeller diameter, D	C/D ratio
45° PBT	T/2	0.33, 0.50, 0.67	T/2	0.33, 0.50, 0.67
	T/3	0.50	-	-
A310	0.58T	0.33, 0.50, 0.67	-	-
	0.35T	0.50, 1.0	0.35T	1.0
HE3	T/3	0.40, 0.80, 1.0	-	-
	T/4	0.50, 1.0	-	-

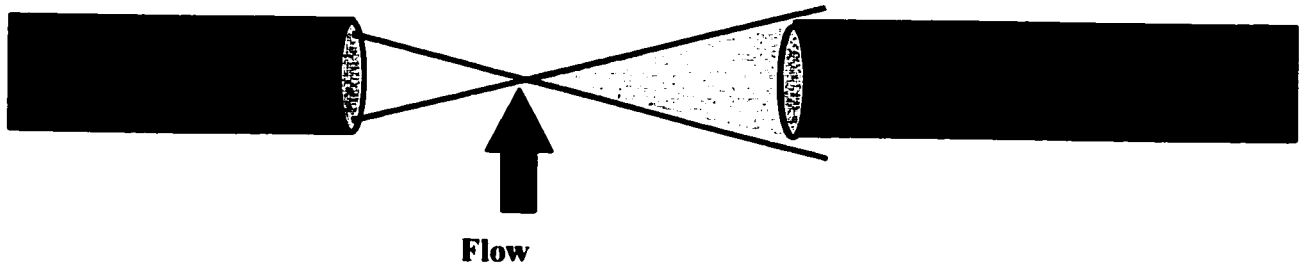
Table 2-4. Range of viscosities covered by the experiments.

	Small scale experiments			Large scale experiments		
Impeller type	Impeller diameter, D	Fluids	Kinematic viscosity, cS	Impeller diameter, D	Fluids	Kinematic viscosity, cS
45° PBT	T/2	Water	1.0	T/2	Water	1.0
		Bayol	3.0		TEG-1	6.5
		TEG-1	9.0		TEG-2	8.9
		TEG-2	23.0		TEG-3	17.7

Table 2-5. Summary of the radial and vertical positions of measurements for both small and large scale tanks.

Small scale experiments			Large scale experiments		
Vertical traverses, z/T	Radial positions, mm	Step, mm	Vertical traverses, z/T	Radial positions, in	Step, in
0.40	80-110	5	-	-	-
0.50	80-110	5	0.50	12-23	0.40
0.55	80-110	5	-	-	-
0.60	80-110	5	0.60	12-23	0.40
0.65	80-110	5	-	-	-
0.70	80-110	5	0.70	8-23.125	0.50
0.75	80-110	5	0.75	8-23.125	0.50
0.80	80-110	5	0.80	6-23.025	0.60
0.90	80-110	5	-	-	-

a)



b)

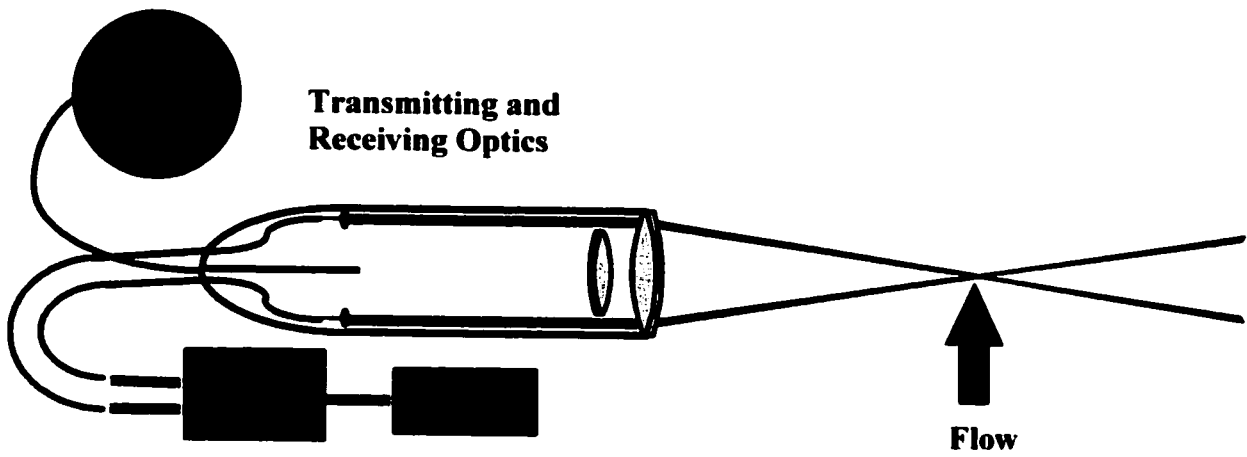
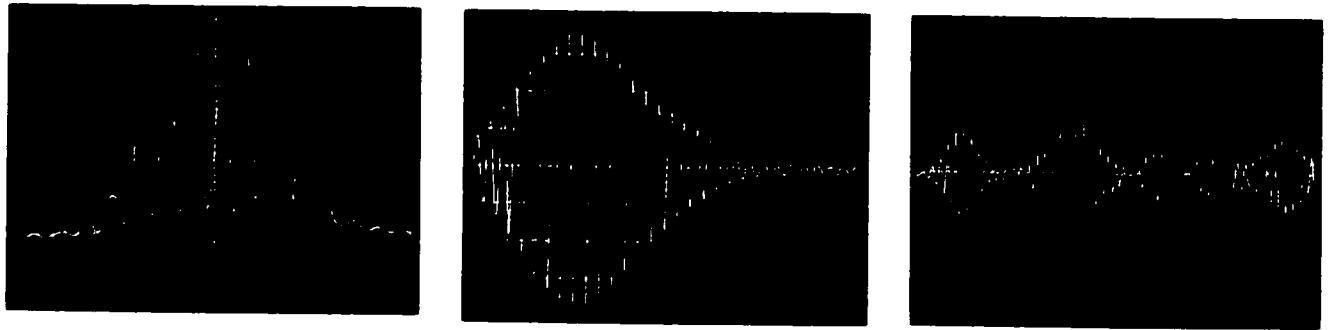


Figure 2-1. Schematics of the a) forward scattering LDV system and b) backscattering LDV system.



a) **b)** **c)**

Figure 2-2. Signal components of Doppler burst showing: a) Total signal b) High-pass filtering the modulated light intensity results in an oscillating signal. The frequency corresponds to the velocity of the tracer particles. c) Real sequence of Doppler bursts with some noise. Data are taken from Dantec Dynamics.

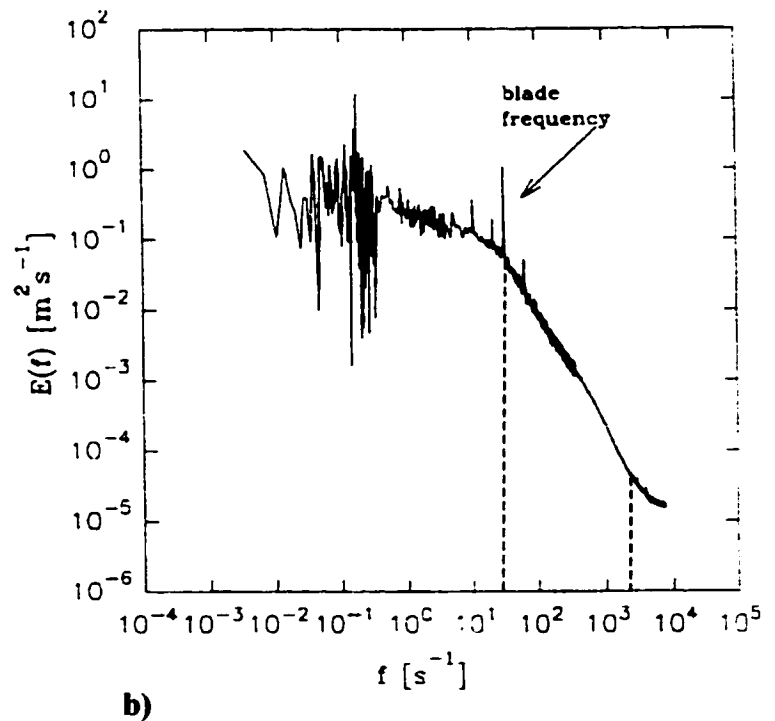
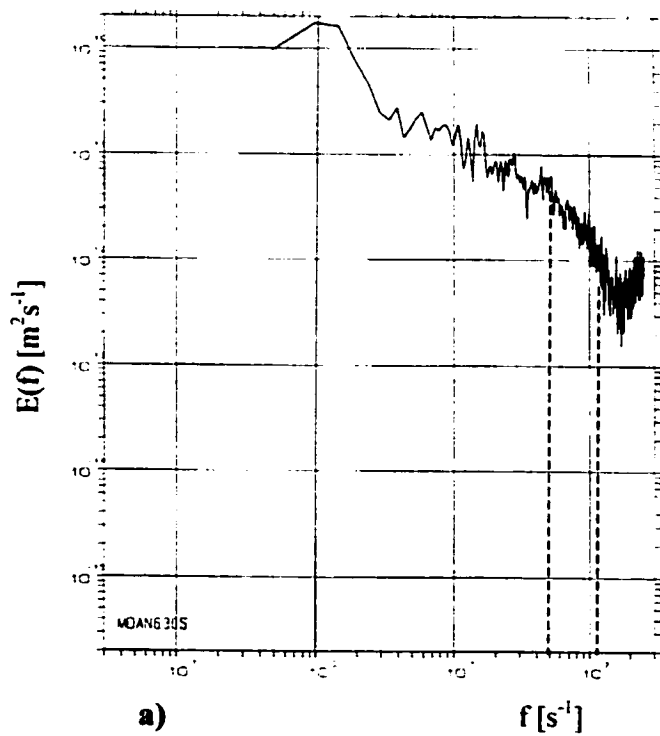
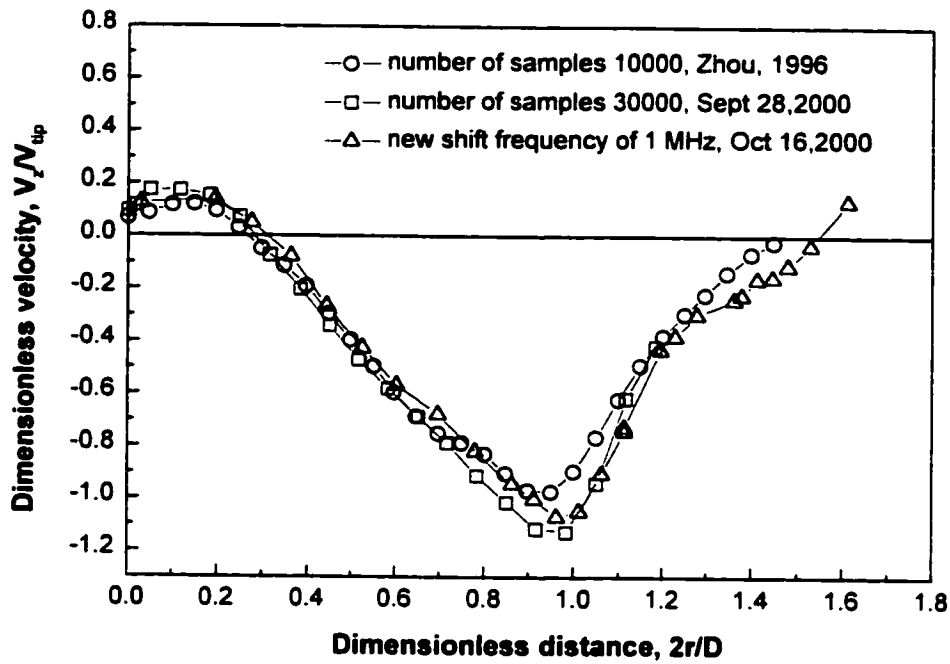


Figure 2-3. Examples of the frequency spectra obtained from a) LDV signal processor by van Maanen, 1999 and b) constant temperature anemometry (CTA) technique by Wernerson, 1997.

a)



b)

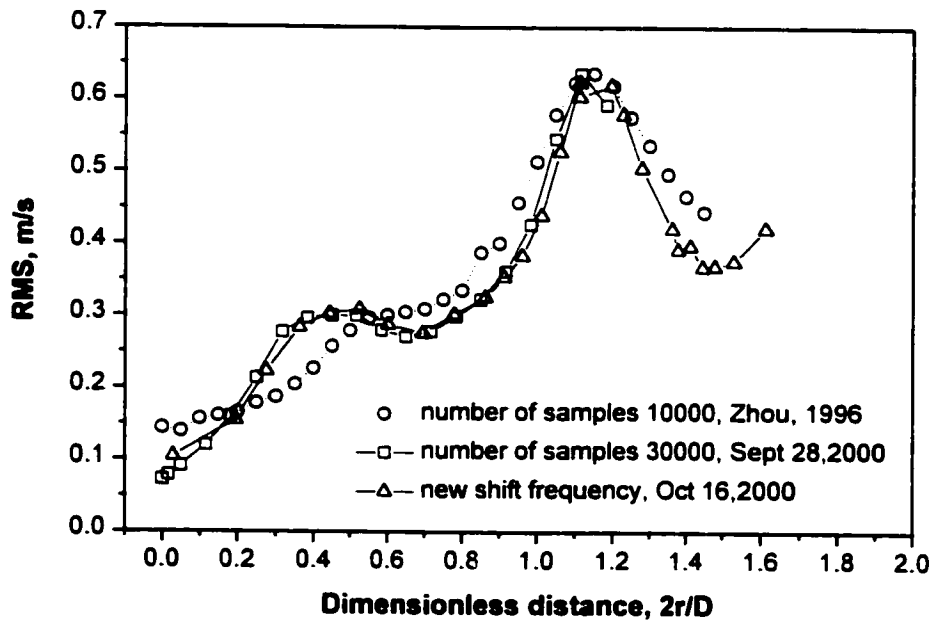
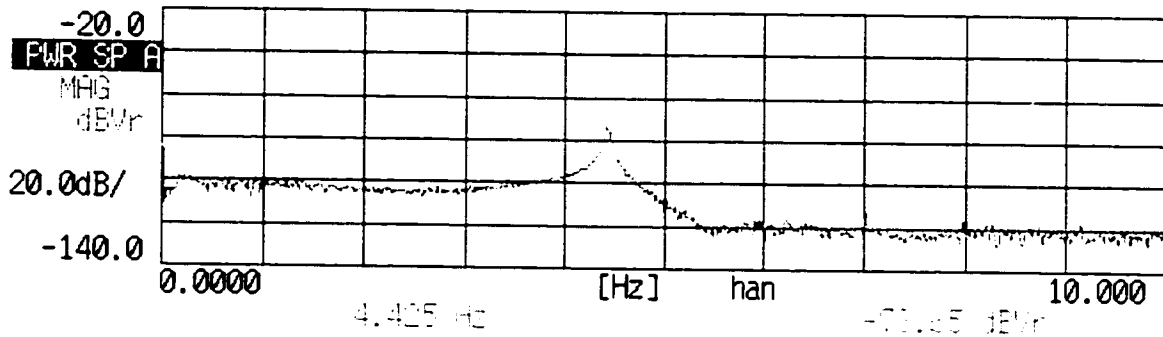


Figure 2-4. The mean and the RMS axial velocity profiles across the lower edge of the 45° PBT for two different shift frequencies: 40 MHz and 1 MHz. The effect of the number of samples is also shown.

a)

10.0 Hz A: AC/100mVr B: AC/316mVr



b)

10.0 Hz A: AC/100mVr B: AC/316mVr

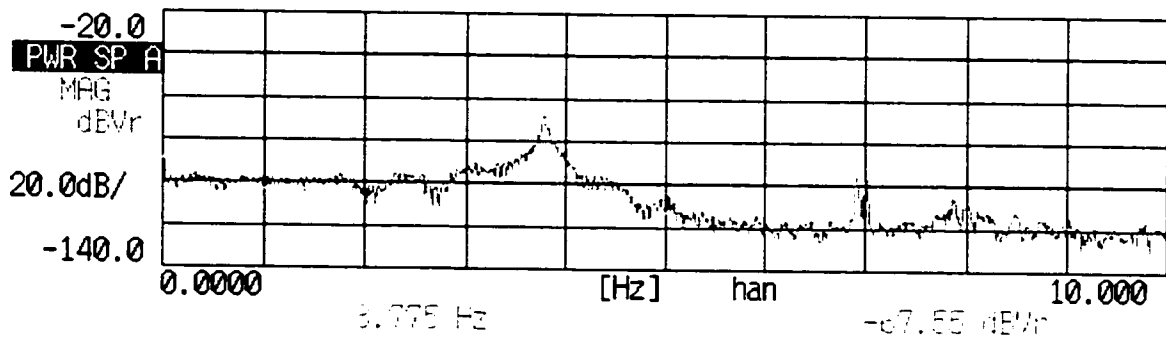
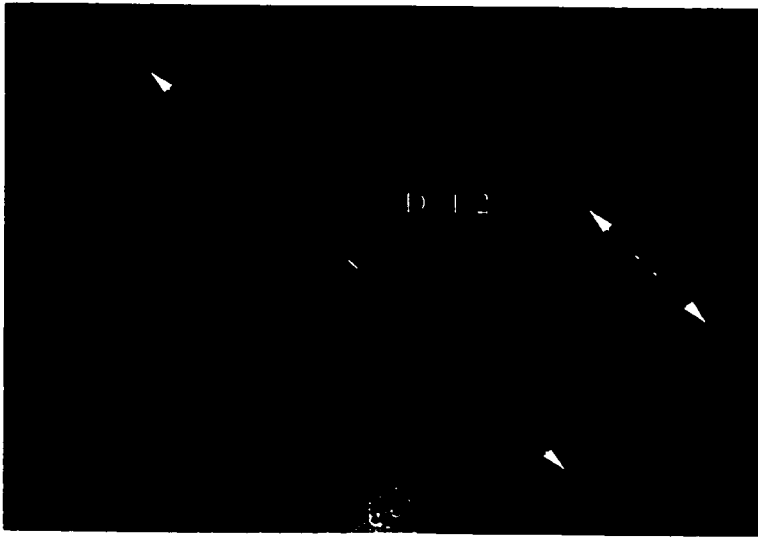
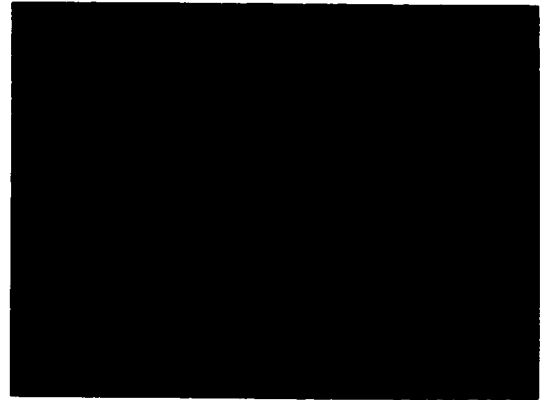


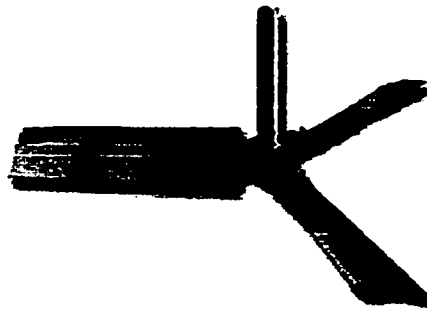
Figure 2-5. Natural frequency of the impeller-shaft system a) 45° PBT ($D=T/2$, $C/D=0.50$). Natural frequency of 3.775Hz. b) A310 $D=0.36T$ natural frequency of 4.425Hz.



45° PBT



A310



HE3

Figure 2-6. Impellers used in this work: 45° PBT impellers, $D=T/2$, small and large scale, fluidfoil A310 (by Lightnin) and high efficiency impeller by Chemineer (HE3-axial flow).

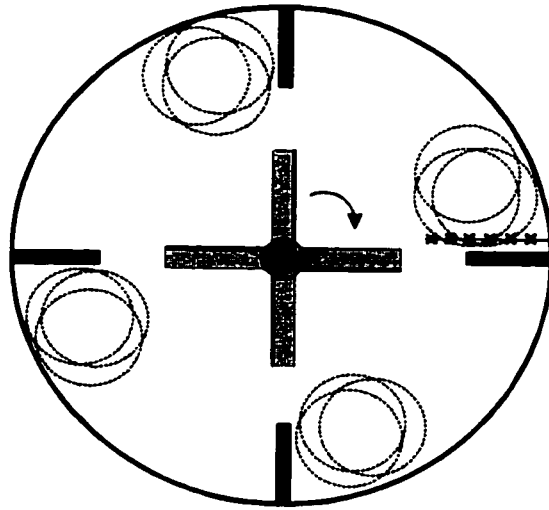


Figure 2-7. Top view of the regions of vortex disintegration on the free surface of the mixing tank (after Fort and Bruha, 1993).

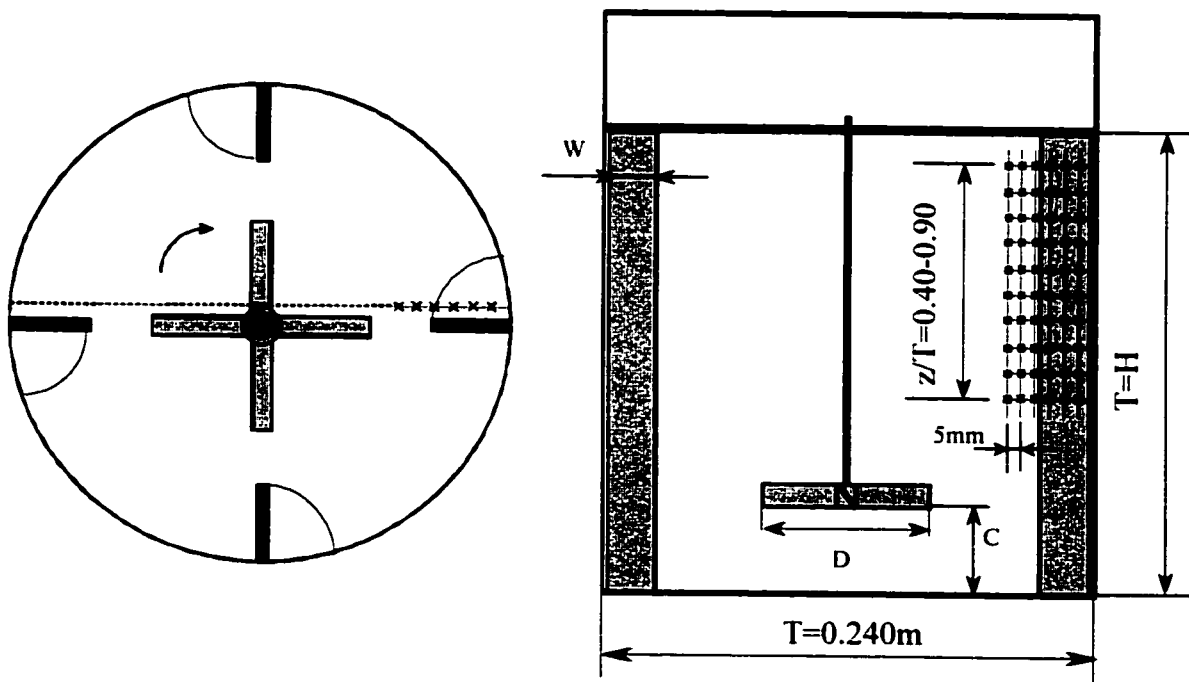


Figure 2-8. Schematic of the small-scale mixing tank showing the LDV measurement grid.

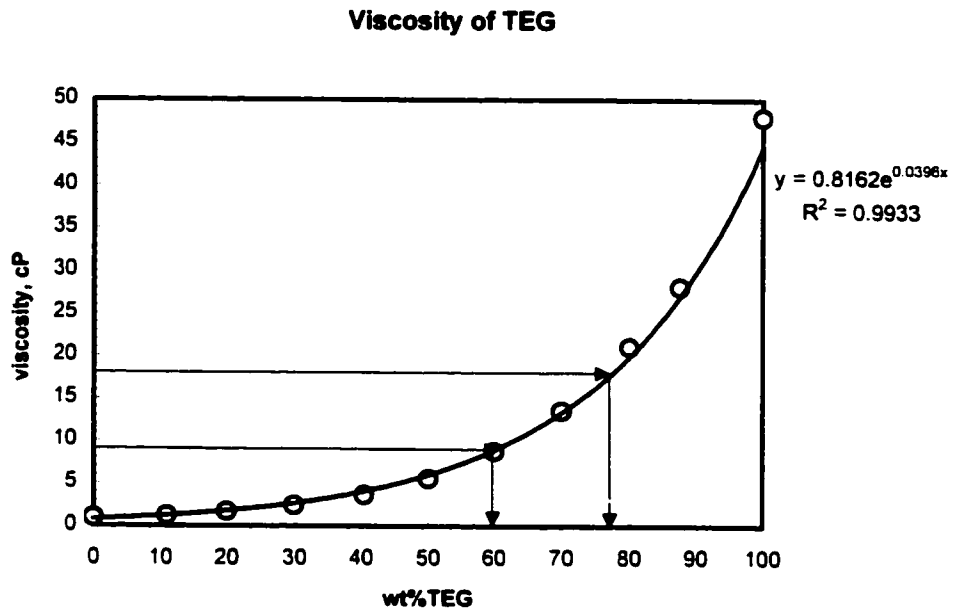


Figure 2-9. Variation of viscosity for different water solutions of TEG (wt%). Dotted symbols represent the actual measurements while the solid line is their best fit.

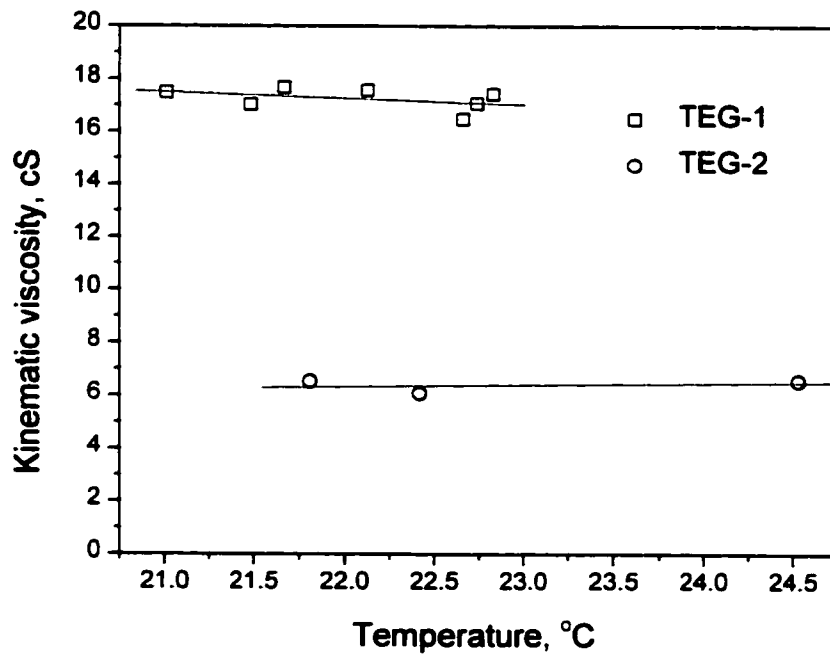


Figure 2-10. Dependence of viscosity on temperature for TEG–water mixtures (large scale experiments).

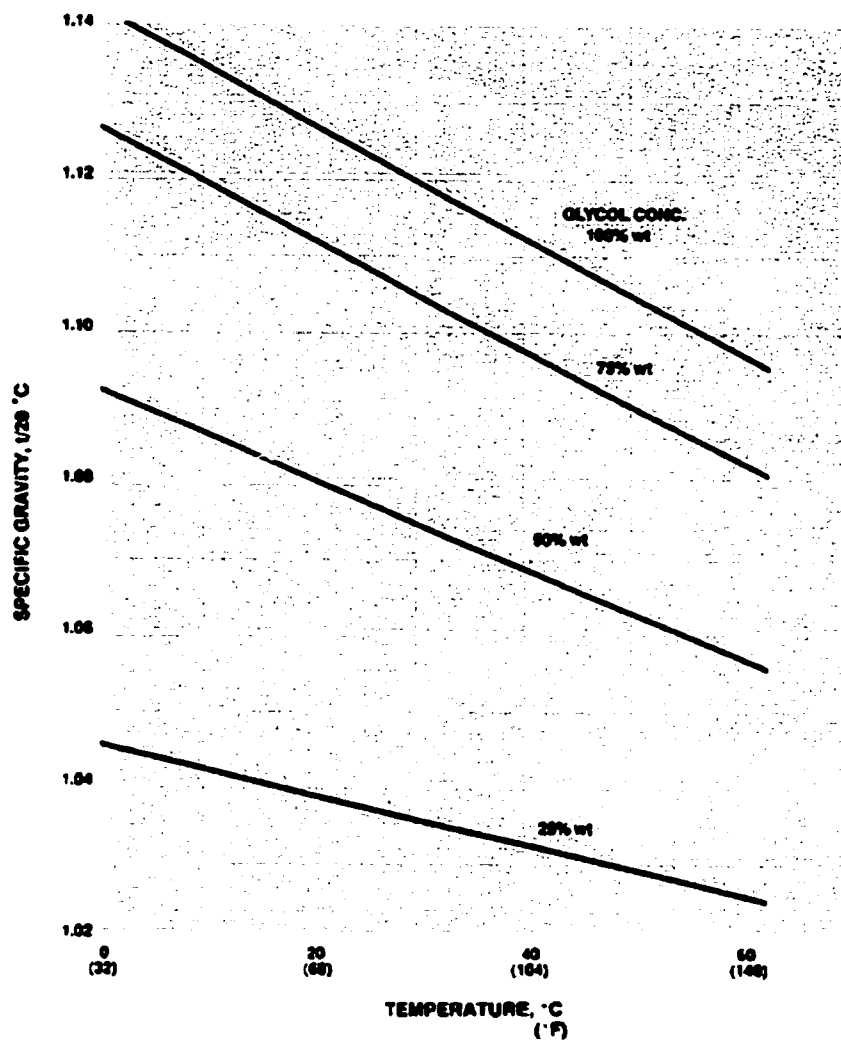


Figure 2-11. Specific gravities of triethylene glycol aqueous solutions at various concentrations. Data are taken from Shell Chemical –online library.

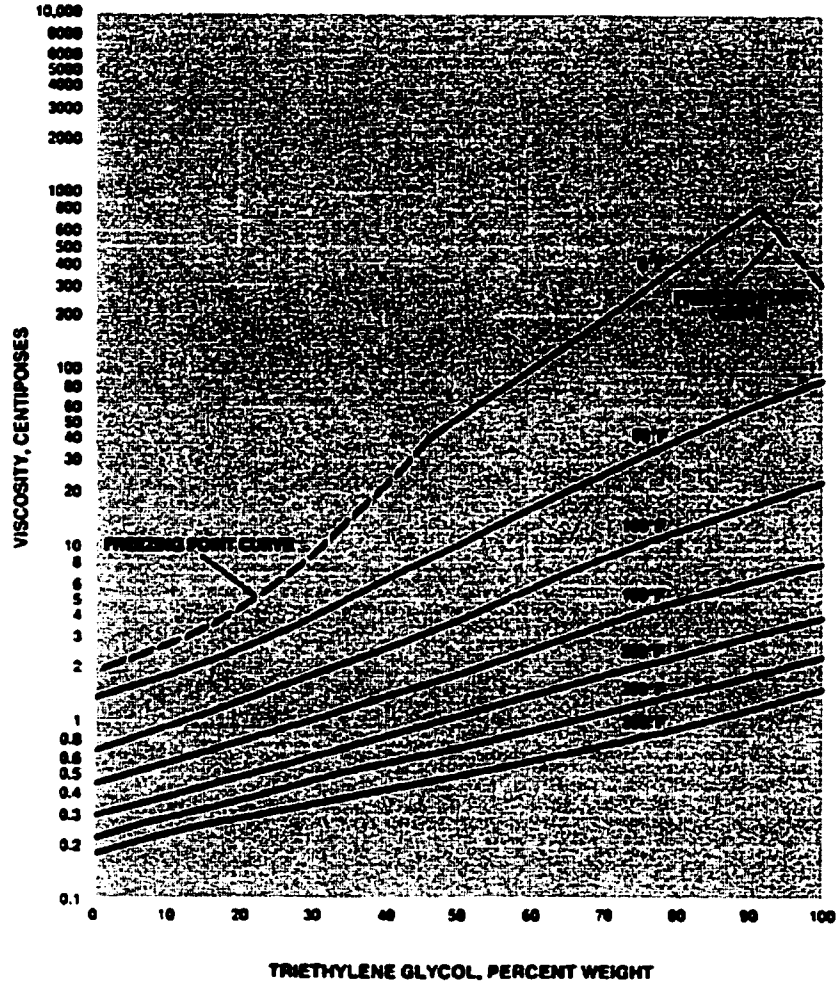


Figure 2-12. Viscosities of triethylene glycol aqueous solutions. Data are taken from Shell Chemical –online library.

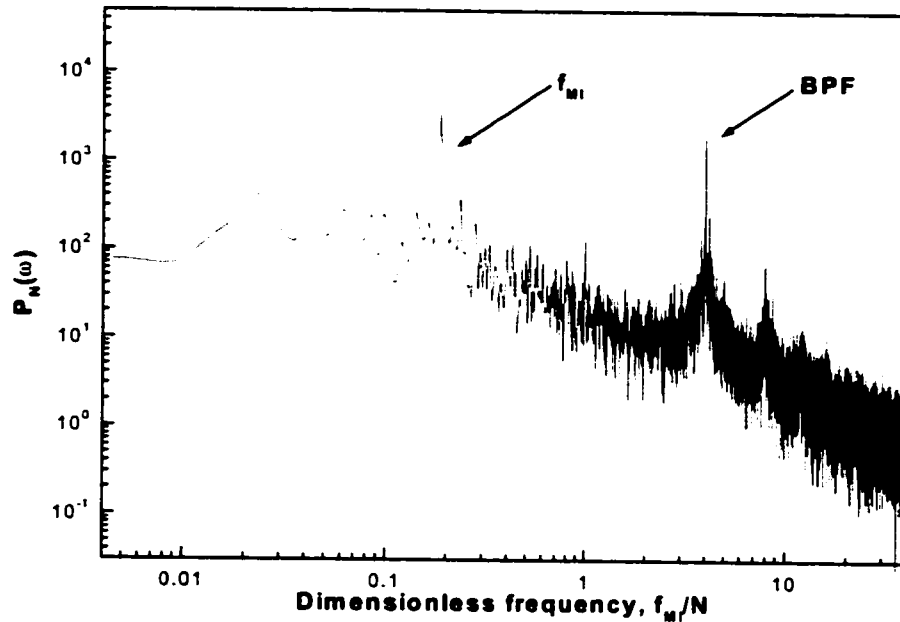


Figure 2-13. Frequency spectrum for the axial velocity at $2r/D=1.05$ showing the presence of the BPF and MI.

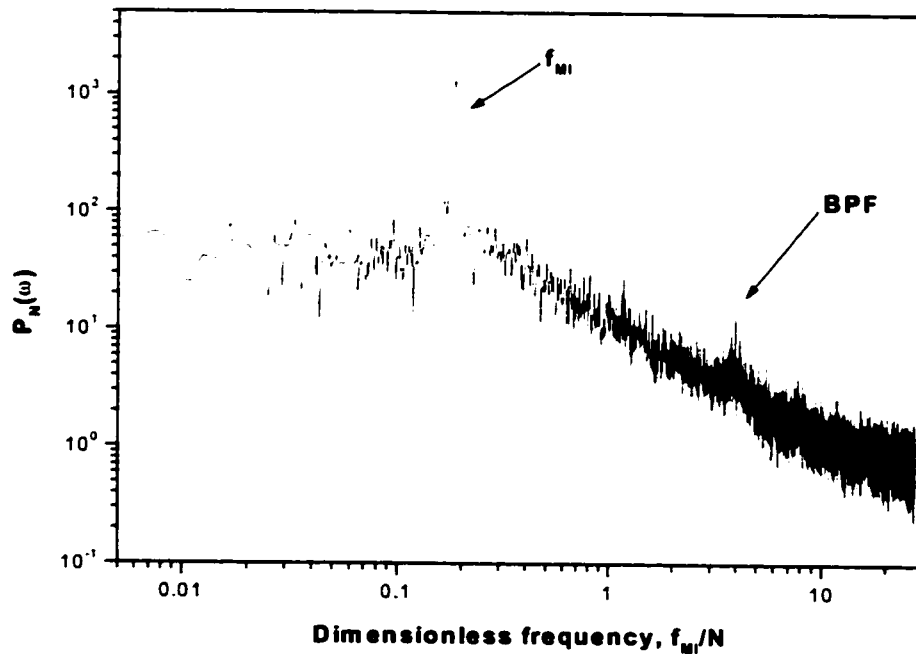


Figure 2-14. Frequency spectrum for the axial velocity at $2r/D=1.35$ showing the presence only of the MI. Note that the $f_{MI}=0.92\text{Hz}$, (45° PBT, $C/D=0.5$ and $D=T/2$, fluid bayol, $Re=24,000$).

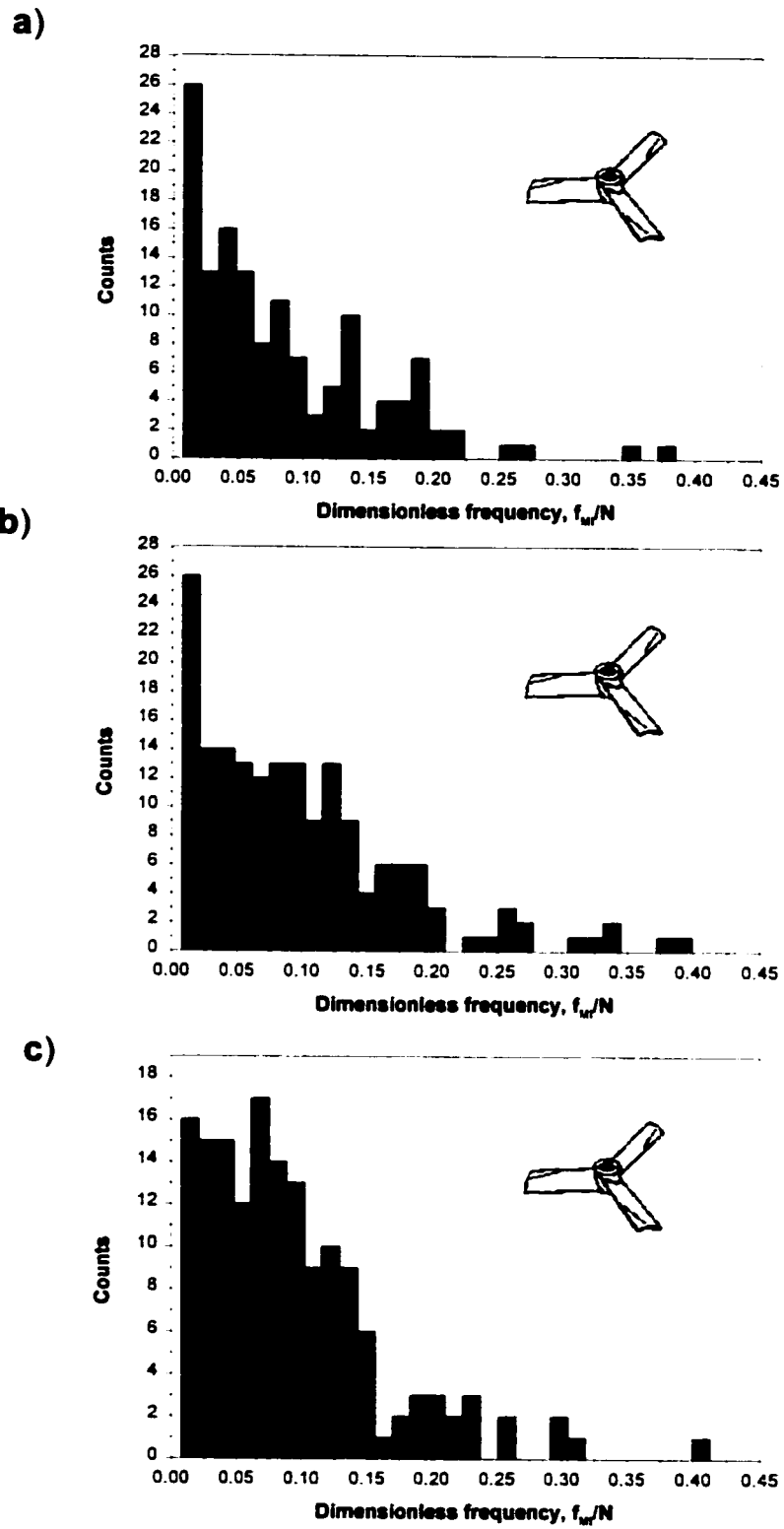


Figure 2-15. Distribution of MI frequency for *HE3* with constant impeller diameter, $D=T/3$ and various C/D ratios: a) $C/D=0.40$, b) $C/D=0.80$ and c) $C/D=1.0$

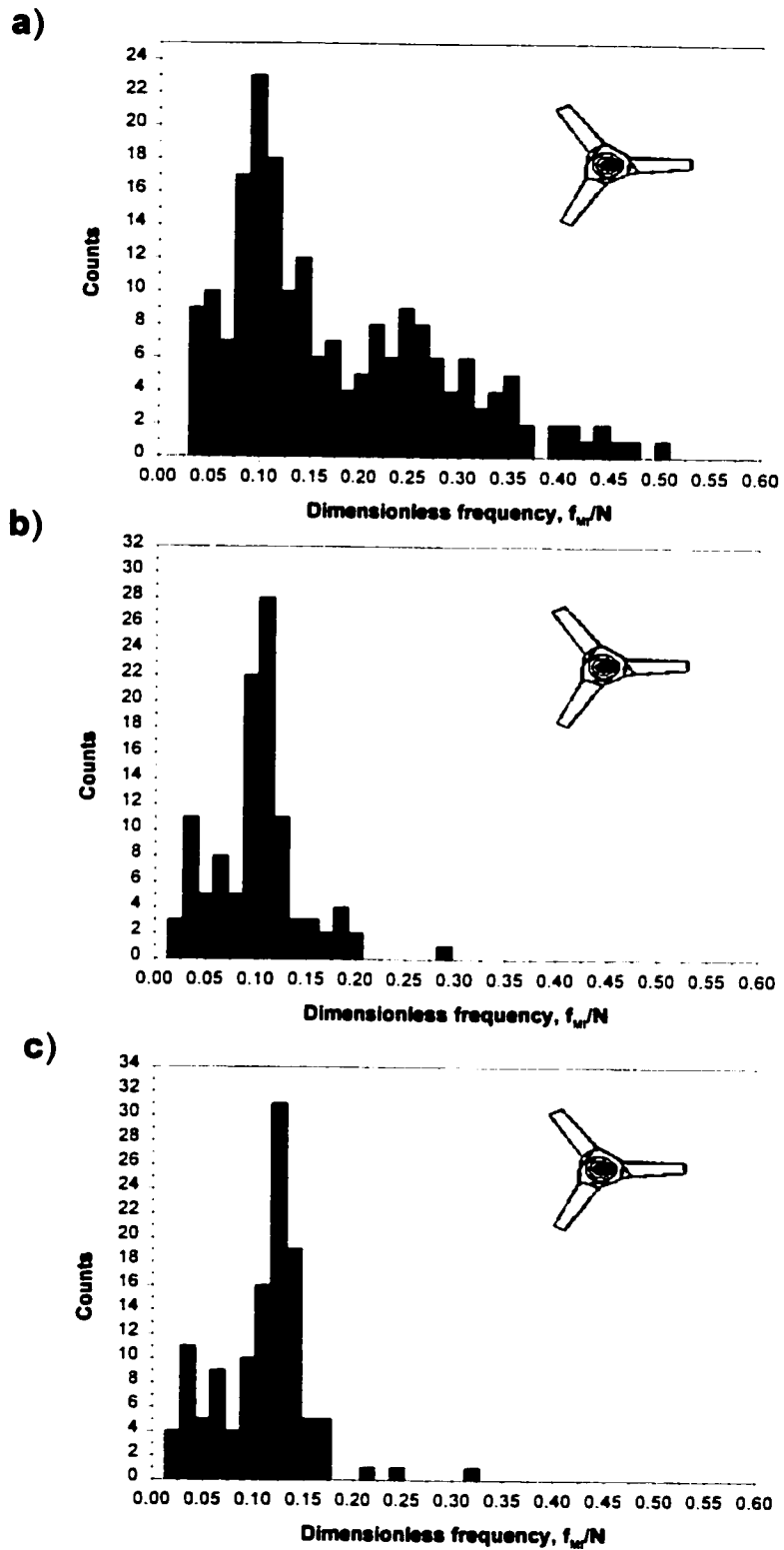


Figure 2-16. Distribution of MI frequency for *A310* with constant impeller diameter, $D=0.58T$ and various C/D ratios: a) $C/D=0.33$, b) $C/D=0.50$ and c) $C/D=0.67$.

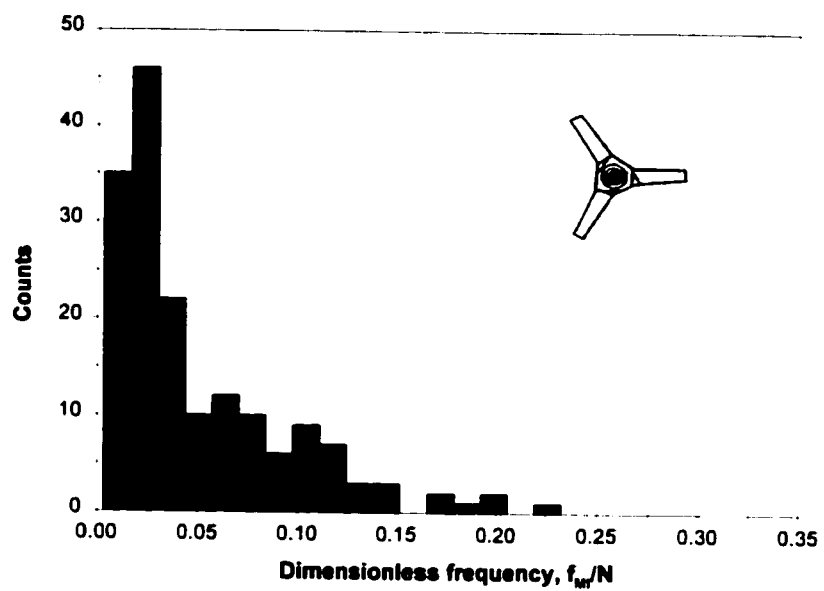


Figure 2-17. Distribution of MI frequency for the large-scale *A310* ($D=0.35T$, $C/D=1.0$) at $Re=5.65 \times 10^4$. No coherent frequency was detected.

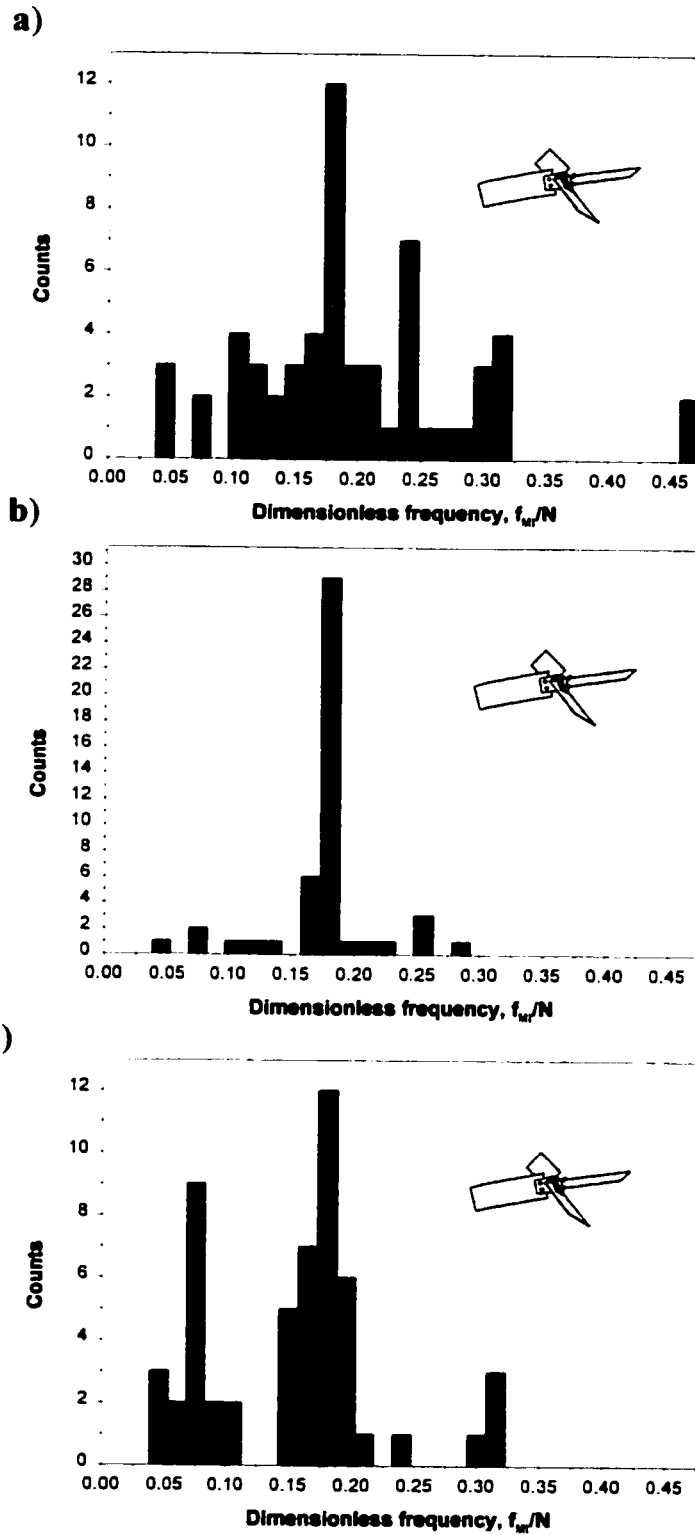


Figure 2-18. Distribution of MI frequency for 45° PBT with constant impeller diameter, $D=T/2$ and various C/D ratios: a) $C/D=0.33$, b) $C/D=0.50$ and c) $C/D=0.67$, $Re=48,000$.

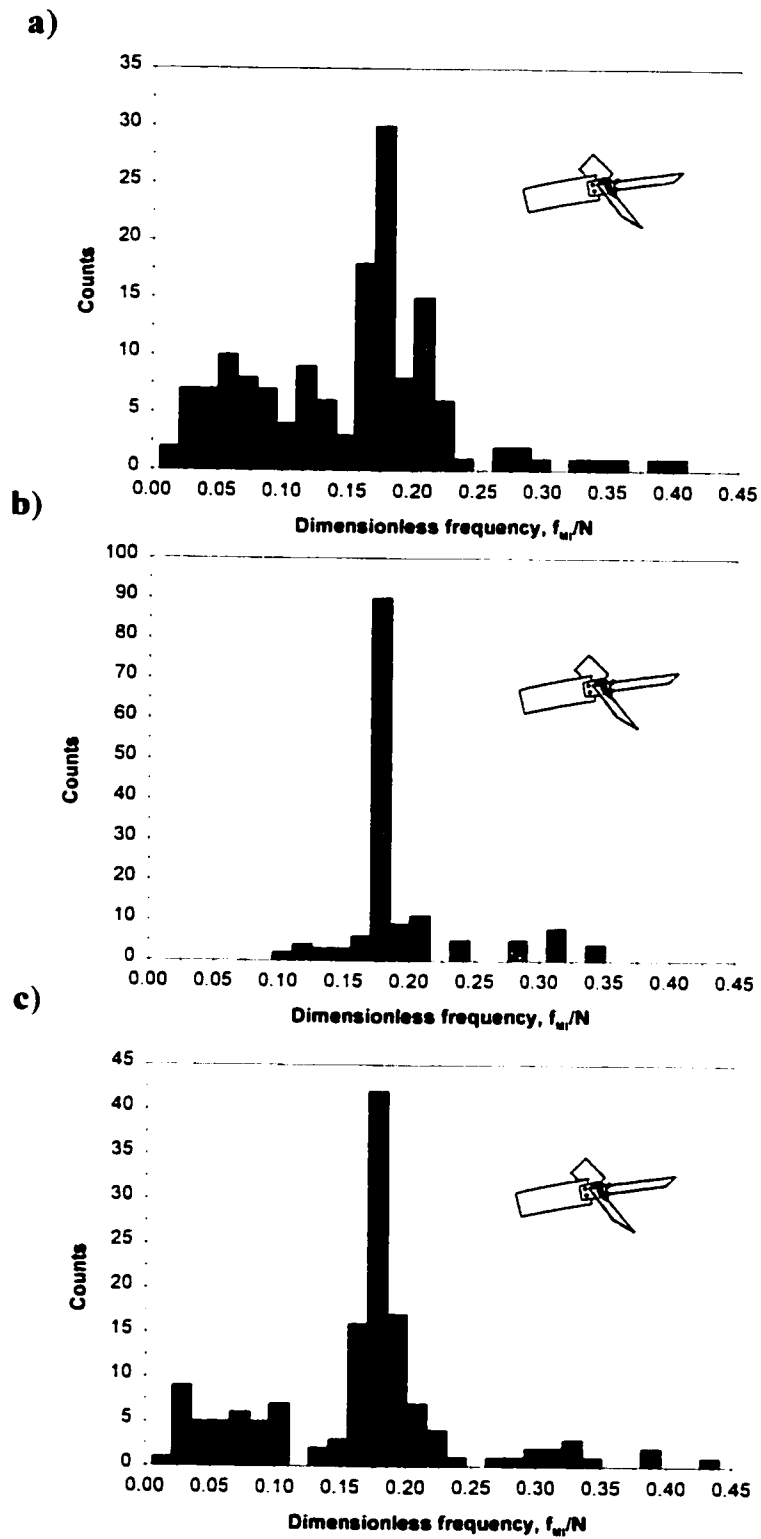


Figure 2-19. Distribution of MI frequency for large-scale 45° PBT with constant impeller diameter, $D=T/2$ and various C/D ratios: a) $C/D=0.33$, b) $C/D=0.50$ and c) $C/D=0.67$. The Reynolds number was greater than 20,000 for all runs.

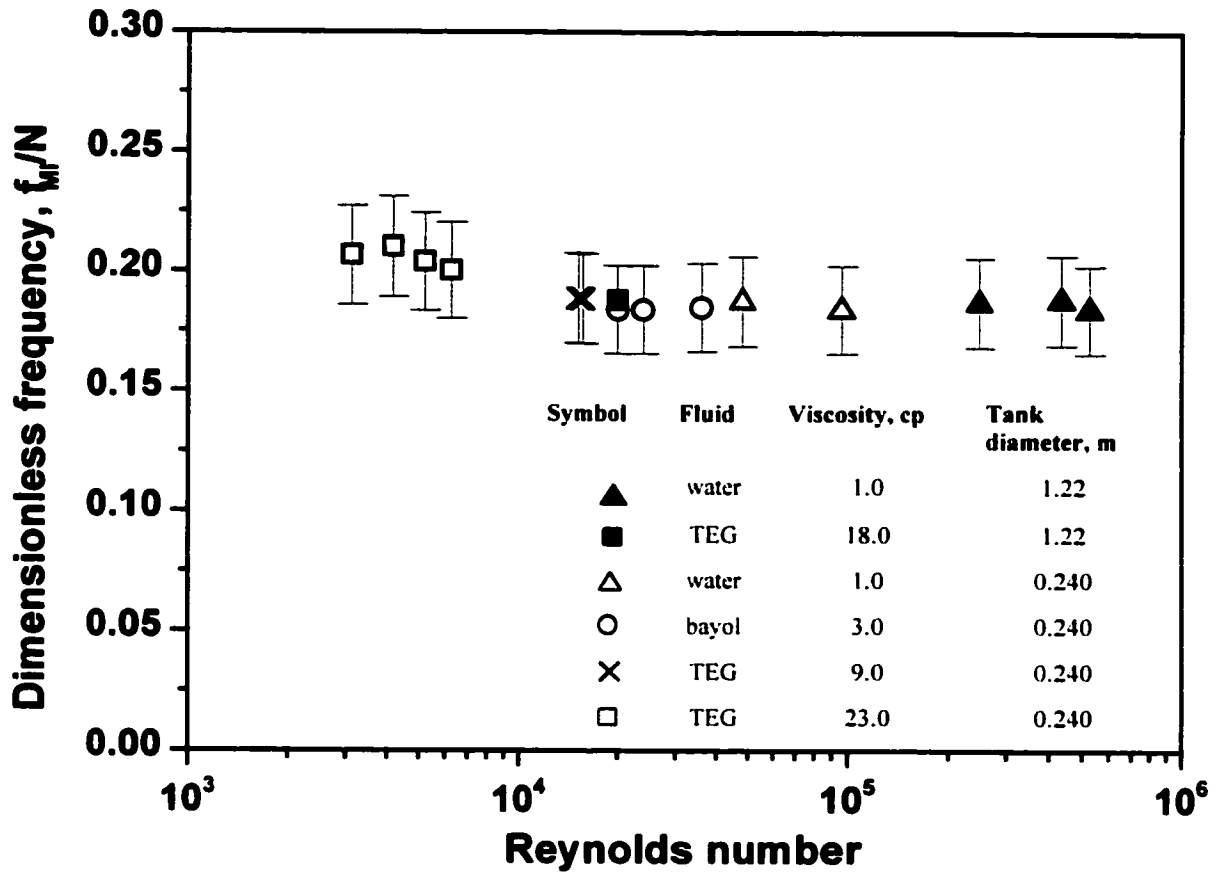


Figure 2-20. Combined results showing the scaling of the dimensionless frequency for the resonant geometry (45° PBT, $D=T/2$, $C/D=0.50$) small and large scale experiments.

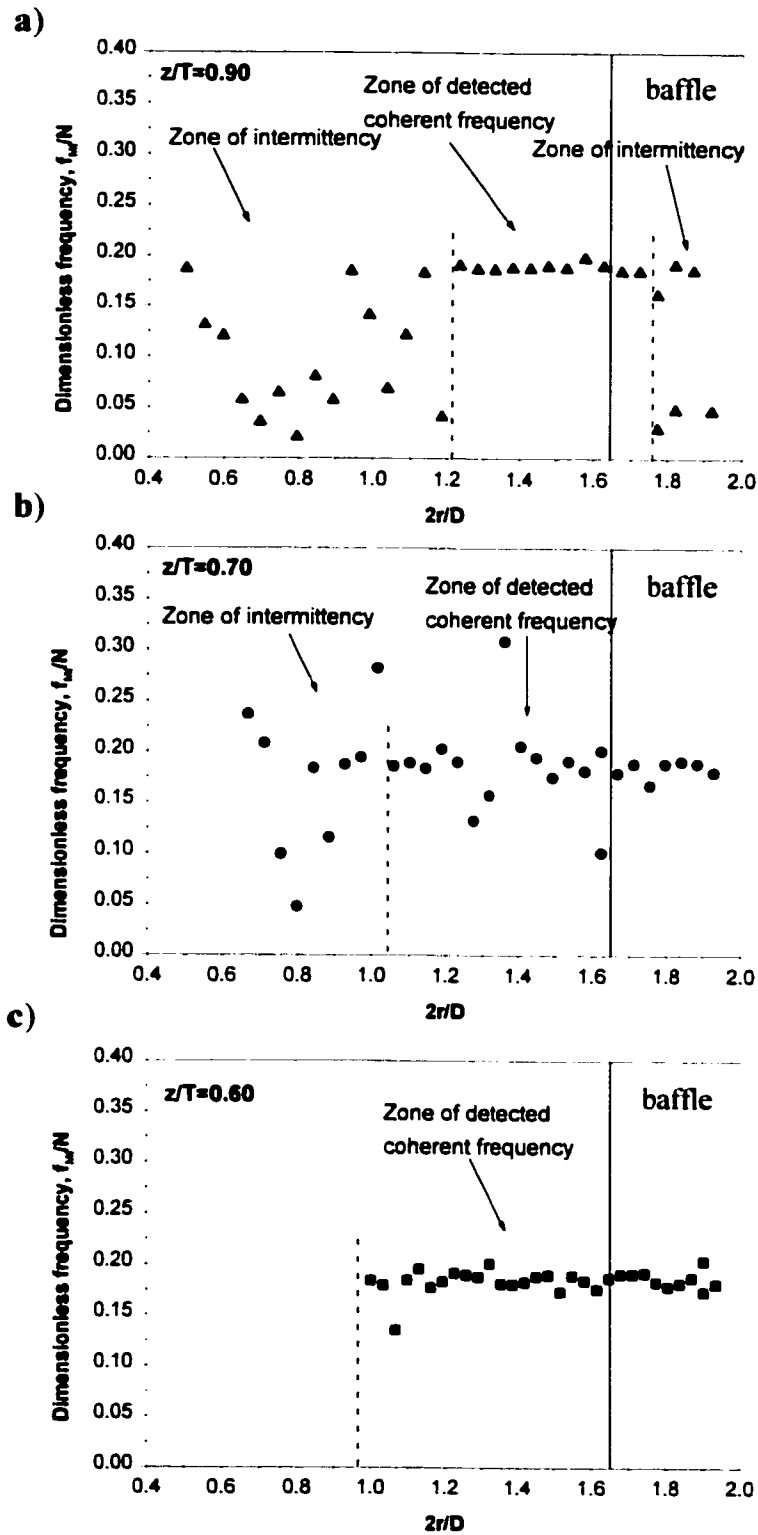


Figure 2-21. Zones of the large-scale tank showing the spatial position where the coherent frequency is found at three different axial locations a) $z/T=0.60$, b) $z/T=0.70$ and c) $z/T=0.90$. Configuration 45° PBT $D=T/2$, $C/D=0.50$, $Re=20,000$.

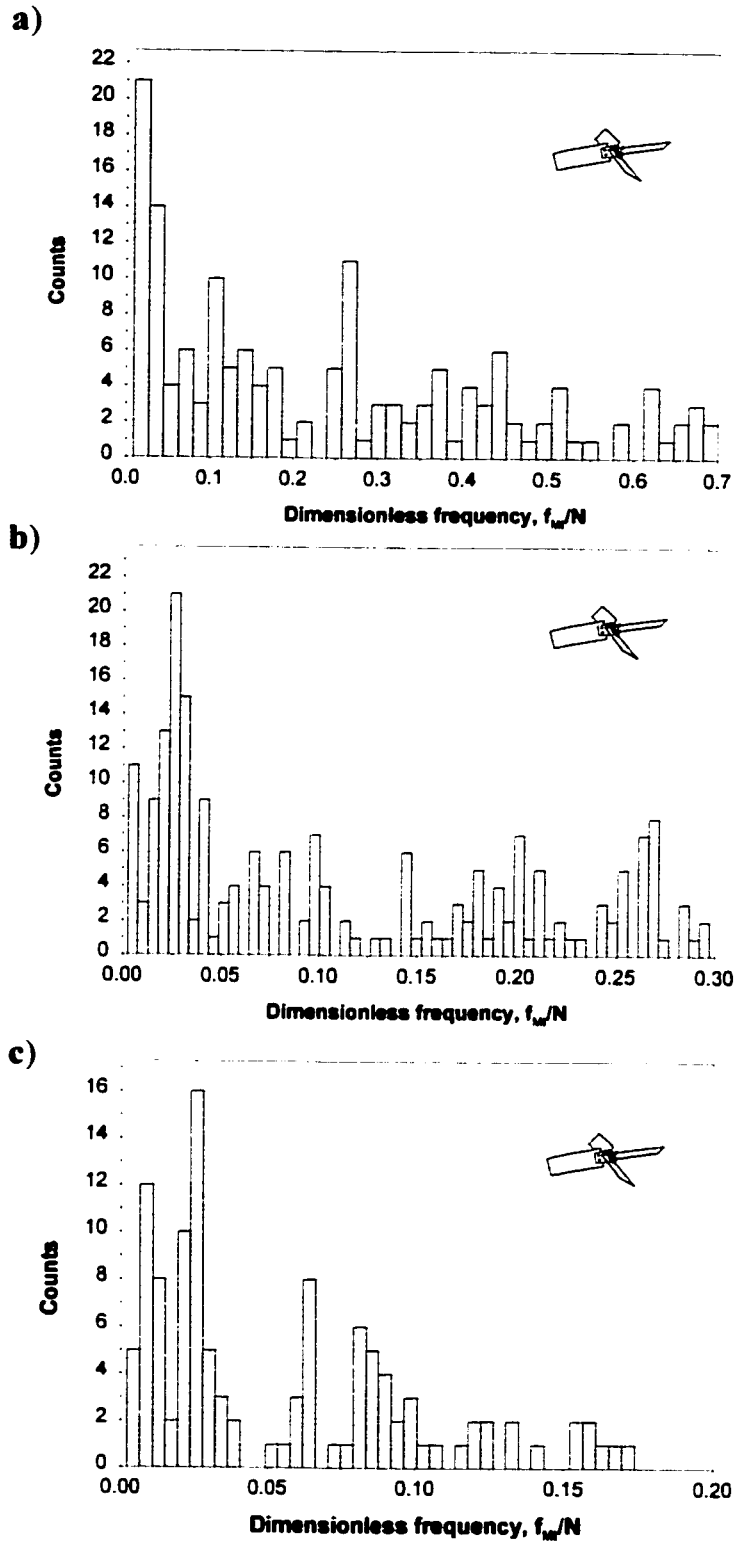


Figure 2-22. Distribution of MI frequency for small-scale 45° PBT with constant impeller diameter, $D=T/3$ and $C/D=0.50$ at various Reynolds numbers: a) $Re=18,000$, b) $Re=20,000$ and c) $Re=25,000$.

Chapter 3: Large eddy simulation

Based on the experimental evidence of Chapter 2 showing the presence of a strong coherent large-scale macroinstability in the flow field produced by a 45° PBT, in this chapter large eddy simulations (LES) are used to probe these macroinstabilities. Several important issues have to be considered in order to do the simulation correctly. First and most important, an accurate modeling approach which is able to represent the large scales of motion has to be selected. All simulations have to be transient and fully three-dimensional which requires exact modeling of the impeller revolution. This is done with the sliding mesh technique. The LES model is a natural choice for the turbulence model. Differences between LES and transient two equation k-ε modeling will be discussed. The results show that LES with a full 360° sliding mesh is able to predict the macroinstabilities correctly even at a coarse grid resolution.

3.1 Introduction

In the past few years studies of computational fluid dynamics (CFD) simulations have shown that the flow field in a mixing tank can be simulated with reasonable accuracy. Simulations are less costly and can provide more detailed information (in some cases) than experiments. All experimental techniques require a significant investment in equipment and training and are usually restricted to examining small-scale models, since the analysis of full-scale equipment in laboratory setting is often impossible.

The complexity of the flow field in mixing tanks requires careful selection of turbulence models. The difficulty arises from the fact that the flow field cannot be described as a classical three-dimensional turbulence that is stationary and fully isotropic. In reality, the flow field very close to the impeller is highly anisotropic due to the strong trailing vortices at the tip of the impeller blades. These die out quickly, leading to an impeller discharge stream which is effectively isotropic over the inertial subrange of the turbulent spectrum. In the bulk of the tank macroinstabilities dominate and the flow is quasi-stationary, anisotropic on the largest scales of motion and far from equilibrium (Kresta, 1998). In the top third of the tank, even a Reynolds number higher than 2×10^4

(the fully turbulent limit at the impeller) does not ensure fully turbulent flow (Bittorf and Kresta, 2001).

The choice of CFD models depends on what level of detail is needed from the simulations, or down to which eddy sizes the Navier-Stokes equations have to be resolved. The answer to this question depends on the critical process objective in the mixing tank. If one needs to resolve only the mean velocity field and get information for the overall circulation pattern, the steady state, standard k - ϵ model can give a fast solution. Transient calculations add another dimension to the simulations; the flow field now is evolving with time. Fully transient, 3-D simulations can provide information about the time varying large scale eddies. This may be important if the time scale of the blending (or reaction) process carried out in stirred tank is short compared to the lifetime of the large-scale motions. The feedstream jet intermittency discussed by Houcine et al. (1999) gives an example of how meso-mixing is affected by large-scale flow instabilities.

Classification of models for time varying flow is based on their ability to resolve different temporal and spatial scales of motion. In order of increasing resolution, three main groups exist:

- i. transient k - ϵ model
- ii. large eddy simulations (LES) and
- iii. direct numerical simulations (DNS).

We will discuss first the two extremes: transient k - ϵ and DNS models, pointing out their advantages and disadvantages and thus showing why the intermediate LES model is the best choice for simulating the large scale macroinstabilities in mixing tanks.

The transient k - ϵ model is based on the time averaged Navier-Stokes equations, also known as the Reynolds averaged Navier Stokes (RANS) equations. These equations are composed of mean quantities instead of instantaneous time-dependent values. The Reynolds averaging process leads to an additional six unknowns, the Reynolds stresses. Various models for the Reynolds stresses are available, but the most widely applied approach in engineering applications models the Reynolds stresses using the turbulent kinetic energy, k , and its rate of dissipation ϵ . When combined with the assumption of

local isotropy, this is the basis of the very well known two-equation isotropic k - ϵ model. This model averages all the transients (fluctuations) combining them into k . This model is not designed to simulate large-scale macroinstabilities.

In the case of DNS the governing Navier-Stokes equations are solved directly without time averaging. All scales of turbulent motion are simulated by means of the classical transient three-dimensional Navier-Stokes equations. The only limitation is due to the spacing of the computational grid, which must be fine enough to resolve the smallest eddies at or below the Kolmogorov length scale. From dimensional analysis (Frisch, 1995) the Kolmogorov length scale scales with $Re^{-3/4}$ times the integral length scale, so the number of required grid points scales as $Re^{9/4}$. Even with recent advances in computational speed, DNS is still constrained to simple geometries and relatively low Reynolds numbers.

To simulate the macroinstability correctly it is sufficient to resolve only the anisotropic large-energy containing motions and model the effect of the isotropic small scale eddies. This approach is pursued in so called Large Eddy Simulations (LES). The LES approach resolves directly only the "scale of interest" or those scales which are associated with the large-scale anisotropic motions. The cut-off length scale is usually chosen to lie in the inertial sub range of turbulence. Below this length scale all the turbulence is absorbed into a sub-grid scale (SGS) model. The consequence of the LES-approach in mixing tanks is that both the average flow field and the large eddies associated with impeller blade passages and flow past the baffles can be resolved for both high and moderate Reynolds numbers. The grid requirements are less severe than DNS because only the large-scale motions are directly computed.

Modeling of macroinstabilities requires not only the proper turbulence model but also a technique to model the rotation and geometry of the impeller exactly. This requires that full 360° transient simulations be performed. Three approaches are reviewed below, with particular attention paid to the sliding mesh technique the only one incorporating both the transient and the three dimensional character of the flow field.

The earliest reports of computational simulations of the 45° PBT are given by Ranade et al. (1989). They reported three-dimensional steady-state simulations applying

the k - ϵ model. To simulate the impeller they used boundary conditions developed from experimental data. This models the impeller as a “black box” ignoring the individual impeller blades and suppressing feed back to the impeller from the tank. Later the study was extended (Ranade et al, 1991) to simulate mixing of an inert tracer, with limited success. Fokema et al (1994) applied two different sets of boundary conditions in simulation of two off-bottom clearances of a 45° PBT. They concluded that the correct prediction of the velocity field is possible only if the impeller location is considered and the impeller boundary conditions are very carefully specified. The need for experimentally measured time-averaged boundary conditions severely limits this computational technique. In order to overcome this limitation the sliding mesh and multiple reference frame (MRF) models were developed.

In the MRF model a rotating frame is used for the region containing the impeller while a stationary frame is used for regions that are stationary: the baffles and tank wall. In the rotating frame the impeller is at rest, while in the stationary frame the baffles and tank wall are at rest. The governing momentum equations are then solved in two different reference frame domains in such a way that on the MRF surface the information from the impeller domain is used as a boundary condition for solving the set of equations in the stationary frame. This means that the impeller is not moving physically; i.e. the orientation of the impeller blades relative to the baffles does not change during the simulation. The model therefore spatially averages all transients. It is recommended if the interaction between the impeller and baffles is weak and the flow is stationary.

The MRF model with a combination of different turbulence steady state models was applied by Marshall et al. (1999) to predict the mean velocity field, power number and flow number for a Lightnin A310 impeller in a large-scale tank. All turbulence models performed well, predicting the flow and power number within 10% error.

The major drawback of the MRF model is the lack of prediction of time varying eddies in the mixing tank. Harvey et al. (1995) described a transient approach which simulates the impeller rotation explicitly. This is done by physically moving the grid: a technique known as the sliding mesh.

Like MRF, the sliding mesh technique also divides the grid into two separate parts: one associated with the rotating impeller and the other one associated with the stationary baffles and the tank walls. At every time step the impeller grid is moved along the sliding surface and all the conservation equations are solved in an iterative process until convergence is reached. During each step of those calculations information is passed through the sliding interface from the rotating region to the stationary region and back again. The sliding mesh model is the most rigorous and informative method for simulating the impeller rotation. It provides information for the fully transient three-dimensional nature of the flow field produced by the impeller. Results from the sliding mesh combined with a standard k - ϵ model were discussed by Bakker et al (1997) who admitted that a finer grid would be necessary to resolve the trailing vortices. They confirmed the high computational cost of sliding mesh predictions due to the number of impeller revolutions (approximately 20), which are necessary to yield a stationary or quasi-steady state solution. Intensive steady and unsteady computation of the flow field generated by 45° PBT was also performed by Wechsler et al. (1999). They validated the results obtained from steady and unsteady simulations with experimental data of Schafer et al. (1998). The grid sensitivity analysis showed that close to the impeller blades the predicted mean velocities matched the experimental data. Outside the impeller swept volume some discrepancies were detected. It was concluded that further grid refinement would overcome this problem.

Since the macroinstability was observed in both small and large-scale experiments, this study is logically extended to use available CFD methods to examine the macroinstability in more detail. The macroinstability is a large-scale unsteady phenomenon (Bruha and Fort, 1996, Myers et al, 1997, Kresta and Wood, 1993), so a model which resolves at least the large scales of transient motion, is needed. The objective of this work is to validate the LES approach and use it to probe the macroinstability for the small-scale resonant geometry ($T=0.240\text{m}$, 45° PBT, $D=T/2$, $C/D=0.50$ at $Re=48,000$). First a brief overview of the two equation k - ϵ model and LES-Smagorinski model will be given, followed by a description of the simulation procedure. The results will show that LES combined with a sliding mesh provides a very accurate means for simulation of large-scale macroinstabilities in a stirred tank.

3.2 The choice of turbulent model

In turbulence, a description of the flow at all points in time and space is not feasible. Instead, following the idea of Reynolds decomposition the flow can be described in terms of mean quantities, such as mean velocity, U_i . The mean flow is defined by an average that for a statistically steady flow is a time average. Adopting this formulation leads us to the Reynolds averaged Navier-Stokes (RANS) equations. The equations are valid when flow conditions do not change with time. The mean flow is a long time average that contains no *unsteadiness* (transients) i.e. all of the fluctuations are considered as a part of the turbulence so the result of a computations should be a steady flow.

The concept of unsteady RANS has been proposed by Speziale (1998) and it is claimed that this type of calculation is a sort of very large eddy simulations (VLES). Such calculations rely on traditional RANS models but are deliberately unsteady. It is simple to describe the numerical realization of URANS, but the physical implications are questionable. The turbulent flow is modeled as a flow field that is periodic and smoother but representative in a sense so that it reflects the large-scale dynamics of the true flow (Spalart, 2000). Such a field can be defined from the turbulent one by phase averaging. The averaging procedure creates Reynolds stresses of two kinds, and in URANS both are left to the turbulence modeling.

The LES is based on the filtered equations of motion. Mathematically the equations obtained after filtering are analogous to the equation used in URANS model. It can be proven that the filtering operation is equivalent to the averaging if a certain shape of filter is selected. A question then logically arises: What is the difference between the URANS and the LES approach? The difference can be found in the numerical realization and empiricism involved. The LES is more natural and can be physically justified while the URANS modeling applies so much empiricism that it is highly unreliable.

3.2.1 Two equation k- ϵ model

The mathematical expression of a momentum balance on an incompressible fluid is given by the Reynolds averaged Navier-Stokes set of differential equations. By

expressing the instantaneous velocity as a simple sum of a time averaged mean velocity U_i and a turbulent fluctuating component u'_i , the instantaneous form of a momentum Navier-Stokes equations is written

$$\frac{\partial(u'_i + U_i)}{\partial t} + (u'_j + U_j) \frac{\partial(u'_i + U_i)}{\partial x_j} = -\frac{1}{\rho} \frac{\partial(p' + P)}{\partial x_i} + \nu \frac{\partial^2(u'_i + U_i)}{\partial x_j^2} + g_i \quad (3.1)$$

The time averaged form of Equation 3.1 is

$$\frac{\partial U_i}{\partial t} + U_j \frac{\partial U_i}{\partial x_j} = -\frac{1}{\rho} \frac{\partial P}{\partial x_i} + \frac{\partial}{\partial x_j} \left(\nu \frac{\partial U_i}{\partial x_j} - \overline{u'_i u'_j} \right) + g_i \quad (3.2)$$

The Reynolds averaging procedure introduces a new term $-\overline{u'_i u'_j}$, which represents the stresses appearing in the flow due to the turbulent velocity fluctuations. There are now 10 unknowns to solve, and only 4 equations. If we want to predict the turbulent flow field we must model the Reynolds stresses in terms of known quantities. By analogy with the viscous stress in laminar flow the turbulent stresses can be related to the mean-velocity gradients. For general flow situations (Rodi, 1987), this concept may be expressed as:

$$-\overline{u'_i u'_j} = \nu_t \left(\frac{\partial U_i}{\partial x_j} + \frac{\partial U_j}{\partial x_i} \right) - \frac{2}{3} k \delta_{ij} \quad (3.3)$$

ν_t is the turbulent (eddy) viscosity which is not a fluid property but depends on the state of turbulence. When Equation 3.3 is used to eliminate the $\overline{u'_i u'_j}$ in the momentum equation (Equation 3.2) the second part can be absorbed in the pressure-gradient term so that in effect the static pressure is replaced as unknown quantity by the pressure $P + \frac{2}{3} k$.

The appearance of k does not necessitate the determination of k ; rather it is the distribution of the eddy viscosity, ν_t , only that has to be determined.

The simplest possible model of turbulence is the Prandtl-Kolmogorov eddy diffusivity:

$$\nu_t = C_0 k^{1/2} L_0 \quad (3.4)$$

where C_o is a constant, L_o is the length scale of energy containing eddies, and $k^{1/2}$ is the characteristic velocity scale. As the energy is contained mainly in the large-scale fluctuations, $k^{1/2}$ is a velocity scale for the large-scale turbulent motion. The k- ϵ model uses two equations: one for k and a second equation that relates the dissipation, ϵ , directly to the kinetic energy k eliminating the need for any length scale specification. The dissipation, ϵ is approximated by the usual inertial subrange spectral transfer relation

$$\epsilon = C_\epsilon \frac{k^{3/2}}{L_o} \quad (3.5)$$

which contains the implicit assumption that the mixing length L_o is the same as the scale of the eddies that contain most of the energy. It is more accurate to refer to ϵ as the fluctuating vorticity or the rate of turbulence kinetic energy transfer through the inertial subrange, rather than dissipation. As Rodi (1987) explains, "An exact transport equation for the fluctuating vorticity can be derived from the Navier-Stokes equations, and used to derive a conservation equation for the dissipation ϵ . This equation contains a number of complicated correlations whose behavior is little known, and for which fairly drastic model assumptions must be introduced in order to make the equation tractable". The constants required for the equation, however, are derived from a set of experiments on classical turbulent flow, such as grid turbulence, and should not be regarded as arbitrary tuning parameters. Combining Equation 3.4 and Equation 3.5 we obtain for the eddy viscosity ν_t

$$\nu_t = C_o C_\epsilon \frac{k^2}{\epsilon} \quad (3.6)$$

The latter equation used in the k- ϵ model requires that the Reynolds number be high enough for the inertial subrange to exist. The inertial subrange controls the rate of energy transfer from large to small scales. From the log-law constant shear layer, we have that $C_\epsilon = C_o^3$ so Equation 3.6 becomes

$$\nu_t = C_o^4 \frac{k^2}{\epsilon} \quad (3.7)$$

The k-equation is a balance between the diffusion of turbulence due to velocity and pressure fluctuations, the production of k by mean shear and acceleration (or by interaction of the Reynolds stresses with mean velocity gradients) and the dissipation of k by viscous action into heat. The k-equation can be derived exactly from the Navier-Stokes equations (see Hinze, 1959) but the exact form of it is of little use for turbulence modeling because new unknown correlations appeared in the diffusion and dissipation terms. The exact k-equation reads:

$$\begin{aligned}
 \underbrace{\frac{\partial k}{\partial t}}_{\text{Rate of change}} + \underbrace{U_i \frac{\partial k}{\partial x_i}}_{\text{Convection}} = & \underbrace{-\frac{\partial}{\partial x_i} \left(u_i' \left(\frac{\overline{u_i' u_i'} + P}{2} + \frac{P}{\rho} \right) \right)}_{\text{Diffusion}} - \underbrace{\overline{u_i' u_i'} \frac{\partial U_i}{\partial x_i}}_{\text{work of deformation of the mean flow}} \\
 + \underbrace{v \frac{\partial}{\partial x_i} u_i' \left(\frac{\partial u_i'}{\partial x_i} + \frac{\partial u_i'}{\partial x_i} \right)}_{\text{work done by viscous shear stress}} - & \underbrace{v \left(\frac{\partial u_i'}{\partial x_i} + \frac{\partial u_i'}{\partial x_i} \right) \frac{\partial u_i'}{\partial x_i}}_{\varepsilon = \text{viscous dissipation}}
 \end{aligned} \tag{3.8}$$

In order to make use of k-equation (Equation 3.8) all of the terms on the RHS have to be approximated for isotropic flow. The approximation is considered valid if the equation produces a log law mean velocity profile and realistic wall shear stress in the region close to solid surfaces. Using the eddy viscosity and diffusivity expressions for $-\overline{u_i' u_i'}$ and taking into account that the diffusion flux of k is often assumed proportional to the gradient of k , the k-equation reduces to:

$$\frac{\partial k}{\partial t} + U_i \frac{\partial k}{\partial x_i} = \underbrace{\frac{\partial}{\partial x_i} \left(C_k v_t \frac{\partial k}{\partial x_i} \right)}_{\text{Diffusion}} + \underbrace{\frac{\partial U_i}{\partial x_i} \left(v_t \left(\frac{\partial U_i}{\partial x_i} + \frac{\partial U_i}{\partial x_i} \right) - \frac{2}{3} k \delta_{ii} \right)}_{\Pi = \text{turbulent production}} - \varepsilon \tag{3.9}$$

where the turbulent production of k is denoted by Π . To make use of the Prandtl-Kolmogorov eddy viscosity, v_t , a conservation equation for ε is required. The model ε -equation used by Rodi (1987) in the two equation k- ε model is

$$\frac{\partial \varepsilon}{\partial t} + \underbrace{U_i \frac{\partial \varepsilon}{\partial x_i}}_{\text{Convection}} = \underbrace{\frac{\partial}{\partial x_i} \left(C_{\varepsilon} v_t \frac{\partial \varepsilon}{\partial x_i} \right)}_{\text{Diffusion}} + \underbrace{C_{1\varepsilon} \frac{\varepsilon}{k} \Pi}_{\text{Production}} - \underbrace{C_{2\varepsilon} \frac{\varepsilon^2}{k}}_{\text{Dissipation}} \tag{3.10}$$

The second term in the left side of Equation 3.10 is the convection of fluctuating vorticity through the control volume. The first term on the right side represents the diffusion of fluctuating vorticity out of the control volume assuming eddy diffusivity $\nu_\epsilon = C_{\nu\epsilon} \nu_t$. The last two terms on the right hand side of Equation 3.10 are the generation and destruction of the fluctuating vorticity within the control volume.

The physics behind the generation and destruction terms in the ϵ equation can be explained by interpreting the ratio between ϵ and k . This ratio is proportional to the timescale, t_ϵ , of energy transport through the spectrum. Expressing the generation rate and destruction rate in terms of t_ϵ , leads us to the main assumption used in Equation 3.10; that the rate of generation of ϵ is proportional to the rate of production of k . These both feed the large-scale end of the spectrum. The destruction rate is proportional to the dissipation, which provides the sink at the small scales. The complete set of equations for the k - ϵ model is summarized as follows (fully 3-D transient, incompressible form of the equations):

i. Continuity

$$\frac{\partial U_i}{\partial x_i} = 0 \quad (3.11)$$

ii. Momentum

$$\frac{\partial U_i}{\partial t} + U_j \frac{\partial U_i}{\partial x_j} = -\frac{\partial}{\partial x_i} \left(\frac{P}{\rho} + \frac{2}{3} k \right) + \frac{\partial}{\partial x_j} \left(\nu_t \left(\frac{\partial U_i}{\partial x_j} + \frac{\partial U_j}{\partial x_i} \right) \right) \quad \text{for } i = 1, 2, 3 \quad (3.12)$$

where the $\frac{\partial U_i}{\partial t} = 0$ for steady flow.

iii. Turbulent kinetic energy

$$\frac{\partial k}{\partial t} + U_j \frac{\partial k}{\partial x_j} = \frac{\partial}{\partial x_i} \left(C_k \nu_t \frac{\partial k}{\partial x_i} \right) + \Pi - \epsilon \quad (3.13)$$

iv. Dissipation (spectral transfer rate)

$$\frac{\partial \varepsilon}{\partial t} + U_i \frac{\partial \varepsilon}{\partial x_i} = \frac{\partial}{\partial x_i} \left(C_{\varepsilon} v_i \frac{\partial \varepsilon}{\partial x_i} \right) + C_{1\varepsilon} \frac{\varepsilon}{k} \Pi - C_{2\varepsilon} \frac{\varepsilon^2}{k} \quad (3.14)$$

Substituting the expression for eddy viscosity (Equation 3.7) into Equations 3.12-3.14 we obtained a closed system, meaning that the number of unknowns is equal to the number of equations: six equations for six unknowns- U_i for $i=1,2,3$ mean pressure P , k and ε .

The ε equation is very sensitive to the values chosen for the coefficients $C_{1\varepsilon}$ and $C_{2\varepsilon}$. They depend on each other and they are developed for a special case of free shear flows Rodi (1984). The resulting standard set of constants for engineering flows is $C_o=0.507$, $C_\varepsilon=0.166$, $C_k=1.0$, $C_{o\varepsilon}=0.77$, $C_{1\varepsilon}=1.44$ and $C_{2\varepsilon}=1.92$.

3.2.2 Large eddy simulations approach

Steady simulations cannot predict the semi-instantaneous flow of a 45° PBT observed from digital particle image velocimetry (DPIV) measurements, as discussed by Bakker et al. (1996). The mean flow picture of the average of 1024 DPIV measurements over a period of about 20 minutes matches LDV measurements (Figure 1-2a) and steady state turbulent simulations. It was shown that the real instantaneous flow field is a severely asymmetric with a presence of large-scale instabilities “with a time scale much longer than the impeller rotational frequency”. All of these details (see Figure 1-2b) are smeared out when the averaging is performed.

The basic idea behind LES is to directly solve the governing equations obtained by spatially filtering the Navier-Stokes equations over the small scales of motion that cannot be resolved by the grid. Filtering eliminates the scales which are smaller than the filter width, ξ . The smallest resolved scale is usually chosen to lie in middle of the inertial subrange of the energy spectrum as shown in Figure 3-1. This imposes a limitation on the length of the computational grid cell, which must be somewhere between the length of the large scale and Taylor scale eddies. In FLUENT’s realization of LES, a top-hat filter is used:

$$G_\xi^{hat}(x) = \xi^{-3} \text{ if } |x_k| < \xi/2 \text{ for all } k \text{ and}$$

$$G_{\xi}^{bux}(x) = 0 \text{ if } |x_k| \geq \xi/2 \quad (3.15)$$

where ξ denotes the width of the filter.

Translated into the finite volume discretization formulation, filtering implies averaging over the cell volume and in FLUENT it is performed so that the ratio between the filter width, ξ and grid size Δ is set to be equal to $\frac{\xi}{\Delta} = 2$. The grid size Δ is defined as the distance from the center of the cell to the cell face (Bakker et al., 2000)

The instantaneous velocity u_i , then can be represented as a sum of the resolved scale-filtered velocity component, \tilde{u}_i , due to the large-scale motion and unresolved component, u_i'' which is associated with the small-scale motions and it is given as:

$$u_i = \tilde{u}_i + u_i'' \quad (3.16)$$

Applying the filtering operation to the continuity and momentum equations for incompressible flow of Newtonian fluid, we obtain:

$$\frac{\partial \tilde{u}_i}{\partial x_i} = 0 \quad (3.17)$$

$$\frac{\partial \tilde{u}_i}{\partial t} + \frac{\partial(\tilde{u}_i \tilde{u}_j)}{\partial x_j} = -\frac{1}{\rho} \frac{\partial \tilde{p}}{\partial x_i} - \frac{\partial \tau_{ij}}{\partial x_j} + \nu \frac{\partial^2 \tilde{u}_i}{\partial x_j \partial x_j} \quad (3.18)$$

These equations govern the evolution of the large, energy carrying scales of motion. Equations 3.17 and 3.18 are amenable to numerical discretization at a spatial resolution of order ξ , which is typically much more affordable than DNS, which requires resolutions near the Kolmogorov scale η . The scaling rules show (Tennekes and Lumley, 1989):

$$\frac{\xi}{\Delta} = Re^{-1/2} \text{ and } \frac{\eta}{\Delta} = Re^{-3/4} \quad (3.19)$$

If ξ is at the order of the characteristic inertial length scale (Taylor scale) then, the required number of grid cells will be proportional to the $Re^{3/2}$ which is less severe than in the case of DNS ($Re^{9/4}$). The effect of the small scales appears through a subgrid scale (SGS) stress term,

$$\tau_{ij} = \overline{u_i u_j} - \tilde{u}_i \tilde{u}_j \quad (3.20)$$

that must be modeled. Using the definition of the subgrid scale velocity in Equation 3.16 the SGS stresses can be decomposed in three parts (Leonard, 1974)

$$\tau_{ij} = \overline{u_i u_j} + \tilde{u}_i \tilde{u}_j = L_{ij} + C_{ij} + R_{ij} \quad (3.21)$$

where $L_{ij} = \overline{\tilde{u}_i \tilde{u}_j} - \tilde{u}_i \tilde{u}_j$ are the Leonard stresses, $C_{ij} = \overline{\tilde{u}_i u_j''} + \overline{u_j'' \tilde{u}_i}$ are the cross terms, and $R_{ij} = \overline{u_i'' u_j''}$ are the SGS Reynolds stresses. The Leonard stresses represent interactions between resolved scales that result in a subgrid scale contribution; they can be computed explicitly. The cross term and Reynolds stresses contain unknowns and need to be modeled. The modeling usually relates the unknown subgrid scale stresses τ_{ij} to the large-scale strain tensor \tilde{S}_{ij} as follows

$$\tau_{ij} - \frac{\delta_{ij}}{3} \tau_{kk} = -2\nu_t \tilde{S}_{ij} \quad (3.22)$$

In this case the eddy viscosity (Equation 3.4) is proportional to the filter width, which is the size of the smallest structure resolved in the flow. The velocity scale is usually taken to be proportional to the square-root of the trace of the SGS stress tensor.

Smagorinski (1963) developed the most basic subgrid scale model which is analogous to the Prandtl mixing-length model introduced in Equation 3.4. The model is based on the equilibrium hypothesis relating the eddy turbulent viscosity to the square of the length scale associated with the filter or cell length of the computational grid and the resolved strain-rate tensor:

$$\nu_t = \rho L_o^2 |\tilde{S}| \quad (3.23)$$

where L_o is the mixing length for subgrid scales and $|\tilde{S}|$ is defined as

$$|\tilde{S}| = \sqrt{2\tilde{S}_{ij}\tilde{S}_{ij}} \quad (3.24)$$

and represents the resolved strain-rate tensor defined as

$$\tilde{S}_{ij} = \frac{1}{2}(\partial_j \tilde{u}_i + \partial_i \tilde{u}_j) \quad (3.25)$$

The mixing length, L_o is computed in FLUENT as $L_o = \min(\kappa, d, C_s, V^{1/3})$ where κ and C_s are constant, d is the distance to the closest wall, and V is the volume of the cell (FLUENT v5 manual).

3.3 Simulation conditions

The numerical simulations were conducted using the commercial software package FLUENT v5. The model conditions were chosen to match the experimental conditions described in Chapter 2. The model geometry consists of a cylindrical flat-bottomed tank with diameter $T=0.240\text{m}$ and four full length baffles of width $T/10$. In the experiments a lid was used to prevent air entrainment, so on the top of the tank a no slip boundary condition was set. The 45° PBT impeller had a diameter $D=0.120\text{m}$ and off-bottom clearance ratio C/D equal to 0.50. The impeller shaft diameter was 9mm. The working fluid was water with kinematic viscosity equal to $1 \times 10^{-6} \text{m}^2/\text{s}$. The impeller rotational speed was set equal to 200rpm, which corresponds to a Reynolds number of 48,000.

The geometrical model was built first in MIXSIM on a structured grid with a total of 372,480 cells. Since LES was designed to work only on unstructured grids some additional manipulation was needed prior to the start of simulations. These steps are summarized in Appendix.

3.3.1 Differences between the structured and the unstructured grid

The main advantage of unstructured grid based methods over the traditional structured grid based technique is in the flexibility in discretizing a complex geometry. Unstructured grids can contain either only hexahedral elements or different types of elements such as triangles and quadrilaterals and therefore they are known also as a hybrid meshes. Because the unstructured mesh does not require line structure, it is possible to dynamically adapt it to local features of interest such as sharp gradients of velocity due to changes in geometry. The mixing tank model for example, contains a rotating impeller and stationary baffles and it requires a decomposition of the domain into

two zones which move relative to each other along a boundary also known as sliding mesh boundary (see Figure 3-2a and 3-2b). The sliding mesh boundary typically lies midway between the impeller and the baffles.

Sliding meshes have been used in mixing tank simulations but mostly in conjunction with structured grids (Wechsler et al, 1999). Because of the structured nature of the grids, even though the meshes do not align along the sliding interface the interpolation procedure of fluxes and/or conserved variables is relatively easy to implement.

The interface of the sliding unstructured grid in the new version of FLUENT v5 is made up of faces (which are planar polygons in 3-D case) of grid cells. All faces on the sliding boundary have a unique neighboring cell on one side but multiple neighbors on the other side. These faces also form the boundaries of the control volumes over which the conservation laws have to be satisfied. Since the two grids are moving at any instant, the two sets of boundary faces can be replaced with a new set of faces formed by their intersection. These intersection cells are formed in such a way that each new face has a unique cell neighbor on either side. The shape of the boundary cells in a 2-D case is a polygon see Figure 3-3 (Mathur, 1994). The interface treatment then reduces to the geometrical task of finding the intersection faces and applying the same solution algorithm but with the shape function written for different type elements, for example polygons instead of triangles (3D-case). This process imposes no restrictions on the node placement and connectivity of the individual boundary grid. The algorithm is much simplified and the interpolation procedure is omitted. The procedure is non-directional, in contrast with interpolation where the conserved variables are interpolated from one grid to other and fluxes are interpolated in the reverse direction. The most important benefit is the fact that once the new faces have been formed, they can be treated just like other internal faces by the rest of the solution algorithm.

3.3.2 Numerical procedure

FLUENT v5 uses a finite volume scheme where the physical domain is subdivided into small volumes or cells and the integral equations are applied to each cell. In this

code the domain is discretized into an arbitrary unstructured polyhedral (hexahedral) mesh. The governing equations are evaluated at the center of each cell. The second order upwind scheme is employed for time derivatives, requiring no additional dissipation. This scheme uses information from the two previous time steps to calculate the time derivative. Then the cell-centered solution is expanded to each face of the cell using Taylor series expansion. The impeller motion was modeled using the sliding mesh model for unstructured grids as described by Mathur (1994). Because of the unstructured nature of the grid the number of the neighboring cells may vary around the arbitrary chosen cell. This requires use of a multigrid algebraic solver. The multigrid scheme is coupled with dual-time stepping method (Mathur and Murthy, 1997), which is more efficient for unsteady problems. The time-advancement is made with a second order accurate implicit scheme. This scheme uses information from two previous time steps to calculate the time derivatives. The coupling between the continuity and momentum equations was done using the SIMPLE algorithm (Patankar, 1980).

The computational model contains a full 3-D (O-type) grid with a total of 500,000 unstructured, non- uniformly distributed, hexahedral cells. The default structured grid with total of 372,480 cells was built in MixSim. The distribution of the cells in the (r- θ -z) directions was respectively 194, 32 and 60. The grid was refined in FLUENT 4.5 only in the z-direction and below the impeller. The number of cells in the z-direction was increased to 80. The grid statistics showed that the maximum cell volume was $2.87 \times 10^{-10} \text{ m}^3$ and the minimum cell volume was $1.1814 \times 10^{-7} \text{ m}^3$. If the grid cells were cubes, then the maximum resolved grid length would be 5mm (D/25) and the minimum 0.6mm. Hence the resolved scale is much larger than the Kolmogorov scale, η (approximately $3 \mu\text{m}$) but small enough to resolve the largest scales of interest. For the mixing tanks the characteristic length of the energy containing eddies (trailing vortices) scales with the impeller diameter: $L = D/10 = 12 \text{ mm}$. These eddies are somewhere at the top of the inertial range of the energy spectrum (see Figure 3-1).

The simulation model was started from a zero-velocity field and a period of 23.40 seconds of flow time, or 78 revolutions of the impeller was simulated. Derksen and van den Akker (1999) report that quasy-periodic steady state is reached after 20 revolutions

of the impeller. In this work the rotational speed of the impeller is 200rpm, and the implicit time step is 0.01s so 30 time steps are needed for the impeller to make one full revolution. At every time step 10 iterations were performed to achieve better convergence. The actual wall clock time per one-time step was approximately 8-10 minutes. The simulations were run continuously over a month on a single processor SGI Octane computer with a memory of 640Mb.

3.4 Results

In the first part of this section, the mean flow field obtained from LES is compared with experimental results from previous studies. Velocity profiles at the vicinity of the impeller and at the bulk of the tank are examined. As discussed by Bhattacharya and Kresta (2001), the three-dimensional wall jet theory can be successfully used to completely characterize the vertical flow in the bulk of the tank. LES axial velocity profiles are validated using the wall jet similarity solution. This part confirms that the LES is able to represent the mean circulation pattern extremely well.

The second part of this section considers the transient flow field generated by PBT. The frequency of macroinstability obtained from experiments is identical to that recovered from LES time series. Furthermore, the instantaneous velocity field is recorded and analyzed and two hypotheses for the origin of macroinstabilities are explored.

3.4.1 Mean flow

Verification of the CFD simulations requires comparison of the numerical results with experimental data. In this study, the prediction of the mean axial velocity field is verified first. Because the mean flow field behaves differently in the different tank zones, the mean axial velocities in the vicinity of the impeller are verified first. The radial profile of the LES mean axial velocity (after 21.3 seconds flow time or 71 rotations of the impeller) is compared with the experimental data reported by Kresta and Wood (1993b) in Figure 3-4. The averaging procedure is started after reaching the steady conditions i.e. after 20 rotations of the impeller. The impeller tip velocity is defined as:

$$U_{tip} = \pi ND \quad (3.26)$$

The radial profiles are taken in the mid baffle plane at an axial location 2 mm below the impeller blade. The LES mean velocities agree well with the experimental data, showing the peak of the axial velocity at a dimensionless distance of $2r/D=0.8$. Both the shape of the curve and the magnitude of the U/U_{tip} agree fairly well with the experimental data. The computed profile shows some discrepancies in the region close to the shaft and close to the tank walls. Close to the impeller shaft, the slopes of the velocity profiles differ up to some point where the two profiles start to coincide. This effect is due to the large hub $2r/D=0.22$ used in the simulations while in the experiments the hub size is $2r/D=0.16$. Kresta, (1995) noted the same effect of the hub size on the velocity profiles obtained with the LDV measurements.

The difference between the profiles at radial distance $2r/D=1.3$ can be explained with the position of the sliding mesh boundary. In the simulation this boundary creates a discontinuity, shifting the LES profile. The effect of the sliding mesh boundary can be minimized if a fine grid and adaptation procedure is applied to this interface.

In the bulk of the tank the mean flow forms a vertical wall jet along the intersection of the tank wall and the vertical baffle as shown in Figure 3-5 (Bhattacharya and Kresta, 2001). The half width of the jet, b , is defined as the radial distance where $U=U_m/2$. At any height the velocity increases to its maximum value (U_m) at a dimensionless distance of $0.15b$, as measured from the tank wall. In this part of the wall jet the flow characteristics are similar to those of a simple boundary layer. Further away from the tank wall, the wall jet profile decays and at radial position $y_0=1.7b$ the velocity reverses its direction. It asymptotically approaches the recirculation velocity (U_R). Experimental profiles for several axial impellers at various clearances were all well described by a similarity solution of the following general form:

$$\frac{U}{U_m} = 1 - B \tanh^2 \Phi(\eta - \delta) \quad (3.27)$$

where B is recirculation velocity, $\delta=0.15$ is a standard wall jet boundary layer thickness and Φ forces the solution to go through $(1, 0.50)$ when $b=\eta$. In the Figure 3-6 the experimental data for A310 impeller (Bittorf, 2000) are compared with Equation 3.27.

In Figure 3-7, the LES mean axial velocity profiles in the 3-D wall jet are compared with Equation 3.27. The wall jet profiles were taken at 4 different axial locations: $z/T=0.50, 0.60, 0.70$ and 0.80 . It is evident that for $z/T=0.50, 60$ and 0.70 the simulated wall jet profiles obey the expected similarity scaling. It was assumed that the wall jet is formed along the four baffles, so the simulated jet profiles from two consecutive baffles were compared. The close examination of the simulated mean velocity profiles reveals some differences; the axial mean velocity profiles are not symmetrical along the Plane-1 and Plane-2 (see Figure 3-2). The symmetry of the mean flow is broken due to the fact that the simulations covered 21.3 seconds of impeller revolution, which does not accumulate enough cycles of macroinstabilities in every plane upstream of the baffle. The macroinstability exhibits an intermittent behavior and a long simulation experiments is required. The other problem which was observed is that the axial jet profiles were shifted at the points where the sliding surface is located. To reduce the effect of discontinuity along the sliding surface all profiles are interpolated in the shift points. The interpolation might be avoided if the grid is refined and adapted close to the sliding interface.

At height $z/T=0.70$ the boundary layer starts to grow showing that the parameter δ is $0.20b$. The similarity is no longer maintained for the higher profiles $z/T=0.80$ and 0.90 . In the experiments, the same trend was observed by Bittorf (2000). The height at which the similarity profiles do not obey the similarity solution is used to define the limit of the fully developed turbulence in the bulk of a stirred tank. The same idea can be applied to the simulated profiles. In the Table 3-1 all parameters of the computed LES wall jet profiles are summarized.

3.4.2 Frequency analysis

To probe the macroinstability, 60 probe points are examined at two different planes (Plane-1 and Plane-2) upstream of the baffles (Figure 3-2). At every plane, 5 points at 6 axial locations from $0.40 < z/T < 0.90$ are monitored. The resulting time series are evenly sampled at time steps of 0.01 second. The length of the records is 15 seconds; a time span covering three macroinstability cycles. The sampling was started after reaching the steady state conditions, or after completion of the first initial 20 impeller rotations. In Figure 3-8a a time series taken at Plane-1 at $z/T=0.50$ and $2r/D=1.58$ is shown. The periods of 2.5 impeller revolution are marked with letters from *a* to *g*. LES filters the turbulence and therefore only the low frequency component of the signal is recovered. At every point the highest resolved frequency is 20 Hz, which is high enough to capture the low frequency of interest for this work. The highest frequency is defined by the selected time step, which was 0.01s. It was observed that the periods of regular (coherent) oscillations alternate with periods of chaotic oscillations. In Figure 3-8b a LDV time series is shown. The LDV time series contains more turbulence and again periods of regular oscillations alternate with periods of chaotic oscillations. The LES signal shows the time interval from 14 to 24 seconds, where a period of coherent oscillations roughly follows a sinusoidal signal of frequency 0.63Hz. The same period of regular oscillations was obtained from the LDV signal. It is important to point out that the amplitude of the experimental fluctuations scales with those obtained from the LES calculations. This is very promising if one wants to use CFD methods to quantify the error in the turbulent RMS velocity due to low-frequency oscillations.

The frequencies from the LES time series were extracted with the help of a standard FFT algorithm and the frequency distributions were constructed in a similar fashion to those discussed in Chapter 2. In Figure 3-9 the resulting histogram shows that the frequency of macroinstability, f_{MI}/N is equal to 0.186. The recovered macroinstability frequency from the LES agrees very well with that obtained from both scales of experiment as shown in Figure 3-10. All results confirm that for $Re > 2 \times 10^4$ the f_{MI}/N is constant at 0.186.

3.4.3 Transient flow field of the 45° PBT

The instantaneous flow field (Plane-1) of the 45° PBT is highly 3 dimensional, unsteady and very complicated as shown in Figure 3-11. Seven frames are taken in the r-z plane upstream of the baffle at 18.0, 18.75, 19.50, 20.25, 21.00, 21.75 and 22.50 seconds. The time interval between the frames is 2.5 revolutions of the impeller and the series of images covers at least 15 impeller revolutions, or more than two cycles of the macroinstabilities. The time evolution is examined from the animation (provided as "Movie-Plane1.avi" on the attached CD ROM), which is constructed from a total of 100 frames. The time interval between two consecutive frames is 0.03 seconds, or 10 frames per impeller revolution. The animation starts at 18.00 seconds and ends at 23.4 seconds, a total of 78 revolutions of the impeller. This ensures that the numerical results are not biased by the developing phase of the flow field. The maximum instantaneous velocity magnitude was chosen to be 1.14m/s or $0.9U_{tip}$.

The major event observed at the vertical r-z plane is the presence of high-speed jets below the impeller blades. This agrees with results reported by Tatterson and Brodkey (1980). The jets transport the flow downward impinging either on the bottom or on the wall of the tank. In either case, a wall jet along the wall of the tank forms, driving the flow upwards and entraining the surrounding fluid. To restore the mass balance, the impeller must draw in the same amount of fluid from above, closing the primary circulation loop. A vortex regularly rolls down causing the oscillation of the jet and formation of the secondary circulation loop. The vortex is not always energetic enough to cause deflection of the jet, which is characterized by impingement of the jets on the tank wall instead of the tank bottom. The vortex first appears close to the impeller blade and may be related to the existing trailing vortex system. Then it is rolled down, stretching and engulfing more fluid. The tendency is that at every instant in time the two jets are in phase opposition meaning that when one is impinging on the wall the other is sweeping the bottom of the tank. The time period of the transition of the jet impingement point for the two planes examined is given in Table 3-2. Although the time intervals between these periods are not constant, on average the frequency of jet flapping is the same as the frequency of the macroinstabilities.

The other hypothesis explored, suggests that the macroinstabilities are formed when the two consecutive jets, formed from the blades, hit the corner of the tank. In this situation a strong swirling flow is formed on the bottom of the tank. The two jets converge creating accelerated swirl confined between two opposite baffles. The size of the created vortex is with dimensions of the tank diameter. A schematic picture is given in Figure 3-12. The vortex escapes every time from a different side along the tank wall in a rotating manner and the frequency of this motion may be associated with the macroinstability. A second set of animations was done in order to examine this hypothesis. The velocity field in an $r-\theta$ plane 5 mm above the bottom of the tank is shown in Figures 3-13a-e. Again seven frames are taken at 18.0, 18.75, 19.50, 20.25, 21.00, 21.75 and 22.50 seconds (file "Bottom-plane.avi"). They can give information for the number of converging jets on the bottom of the tank at any instant. The jets interact with each other in a very complicated way, so it is difficult to follow and determine an existing repeatable pattern. The radial velocities with the highest magnitude (see arrows on the Figure 3-13a-e) are always spread out from the impeller region and they trace out the region where the jet sweeps the bottom of the tank. If the jet hits the corner of the tank the radial flow will be driven inward or will result in very low velocities. This situation marks the impingement point of the jet hitting the corner of the tank. At any instant in time no more than two jets are converging on the tank bottom and this can be seen from the region where the flow stagnates. The interaction of the jets creates a swirl, which seems to rotate below the impeller (in the animation this spot can be found where the velocity stagnates).

3.5 Conclusions

For the first time, LES has been successfully applied to study the unsteady macroinstability phenomenon in mixing tanks. Frequency analysis at the resonant geometry for a 45° PBT ($T=0.240\text{m}$, $D=T/2$ and $C/D=0.50$) shows a coherent frequency with dimensionless magnitude of $f_{MI}/N=0.189$ ($f_{MI}=0.63\text{Hz}$.) matching exactly the experimental results from both scales. LES has been used to simulate precisely not only the mean velocity but also the transient macroinstability.

3.6 Nomenclature

$C=$	impeller off bottom clearance (m)
$C_o=$	constant
$D=$	impeller diameter (m)
$f_{MI}=$	frequency of macroinstabilities
$G_{\xi}^{box} =$	spatial top-hat filter
$H=$	liquid height (m)
$k=$	turbulent kinetic energy
$L=$	blade length
$L_o=$	length scale of the most energetic eddies
$N=$	impeller rotational speed (rpm or s^{-1})
$P=$	turbulent production term
$r=$	radial position (m)
$Re=$	impeller Reynolds number $\frac{ND^2}{\nu}$
$S_{ij}=$	resolved strain rate tensor, $\tilde{S}_{ij} = \frac{1}{2}(\partial_j \tilde{u}_i + \partial_i \tilde{u}_j)$
$T=$	tank diameter (m)
$U_{ij}=$	mean velocity component,
$\tilde{u} =$	resolved-scale velocity; $u_i = \tilde{u}_i + u_i''$
$u_i =$	instantaneous velocity
$u_i' =$	turbulent fluctuating component
$u_i'' =$	unresolved-scale velocity
$u_0 =$	reference RMS velocity associated with the large scale eddies
$V=$	cell volume, (m^3)
$W=$	blade width (m)
$x=$	coordinate

Greek

$\Delta=$	size of the computational grid.
$\delta_{ij}=$	Dirak delta function
$\eta=$	Kolmogorov length scale
$\mu=$	absolute viscosity
$\nu=$	kinematic viscosity

ν_t =	eddy turbulent viscosity $\nu_t = \rho L_s^2 \tilde{S} $
ρ =	fluid density
ξ =	filter width, m
τ_{ij} =	SGS stress tensor, $\tau_{ij} = -(\overline{\rho u_i u_j} - \widetilde{\rho u_i u_j})$
ε =	turbulent energy dissipation

Abbreviations

A310=	three bladed aerofoil impeller by Lightnin'
BPF=	blade passage frequency
CFD=	computational fluid dynamics
DPIV=	digital particle image velocimetry
DNS=	direct numerical simulations
FFT=	fast Fourier transform
HE3=	three bladed high efficiency turbine by Chemineer
MI=	macroinstability
LDV=	laser Doppler velocimeter
LES=	large eddy simulation
PBT=	four bladed, 45° pitched blade turbine
POD=	proper orthogonal decomposition
RANS=	Reynolds averaged Navier-Stokes
SGS=	subgrid scale stress
URANS=	unsteady Reynolds averaged Navier-Stokes
VLES=	very large eddy simulation

3.7 References

1. Bakker A., Laroche R.D, Wang M and Calabrese R.V., 1997, *Sliding mesh simulations of laminar flow in stirred tanks*, Transactions of the Institution of Chemical Engineers, **75(A1)** 42-44.
2. Bakker A., Mayers KJ, et al., 1996, *The laminar and turbulent flow pattern of a pitched blade turbaine*, Chemical Engineering Res. and Design, **74 (A4)**, 485-491.
3. Bakker A., L. Ochinowo, E. M. Marshal, 2000, *The use of Large eddy simulations to study stirred vessels hydrodynamics*, Proceedings of 10-th European conference on Mixing, Elsevier Science.
4. Bhattacharya and Kresta, 2001, *CFD simulations of three-dimensional wall jets in a stirred tank*, in press
5. Bittorf K, and S.M. Kresta, 2001, *Three-dimensional wall jets: axial flow in a stirred tank*, AIChE Journal, **47 (6)**, 1277-1284.
6. Bittorf, K, 2000 *The application of wall jets in stirred tanks with solids distribution*, PhD thesis (University of Alberta, Canada).
7. Bruha, O., I. Fort, P. Smolka, and M. Jahoda, 1996, *Experimental study of turbulent macroinstabilities in an agitated system with axial high-speed impeller and with radial baffles*. Collect. Czech. Chem. Commun. **61**, 856-867. Kresta and Wood, 1993
8. Derksen J. and E. A. Van den Akker, 1999 *Large eddy simulations on the flow driven by Rushton turbine*, AIChE, **45 (2)**, 209-221.
9. Fokema M. D., S. M. Kresta and P. Wood, 1994, *Importance of using the correct impeller boundary conditions for CFD simulations of stirred tanks*, Can. J. Chem. Eng., **72** ??-??.
10. FLUENT 5 User's guide. Fluent Incorporated, 1998.
11. Frisch U, 1995, **Turbulence. The legacy of A.N.Kolmogorov**, (Cambridge. University Press)
12. Harvey A D and Rogers S., 1996, *Steady and unsteady computation of impeller-stirred reactors*. AIChE Journal, **42(10)**, 2701-2712.
13. Hinze O.J., 1959, **Turbulence an introduction to its mechanism and theory**, McGraw-Hill Book company.
14. Houcine, I., E. Plasari, R.David and J. Villermaux, 1999, *Feedstream jet intermittency phenomena in continuios stirred tank reactor*, Chem. Eng. J., **72**, 19-30
15. Kresta, S.M., 1998, *Turbulence in stirred tanks: anisotropic ,approximate, and applied*, Can. J. Chem. Eng., **76**, 563-576.

16. Kresta, S.M. and P.E. Wood, 1993a, *The flow field produced by a pitched blade turbine: Characterization of the Turbulence and Estimation of the Dissipation Rate*, Chem. Eng. Sci. **48**, 1761-1774.
17. Leonard, A., 1974 Adv. Geophys. **18A** 237.
18. Marshall E. M., Oshinovo L., and R. Weetman, 1999, *Comparison of turbulence models in CFD prediction of flow number and power draw in stirred tanks*, Presented at Mixing XVII, Banff, Alberta, Canada, August 15-20.
19. Myers, K.J., R.W. Ward, and A. Bakker, 1997, *A digital particle image velocimetry investigation of flow field instabilities of axial flow impellers*, J. Fluids Eng., **119**, 623-632.
20. Mathur, S. R., 1994 *Unsteady flow simulations using unstructured sliding meshes*, AIAA 25-th Fluid Dynamics Conference, June 20-23, Colorado Springs, CO
21. Mathur S and Murthy J. Y., 1997, *A pressure-based method for unstructured meshes*, Numerical heat transfer Part B **31**, 195-215.
22. Patankar S. V., 1980, Numerical heat transfer and fluid flow, Hemisphere Publishing Corporation, Washington, DC.
23. Rande V.V., Joshi J. B. and Marathe A. G., 1989, *Flow generated by pitched baled turbines, II: Simulations using k-ε model*. Chemical Eng. Comm. **81** 225-248.
24. Rodi W., 1984, Turbulence models and their application in hydraulics-a state of art review.
25. Schafer M., Yianneskis M., Wachter P., and F. Durst, 1998, *Trailing vortices around a 45° pitched-blade impeller*, AIChE Journal, **44** (6), 1233-1246.
26. Smagorinski J., 1963 *General circulation experiments with the primitive equations I. The basic experiments*. Monthly Weather Review, **91**, 99-164.
27. Spalart R. P., 2000, *Strategies for turbulence modeling and simulations*, Inter Journal of Heat and fluid flow, **21**, 252-263.
28. Speziale C. 1998, *Turbulence modeling for time-dependent RANS and VLES a review*, AIAA journal, **36** (2), 173-184.
29. Tatterson and Brodkey, 1980, *Stereoscopic visualization of the flows for pitched blade turbines*. Chem. Eng. Sci. **35**, 1369-1375.
30. Tennekes H. and J.L. Lumley, 1989, **A first course in turbulence**, The MIT Press.
31. Wechsler K., Breuer M and F. Durst, 1999, *Steady and unsteady computations of turbulent flows induced by a 4/45° pitched-blade impeller*, Journal of Fluids Eng., Trans. of ASME, **121**, 318-329.

Table 3-1. Parameters of the LES wall jet profiles

Axial position, z/T	Boundary layer thickness, δ	Radial position at $U/U_m=0$	Reverse dimensionless velocity U_R/U_m	$B=1-(U_R/U_m)$
0.50	0.15b	1.70b	-0.40	1.40
0.60	0.15b	1.70b	-0.40	1.40
0.70	0.20b	1.65b	-0.53	1.53
0.80	0.50b	1.50b	-0.72	1.72

Core velocity $U_{core}=-0.46874m/$ at $z/T=0.30$ and dimensionless velocity $U_{core}/U_{tip}=0.37$.

Table 3-2. Time periods showing how long the jets sits either impinging on the bottom or the wall of the tank. The average period of flapping coincides with the f_{MI} obtained from FFT.

PLANE-1				PLANE-2			
Left jet		Right jet		Left jet		Right jet	
Time period, s	Impingement point	Time period, s	Impingement point	Time period, s	Impingement point	Time period, s	Impingement point
0.54	W*	1.05	W	0.63	W	0.60	B
0.96	B**	1.44	B	1.2	B	1.1	W
1.60	W	0.57	W	0.60	W	0.60	B
0.20	B	0.24	B	0.87	B	1.0	W

* **W**-The impingement point of the jet is located on the tank wall.

** **B**-The impingement point of the jet is located on the bottom of the tank.

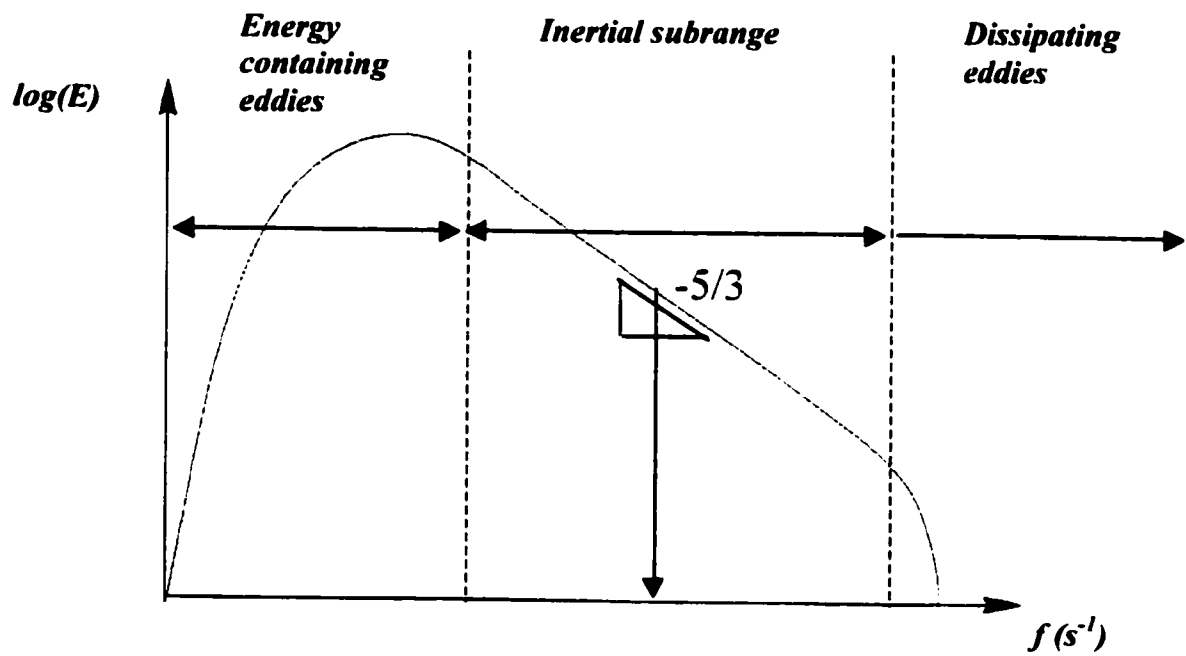


Figure 3-1. Schematic of the idealized turbulent spectrum. The inertial subrange is characterized by a $-5/3$ slope.

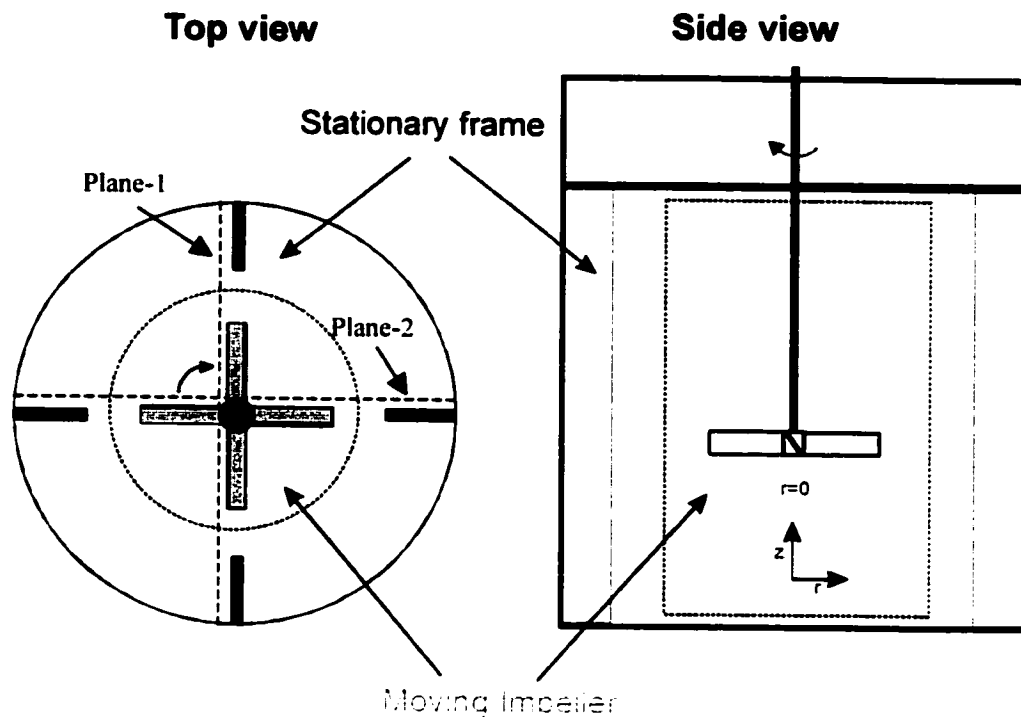


Figure 3-2. Separation of the computational domain with a sliding mesh interface. The sliding surface was chosen to lie midway between the baffles and the tip of the impeller blades: a) top view and b) side view. LES was used to examine both planes 1 and 2.

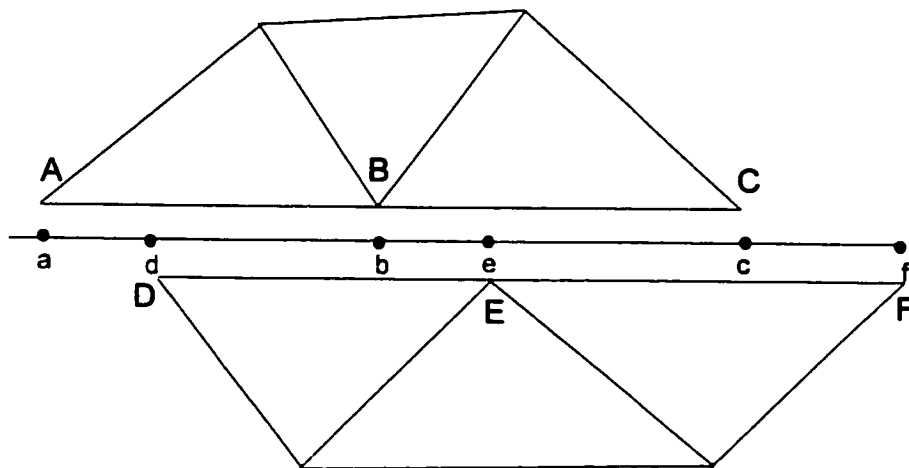


Figure 3-3. Two-dimensional sliding mesh interface (Mathur, 1994)

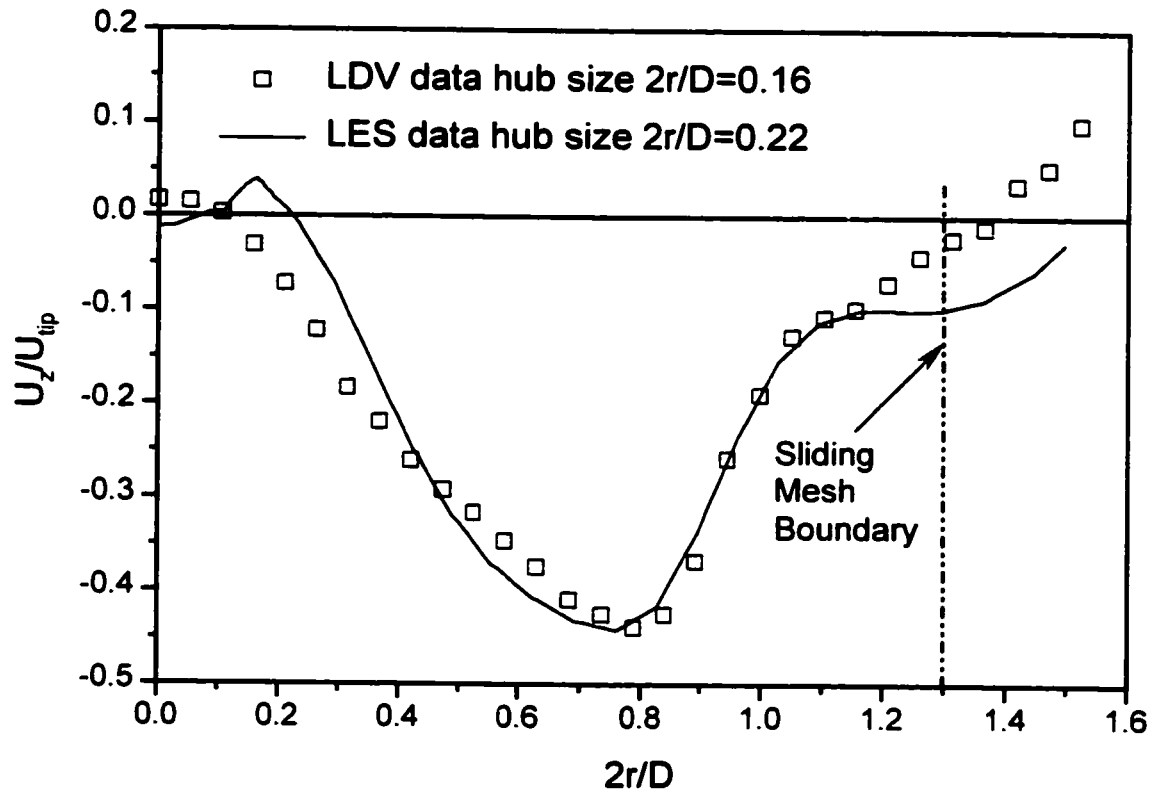


Figure 3-4. Radial profile of the axial velocity in the impeller discharge stream for the resonant geometry (45° PBT, $D=T/2$, $C/D=0.50$). Comparison with the experimental data from Kresta and Wood (1993b) taken 2mm below the impeller blade. Effect of hub size is also shown.

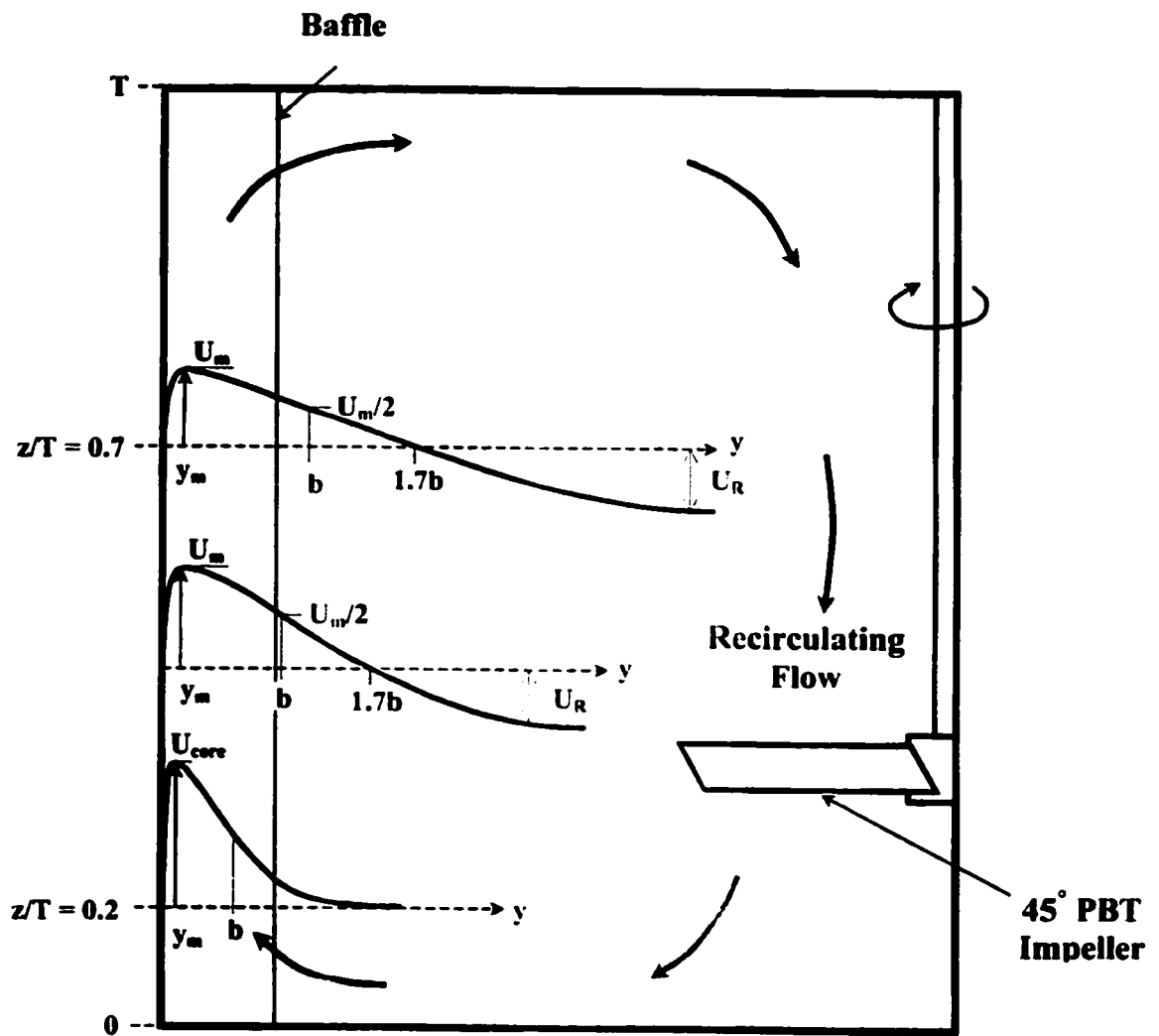


Figure 3-5. Schematic of the 3-D wall jet radial profiles at different axial locations in a stirred tank (Bhattacharya and Kresta, 2001).

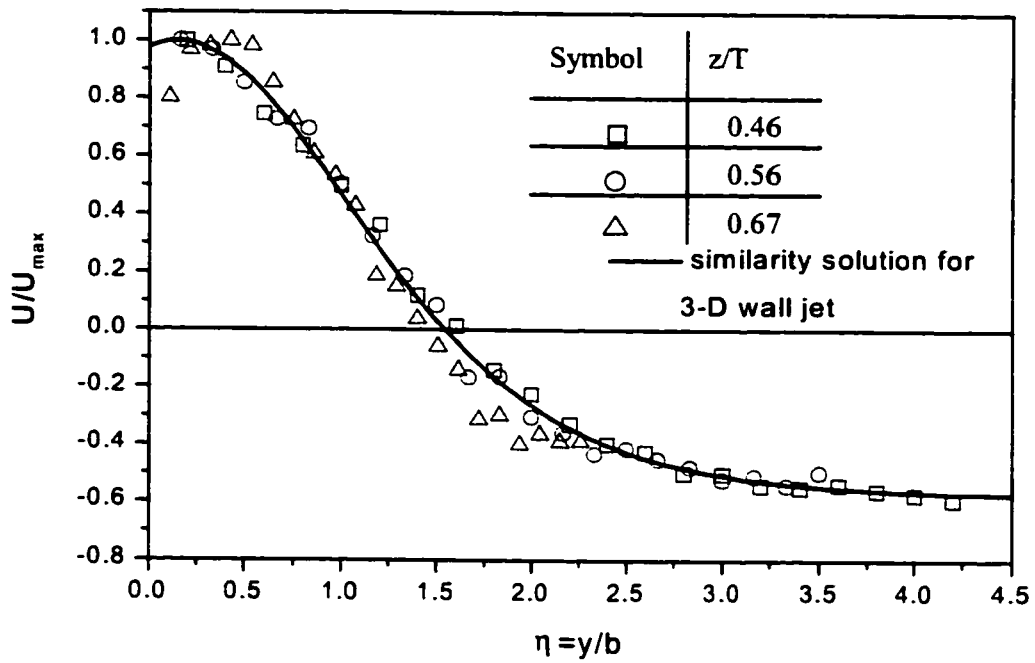


Figure 3-6. Similarity profiles (experimental data by Bittorf, 2000) fit with the similarity solution for the 3-D wall jet (Equation 3.27).

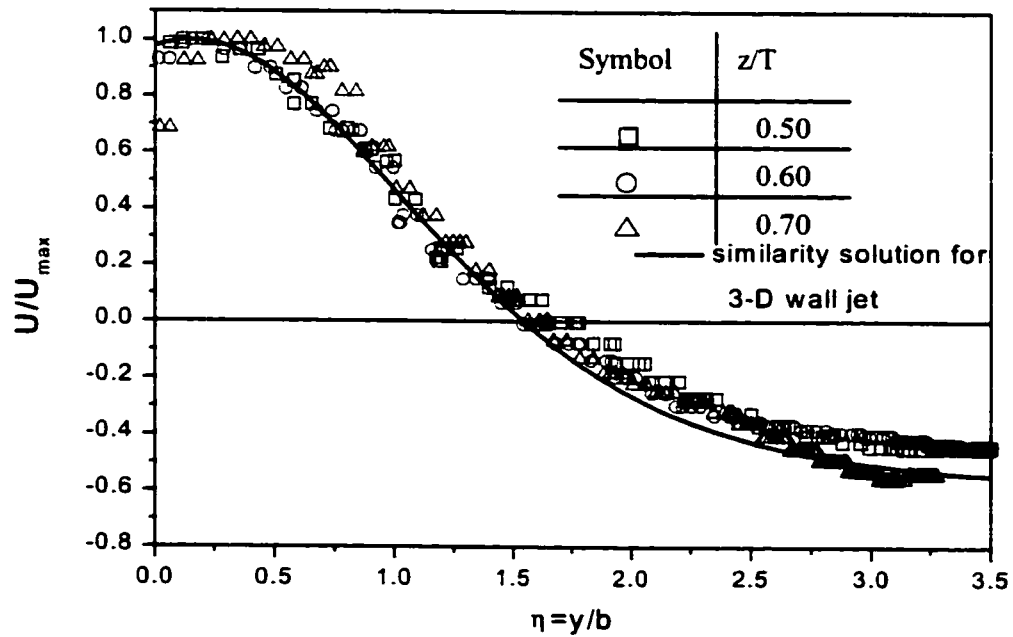


Figure 3-7. Similarity profiles from LES simulation of the resonant geometry (45° PBT, $D=T/2$, $C/D=0.50$).

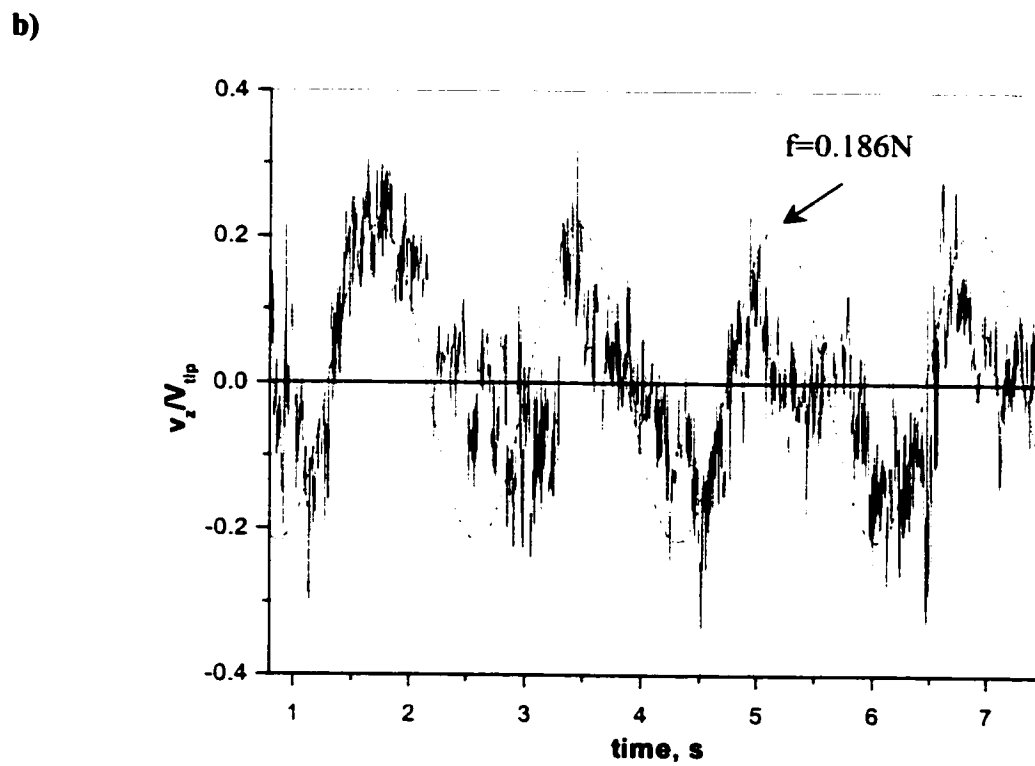
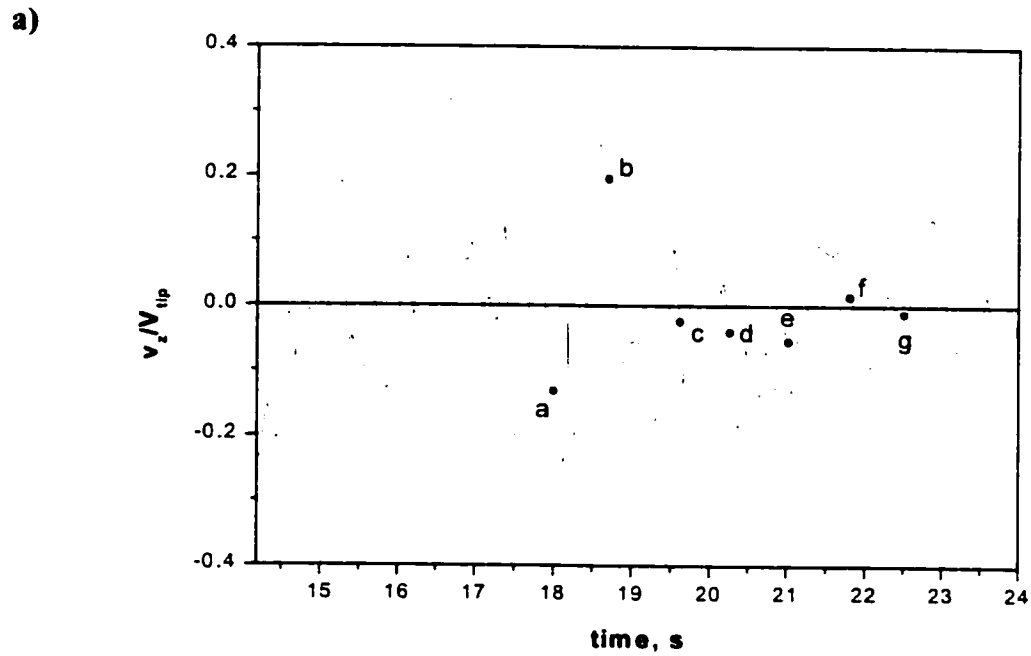


Figure 3-8. Regular oscillations in axial velocity due to macroinstabilities: a) LES time series and b) LDV experimental time series. Note that the turbulence is filtered out of the LES time series. Data are taken at $2r/D=1.58$ and $z/T=0.50$.

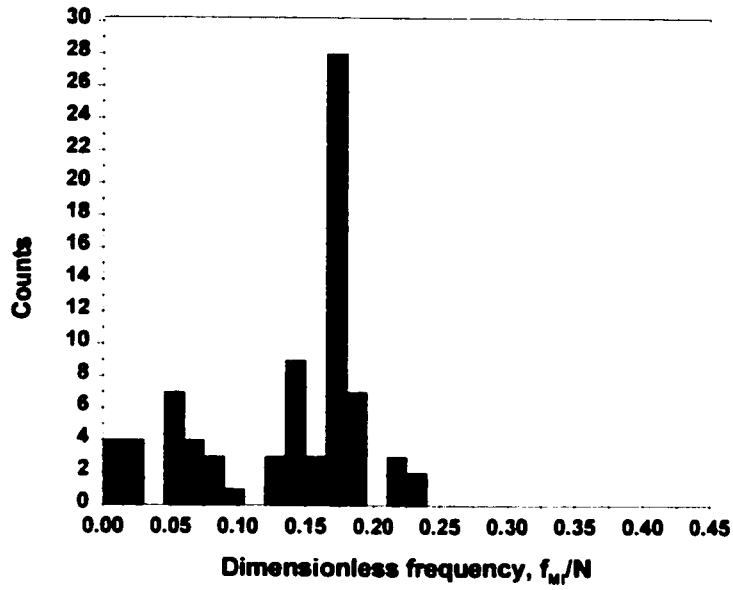


Figure 3-9. LES frequency distribution histogram with maximum at dimensionless frequency $f_{MI}/N=0.186$.

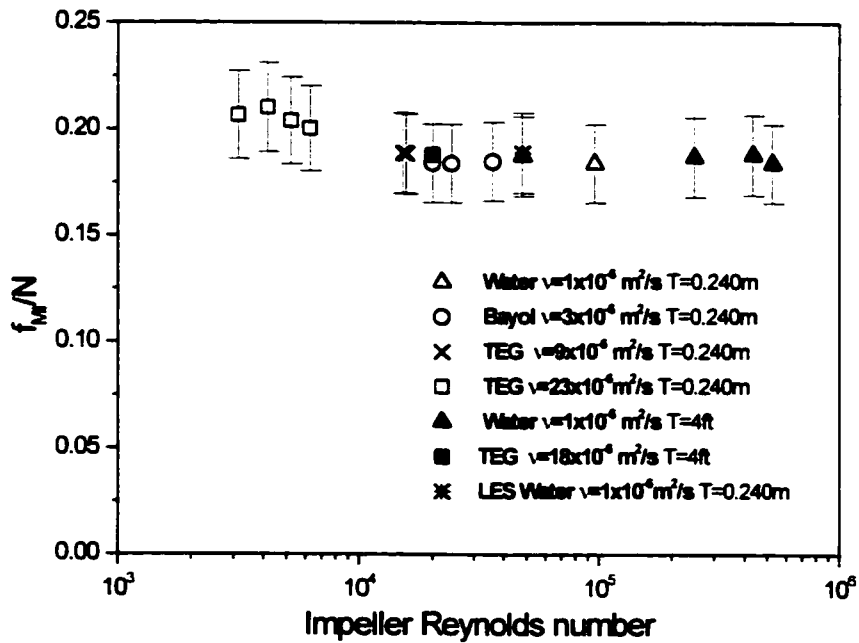


Figure 3-10. Graph showing the scaling of LES f_{MI}/N with impeller Reynolds number.

Figure 3-11a. Instantaneous velocity field (r-z plane) produced by 45° PBT after 18.00s.

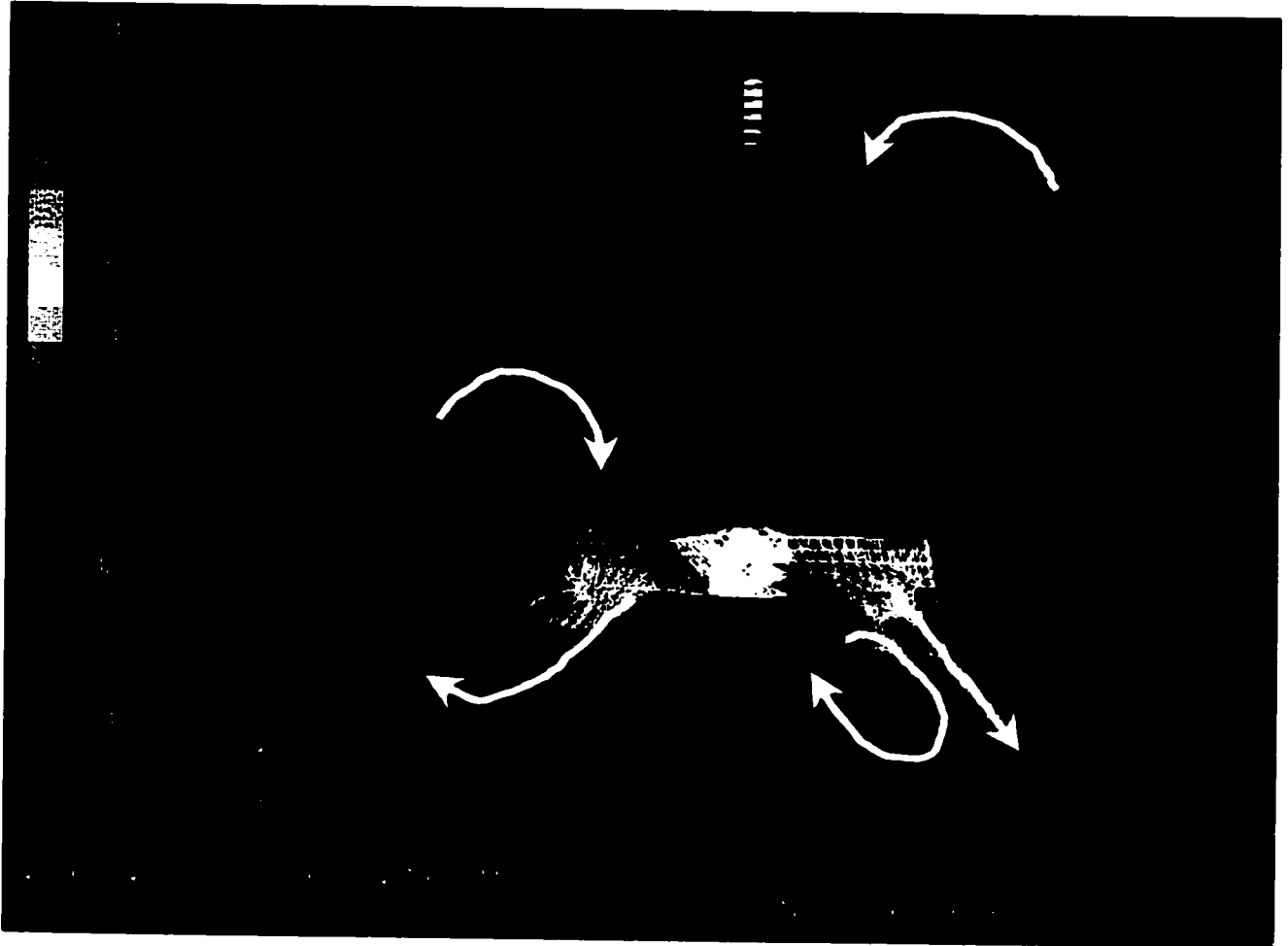


Figure 3-11b. Instantaneous velocity field (r-z plane) produced by 45° PBT 18.75s.

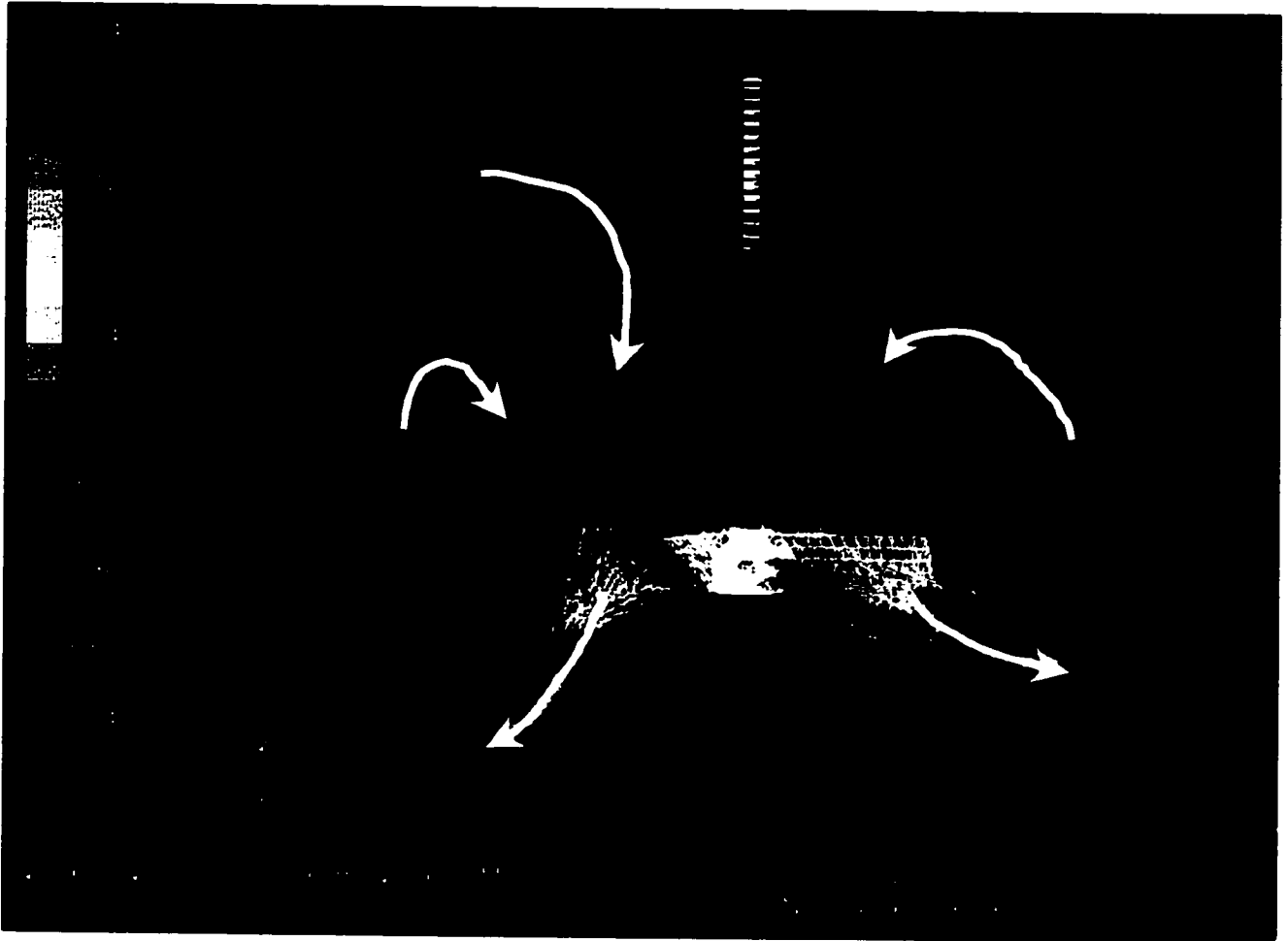


Figure 3-11c. Instantaneous velocity field (r-z plane) produced by 45° PBT after 19.50s.

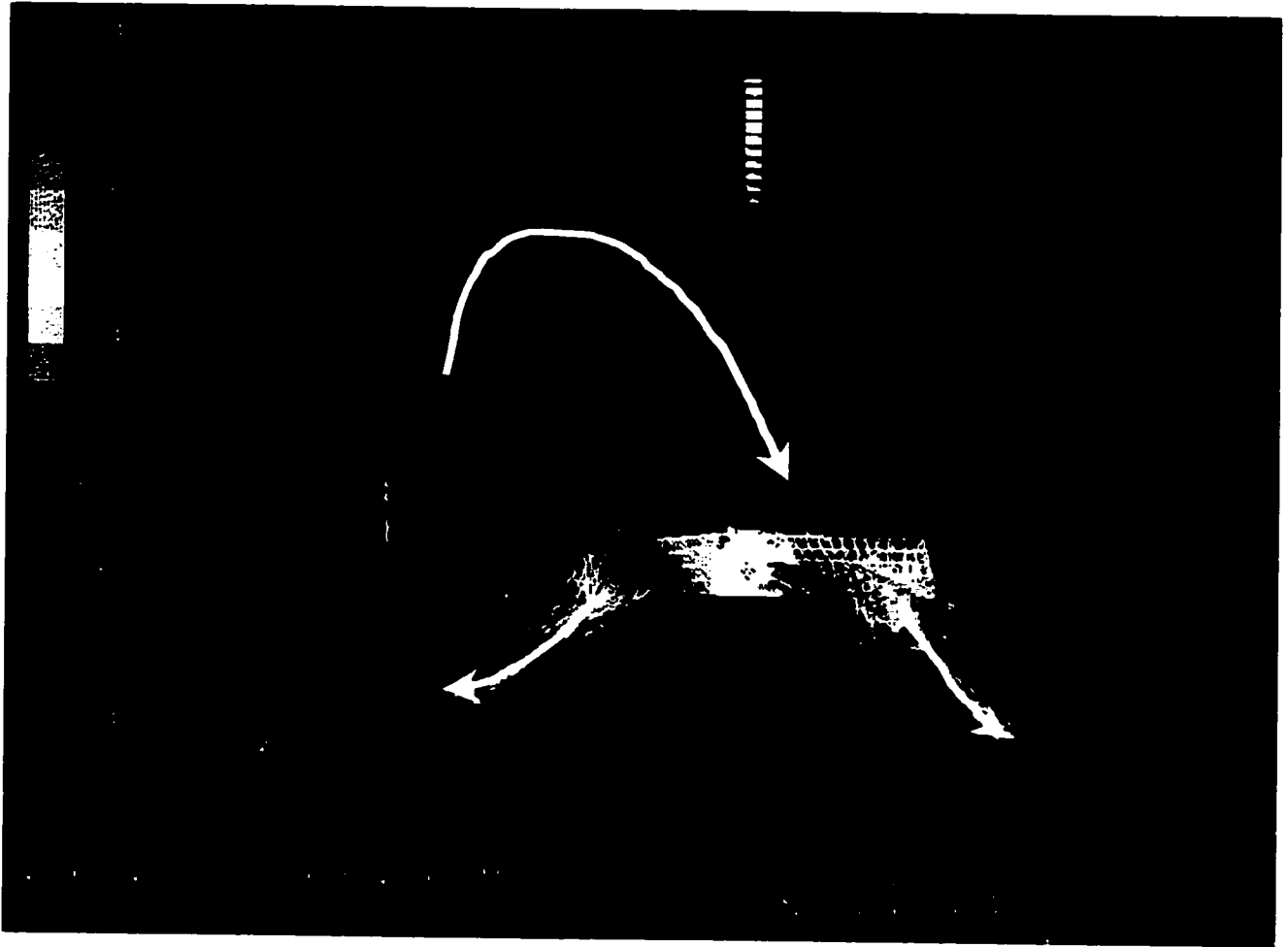


Figure 3-11d. Instantaneous velocity field (r-z plane) produced by 45° PBT after 20.25s.

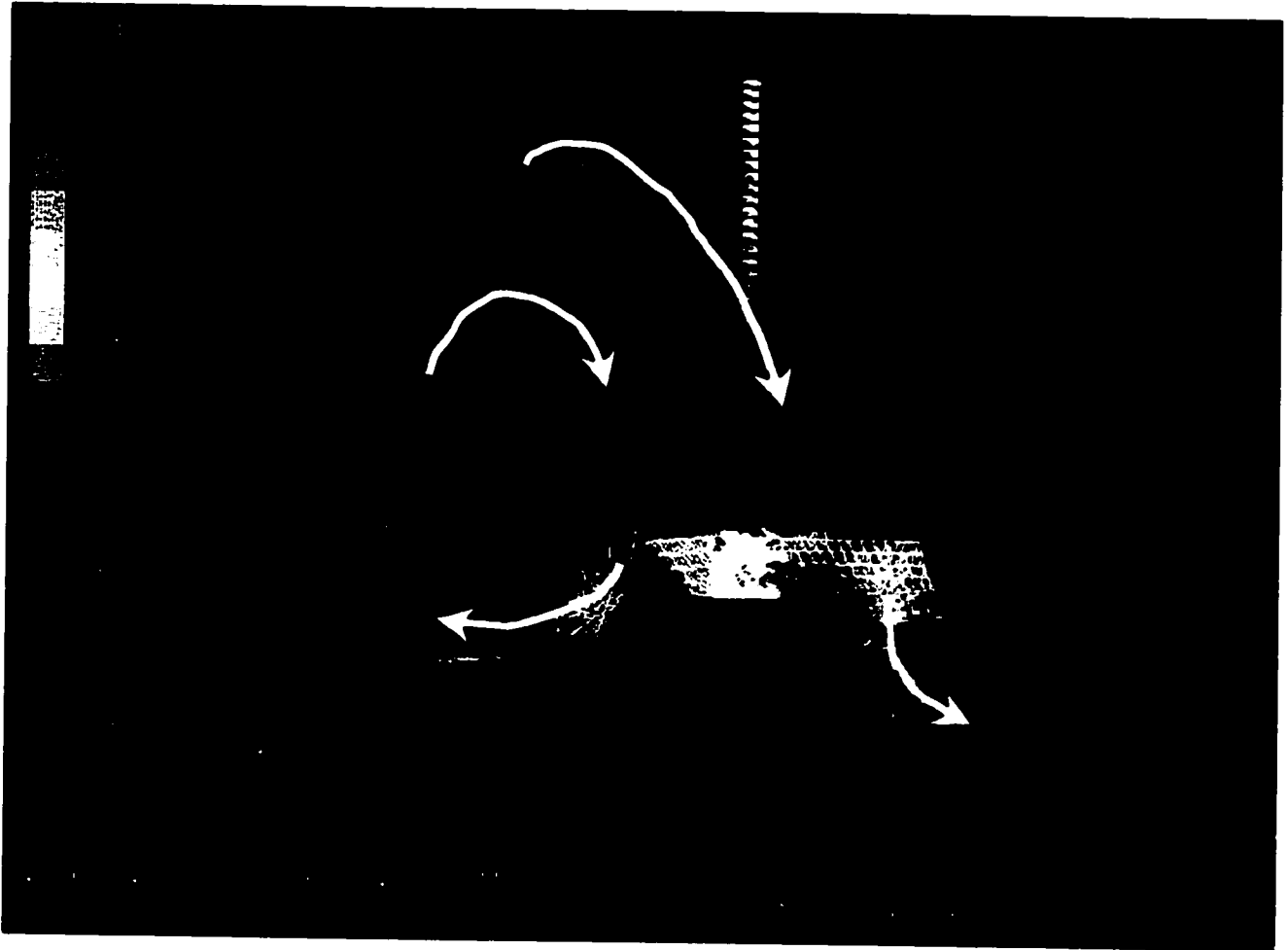


Figure 3-11e. Instantaneous velocity field (r-z plane) produced by 45° PBT after 21.00s.

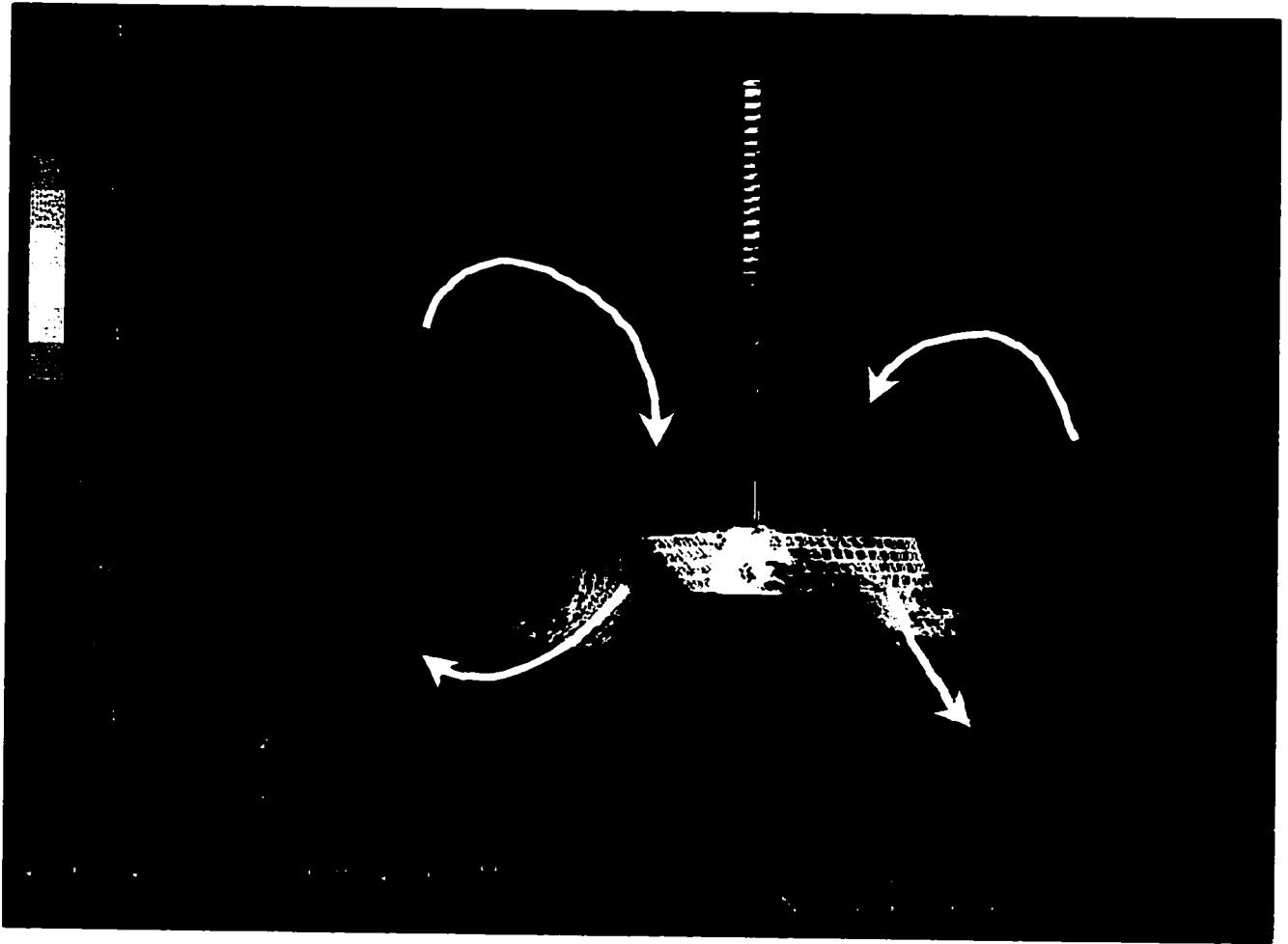


Figure 3-11f. Instantaneous velocity field (r-z plane) produced by 45° PBT after 21.75s.

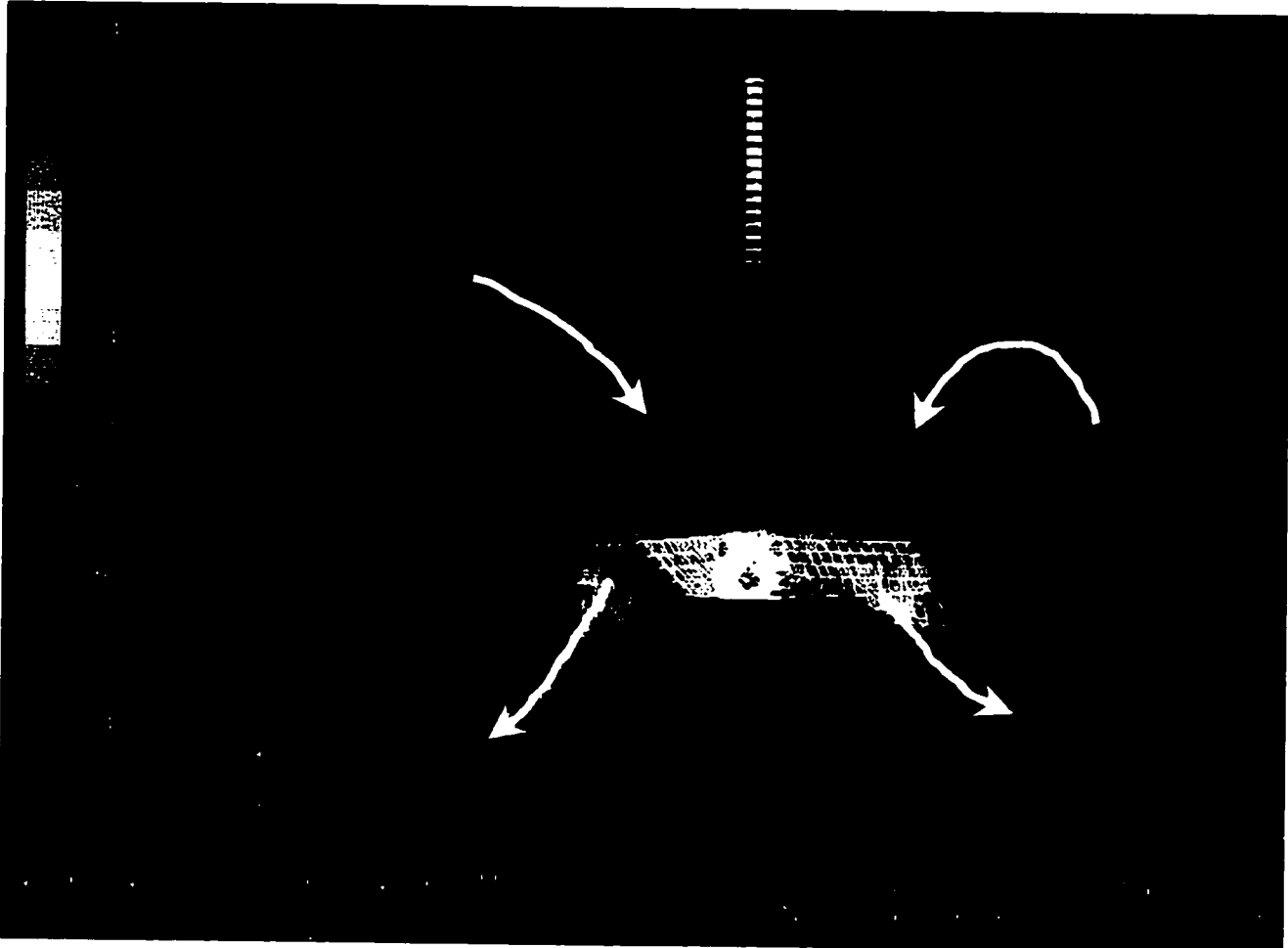
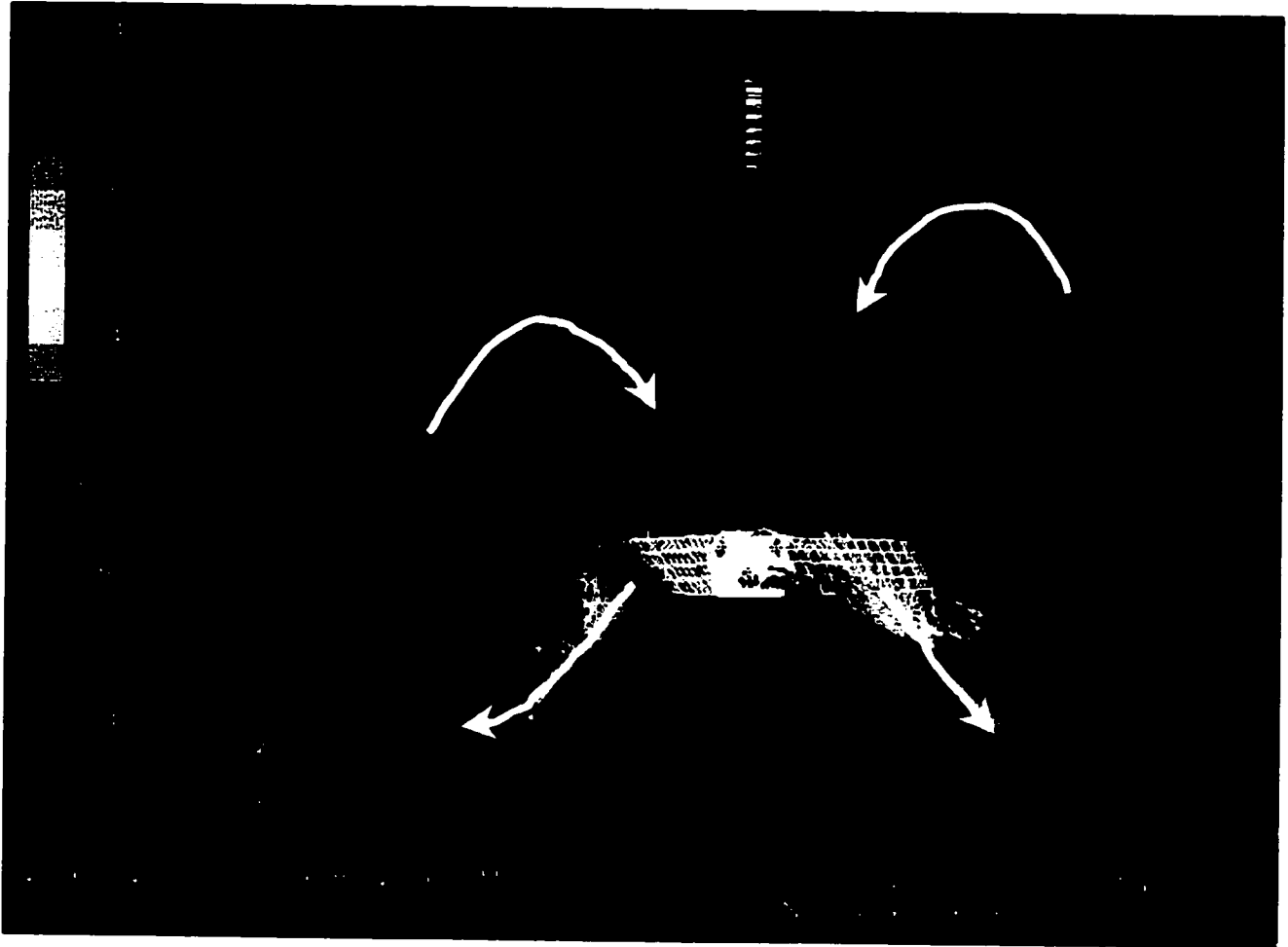
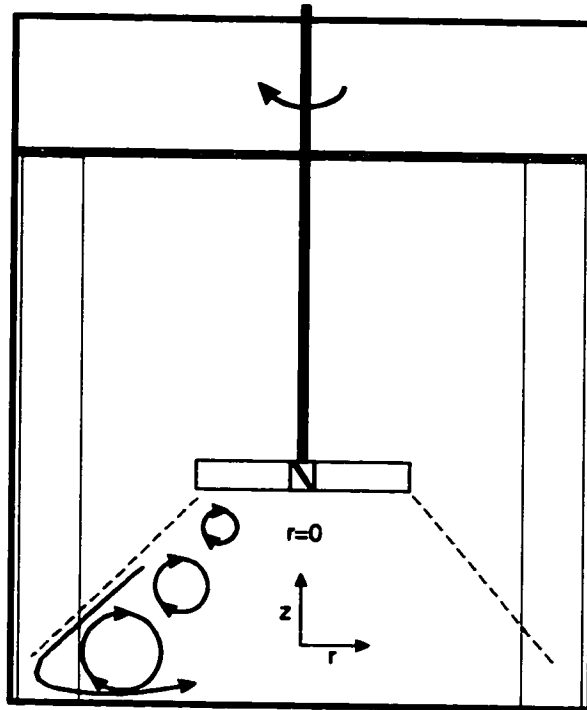


Figure 3-11g. Instantaneous velocity field (r-z plane) produced by 45° PBT after 22.50s.



a) Side view



b) Top view

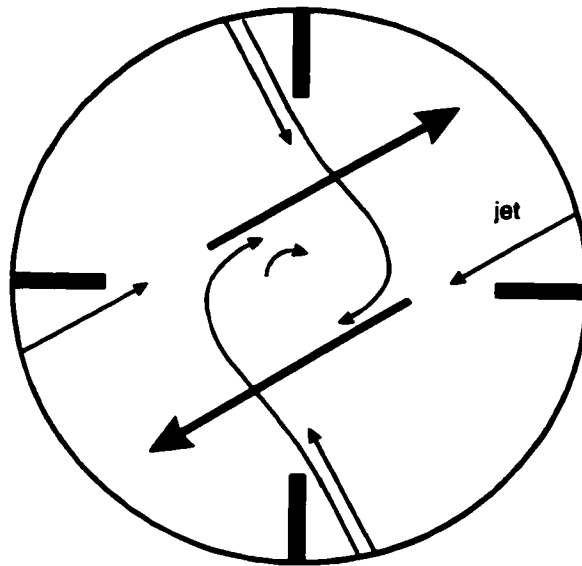


Figure 3-12. Schematic of the four jet interaction below the impeller and close to the tank bottom: a) Side view and b) Top view.

Figure 3-13a. Instantaneous velocity field (r- θ plane) produced by 45° PBT after 18.00s.

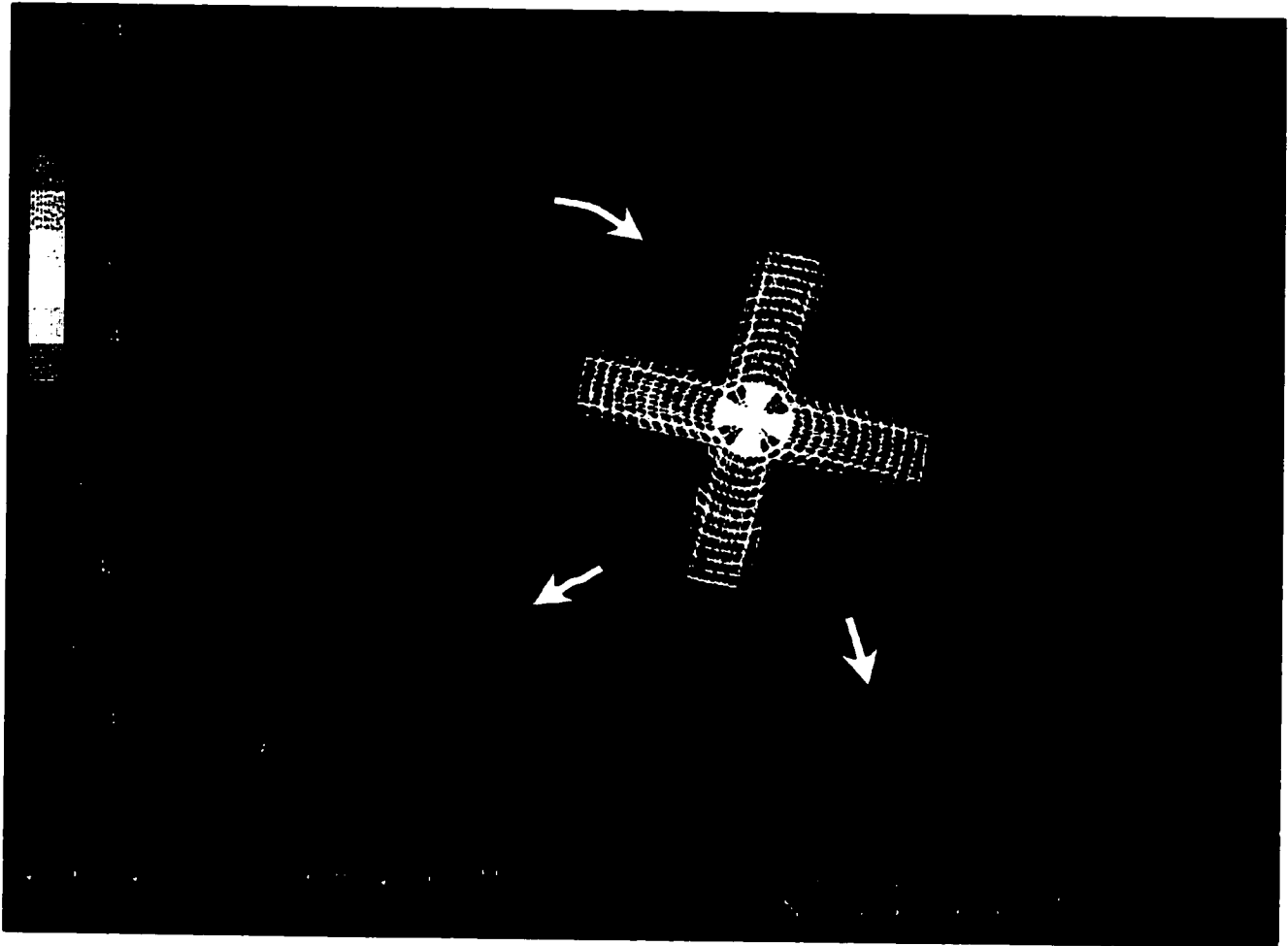


Figure 3-13b. Instantaneous velocity field (r- θ plane) produced by 45° PBT after 18.75s

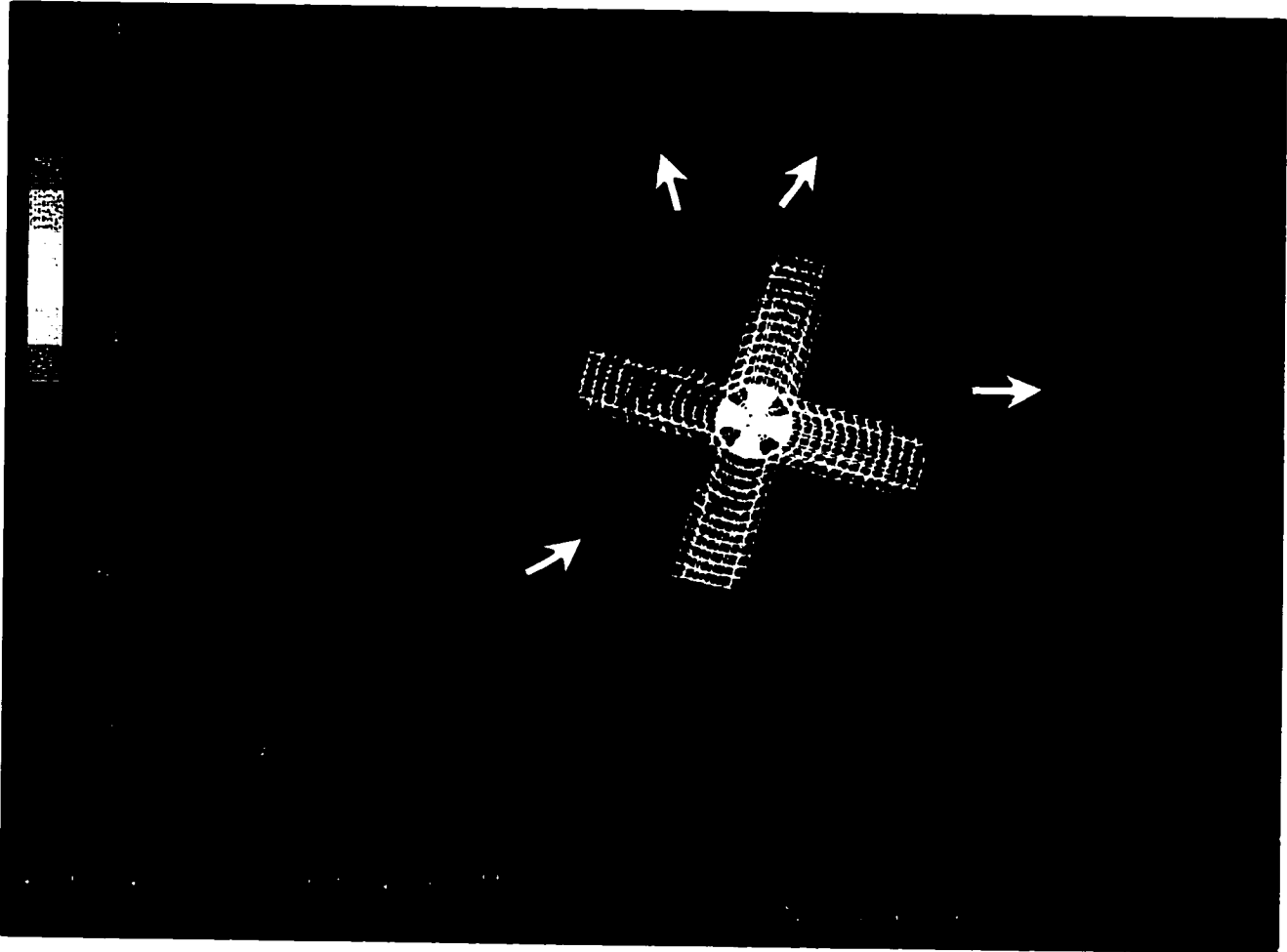


Figure 3-13c. Instantaneous velocity field (r - θ plane) produced by 45° *PBT* after 19.50s

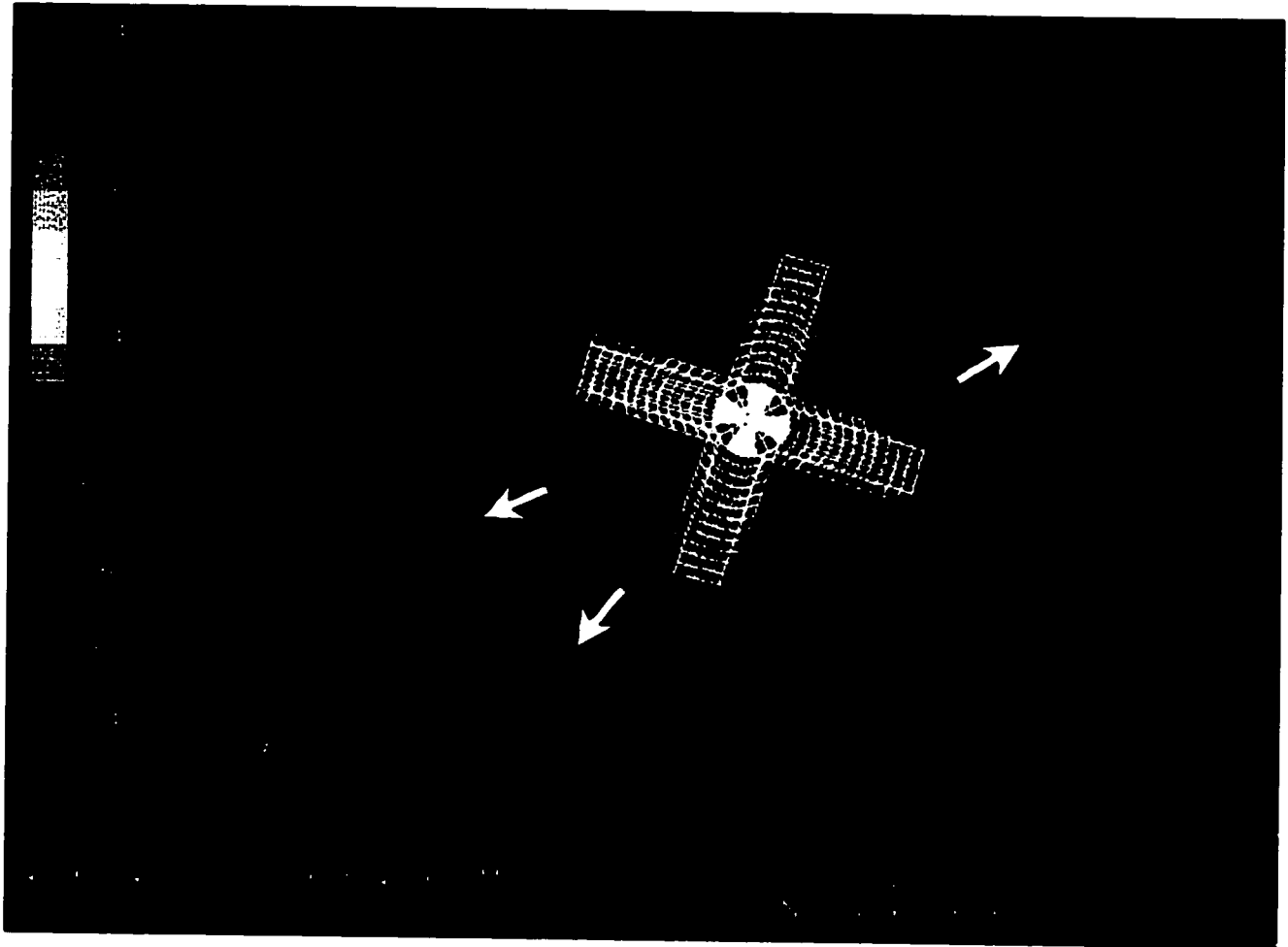


Figure 3-13d. Instantaneous velocity field (r- θ plane) produced by 45° PBT after 20.25s

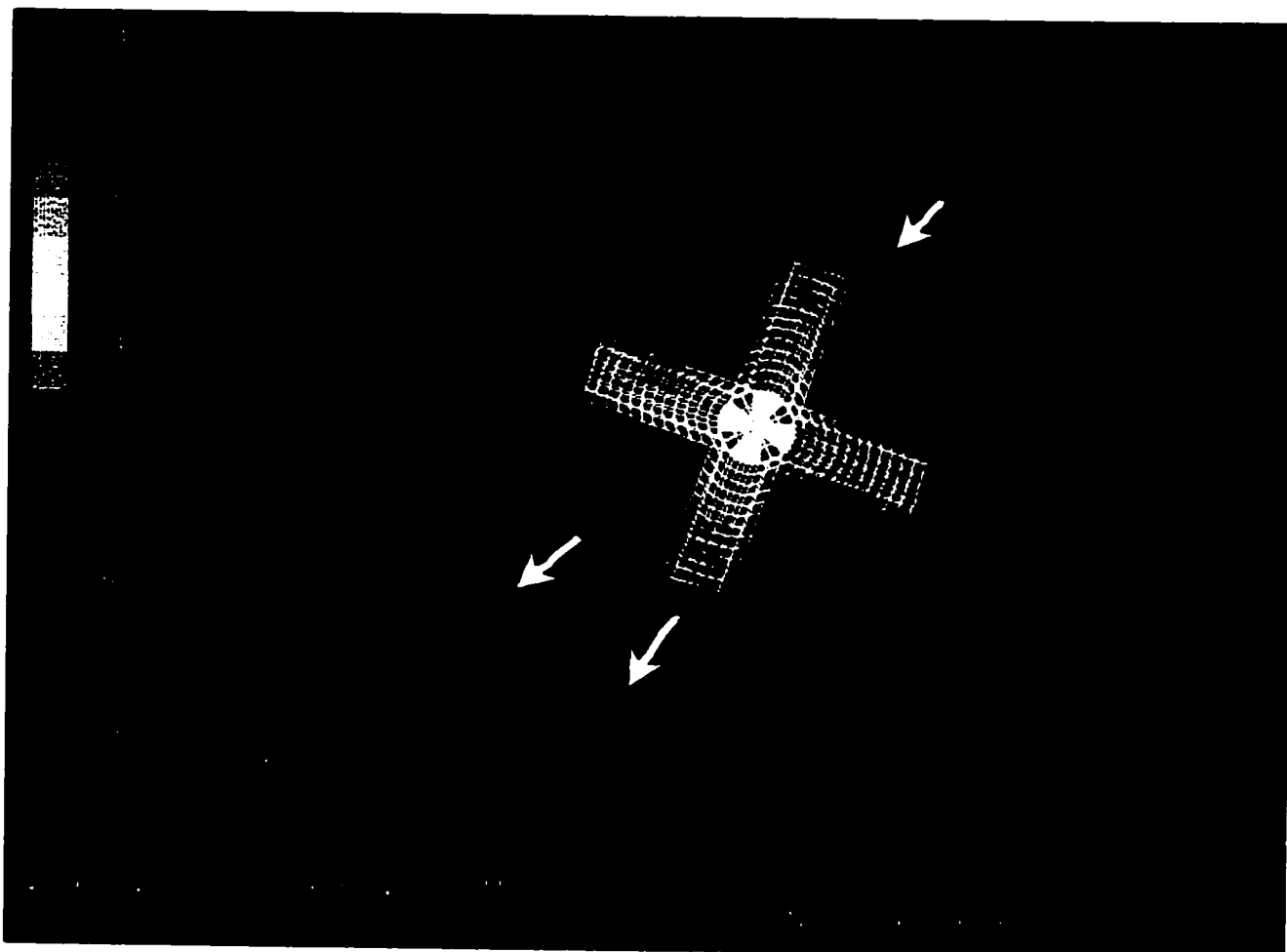


Figure 3-13e. Instantaneous velocity field (r- θ plane) produced by 45° PBT after 21.00s.

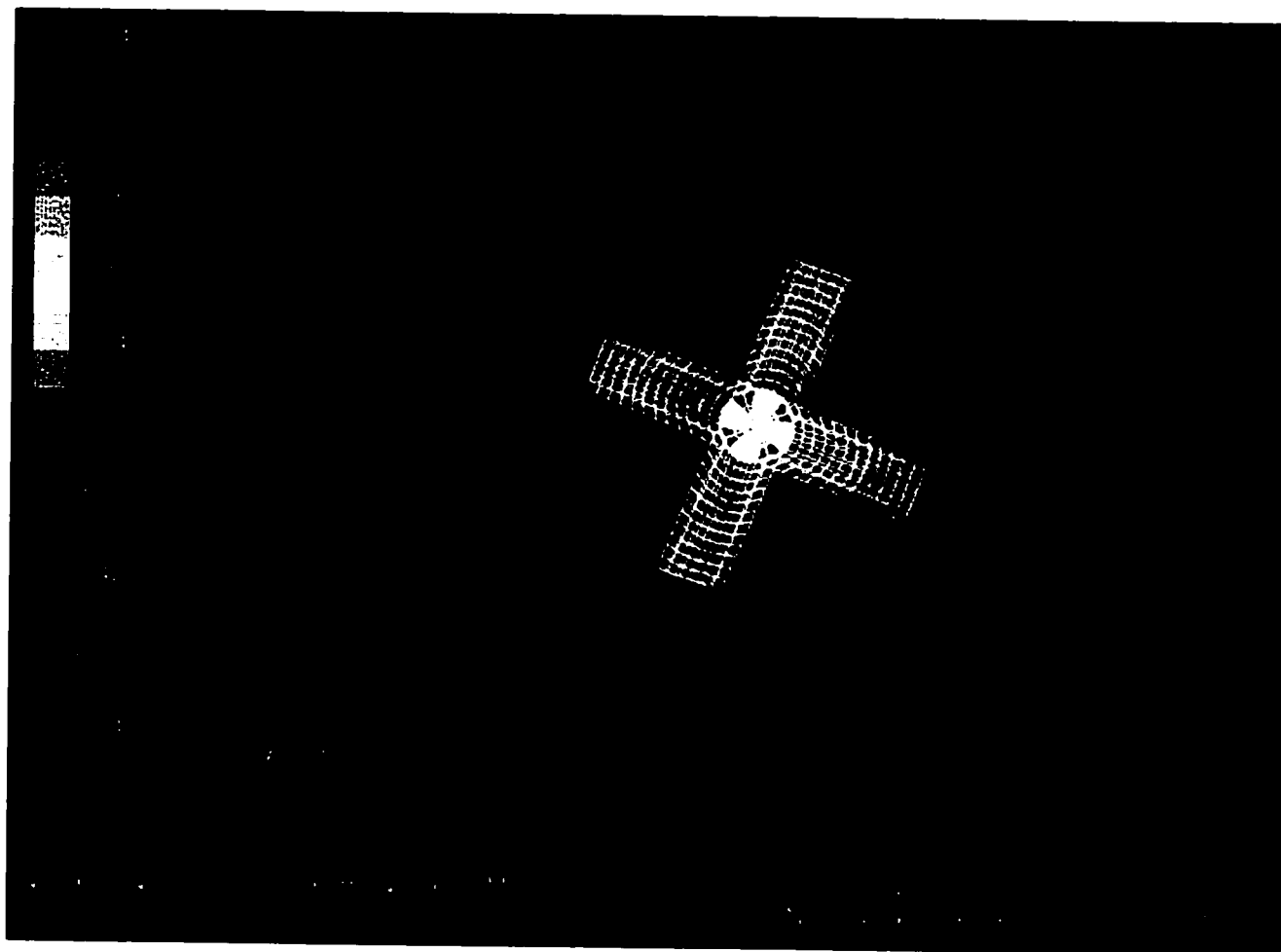


Figure 3-13f. Instantaneous velocity field (r - θ plane) produced by 45° PBT after 21.75s.

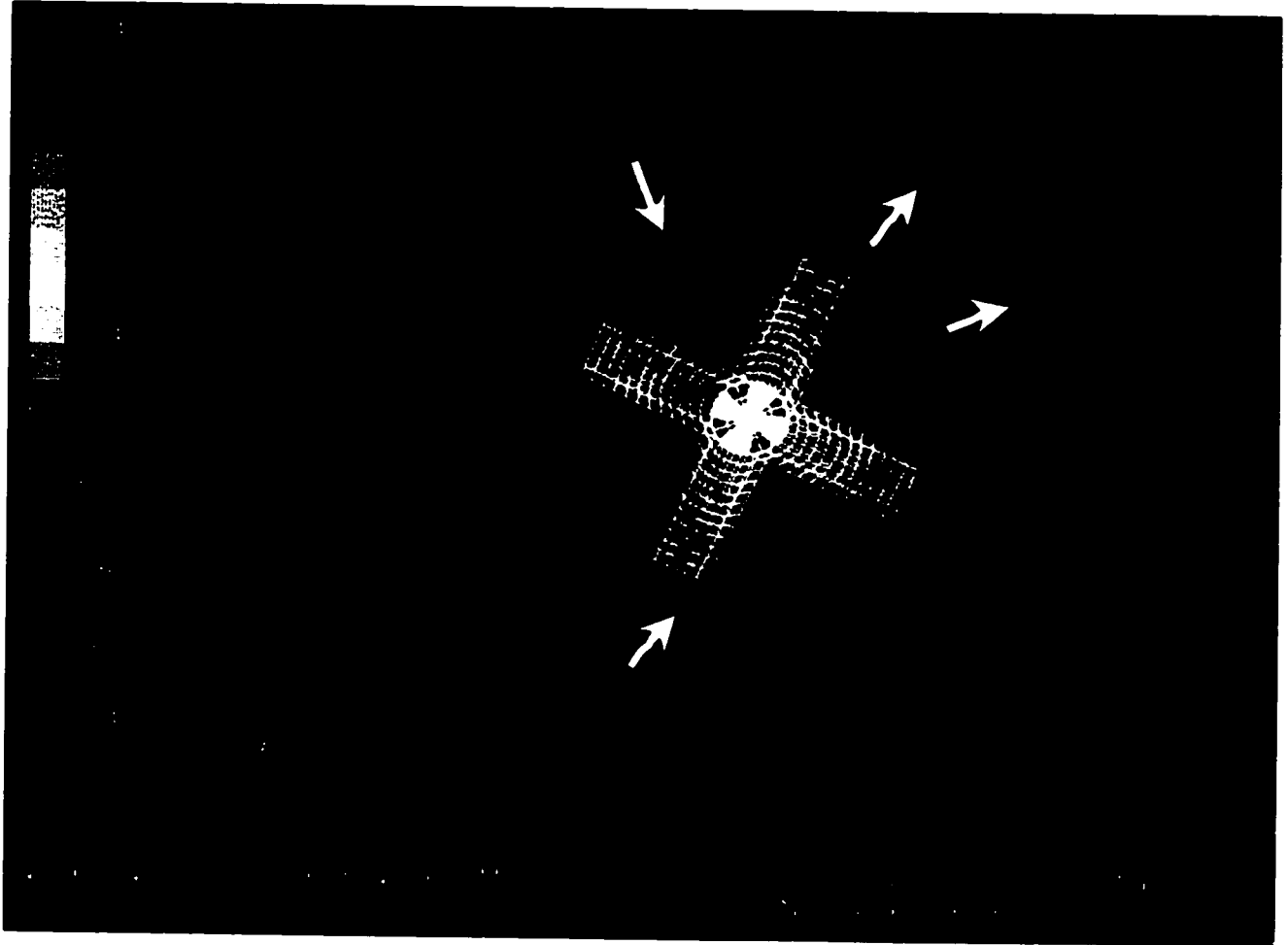
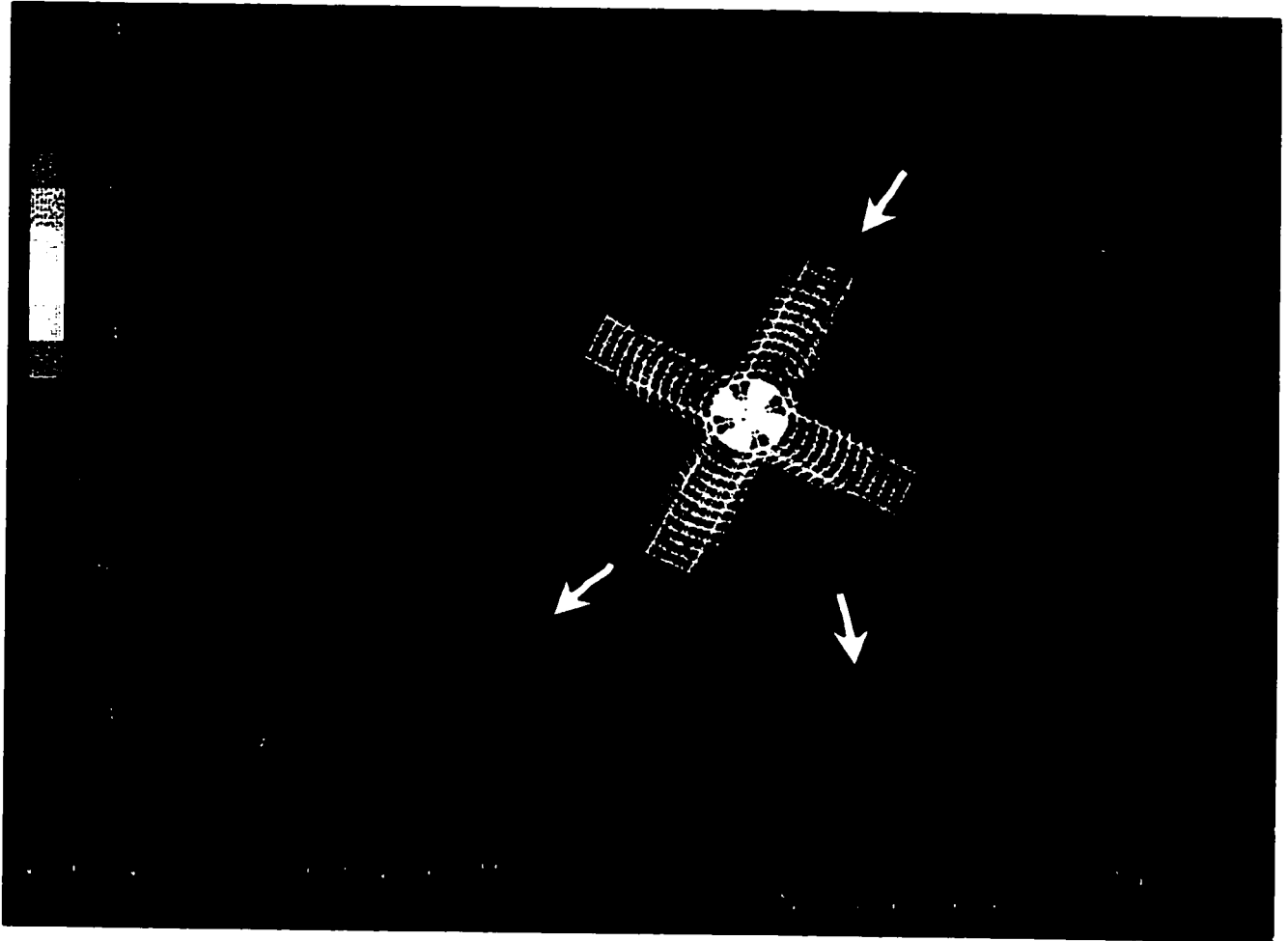


Figure 3-13g. Instantaneous velocity field ($r-\theta$ plane) produced by 45° PBT after 22.50s.



3.8 Appendix

Step 0 In **FLUENT v4.5**, use the Set Cells feature to change the fluid region close to the impeller to WALL type. Write out the case file with a new name. The wall region you just created will be treated as a dead zone when imported to **FLUENT v5** and will not contain any cells. This grid will contain the stationary fluid/grid.

Step 1 Next, read in the original case file back into **FLUENT v4.5** and set the cells OUTSIDE the fluid region around the impeller to WALL (the reverse of **Step 0**). Write out a case file with a new name. Again, the new wall region will be ignored by **FLUENT v5** leaving a fluid region around the impeller and the impeller itself.

Step 2 Exit **FLUENT v4.5** and launch **FLUENT v5**.

Step 3 Next import each of the two **FLUENT v4.5** case files into **FLUENT v5** and write out **FLUENT v5** case files.

Step 4 Exit **FLUENT v5**. The next step is to merge the two **FLUENT v5** case files into a single mesh using the **TGrid 3.x**. Launch **TGrid** and read (File/Read/Mesh...) the two **FLUENT v5** case files. **TGrid** will perform a merge operation. Save the merged mesh.

Step 5 Launch **FLUENT v5** and read in the merged mesh (File/Read/Case...). If the model is a 360° "O"-type grid with cyclic planes, you will need to convert the periodic zone cells to interior type otherwise ignore the following steps. You currently can only do this through the text interface by the following steps:

- 1) Slit the periodic zone command: grid/modify-zones/slit-periodic
 - when prompted for zone id enter the id of the periodic zone which you can determine from the Boundary Conditions Panel.
 - note: this will create two new symmetry zones

- 2) Fuse the resulting interior zones into one interior zone
- GUI command: Grid→Fuse...
 - Text command: grid/modify-zones/fuse-face-zones
 - when prompted for zone id, enter the id of each of the symmetry zones created by the slit-periodic operation.

Step 6 The next step is to set up the grid interface between the two grids. Change the boundary type of the interface walls to Interface type. Next, under the menu Define/Grid Interfaces... panel, create the grid interface from the two interface zones.

- New wall zones are created during the interface creation step. Ignore these zones and do not attempt to delete them.

Step 7 Set-up the models, materials and BCs and **SAVE** the case. Perform a grid check. If you get a warning about multiple shadows existing, exit **FLUENT**, restart **FLUENT**, and read in your case file.

- Setting up the boundary conditions for the two fluid zones requires that one zone be stationary and the other a sliding mesh. To display a fluid zone, use the text interface (display/zone-grid, enter zone id of the fluid zone).

Care has to be taken to ensure the rotational axes of the moving zones are correct (In **MIXSIM/FLUENT v4.5**, the rotational axis is in the x-direction, in **FLUENT v5**, the default direction is the z-direction). The Grid Interface generation can fail if the interface is not uniform, that is if you were to look in the direction of the rotating axis, the path described by the sliding interface should be concentric with that of the stationary interface. It is possible that grid lines of a tank mesh set-up using **MixSim** may not be concentric due to excessive faceting from a coarse grid. If this occurs the grid interface may fail if the deviation (physical separated distance) between the interfaces is large.